HOKKAIDO UNIVERSITY

Title	A mechanism of high-temperature superconductivity from orbital nematic fluctuations and its possibility in iron pnictides and chalcogenides
Author(s)	我妻, 友明
Citation	北海道大学. 博士(理学) 甲第13124号
Issue Date	2018-03-22
DOI	10.14943/doctoral.k13124
Doc URL	http://hdl.handle.net/2115/73115
Type	theses (doctoral)
File Information	Tomoaki_Agatsuma.pdf

Instructions for use

Hokkaido University Collection of Scholarly and Academic Papers : HUSCAP

Doctoral Thesis

A mechanism of high-temperature superconductivity from orbital nematic fluctuations and its possibility in iron pnictides and chalcogenides

（軌道ネマチック揺らぎによる高温超伝導機構と鉄ニクタイド・カルコゲナイドにおけるその可能性）

Tomoaki AGATSUMA

Department of Physics, Graduate School of Science, Hokkaido University

March, 2018

Acknowledgments

I would like to express my special thanks to Prof. Hiroyuki Yamase for his many valuable comments and many scientific discussions during my PhD course. Thanks to them, I learned a way of scientific communications and how to clarify the truth hidden in nature or experimental data. Moreover, he helped me substantially to revise the present thesis. Without his revisions this thesis could not be completed. I would also like to express my special thanks to Prof. Takashi Hotta, who was my supervisor when I was a master student. He gave me many fruitful comments to improve the present thesis, and what I learned during my master course actually provided a strong basis to proceed with the present PhD project. My gratitude also goes to Prof. Migaku Oda and Prof. Takafumi Kita for many valuable comments to make the thesis more complete. During a research life in National Institute for Materials Science (NIMS), I am indebted to many people: Prof. Shinya Uji, Dr. Taichi Terashima, Dr. Naoki Kikugawa, and Dr. Shunsuke Tsuda for insightful comments on my PhD project, and Ms. Yukiko Shibata for a warm support as a secretary in our group. I also thank Mr. Kamo Mosoyan for interesting discussions on various scientific topics in English, which were very useful for brushing up my English. I appreciate Prof. Isao Watanabe for having provided me various opportunities to discuss in Engligh with many professors and many students by using cooperation among RIKEN, Hokkaido University, and NIMS. I also acknowledge Mr. Muhamad Darwis Umar for many general discussions about physics which helped me to improve my scientific communications in English. I thank Mr. Hideo Kawaguchi and Mr. Kensuke Yoshida, who frequently encouraged me to study theoretical condensed matter physics since I was a master student. I am grateful to NIMS graduate research assistantship, which helped me to perform my research during the PhD course. Finally, I would like to thank my family for their support and encouragement.

Contents

Chapter 1

Introduction

In this thesis, we clarify a new superconducting mechanism due to orbital nematic fluctuations and its possible connection to iron-based superconductors (FeSCs). In this introductory chapter, we briefly review the history of superconductivity in Section 1.1, and highlight in Section 1.2 FeSCs, new high-temperature superconductors discovered recently. After reviewing possible superconducting mechanisms of FeSCs, we state our motivation of this thesis in Section 1.3.

1.1 History of superconductivity

In 1911, H. K. Onnes discovered that electric resistivity of mercury suddenly disappears at 4.2K when decreasing temperature. This discovery was the dawn of the history of superconductivity. Since then, superconductivity has been studied vigorously by many researchers, but its origin remained mysterious for a long time. In 1957, J. Bardeen, L. N. Cooper and J. R. Schrieffer[1] proposed the so-called BCS theory, which is now recognized as the standard microscopic theory of superconductivity and successfully explains the superconductivity in various metals. They clarified that the superconductivity is a new thermodynamic state, in which two electrons form a pair, called as the Cooper pair, by an effectively attractive interaction via electron-phonon coupling. This mechanism is schematically explained in Fig.1. When an electron moves through the lattice formed by positive ions, the electron and ions attract each other, which yields a distortion of the lattice. Such a region is then positively charged. Since the ions move much more slowly than the electrons, another electron is attracted to the positively charged area. In this way, the two electrons effectively attract each other via electron-phonon coupling. This is the conventional mechanism of superconductivity.

In 1986 J. G. Bednorz and K. A. Müller[2] discovered cuprate superconductors which exhibit the transition temperature (T_c) as high as 135K at ordinary pressure[3]. Cuprate superconductors are layered systems consisting of CuO_2 layers and block layers[4]. Superconductivity is believed to be driven by electrons in the CuO_2 plane and its minimal model is describied by a two-dimensional model with a single-band by introducing the

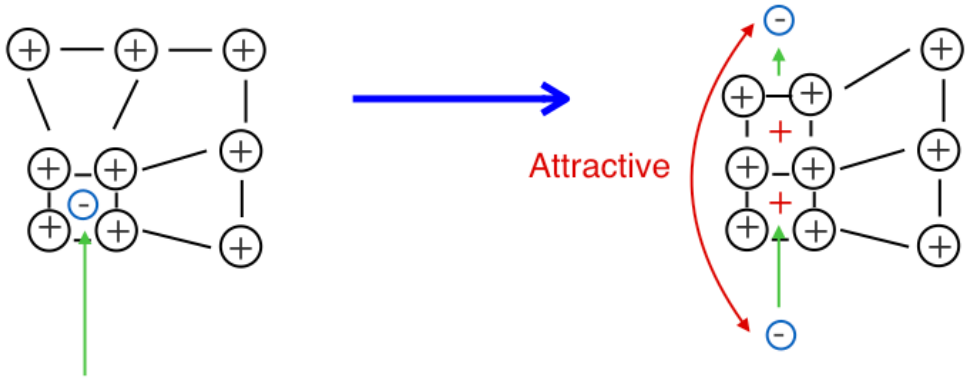

Figure 1: Sketch of the conventional mechanism of superconductivity. When an electron moves through a lattice, which is formed by ions with positive charge, the lattice slightly deforms due to the attractive Coulomb interaction between the electron and the lattice. Such deformation makes a local region positively charged, which then attracts another electron. In this way, two electrons attract each other via electron-phonon coupling and can form a Cooper pair.

concept of the Zhang-Rice singlet[5]. The parent compounds of cuprate superconductors are Mott insulators and superconductivity occurs via carrier doping into the Mott insulator. Therefore the importance of strong electron correlations between electrons is widely recognized. However, in spite of tremendous efforts in the last thirty years, the mechanism of the high-T_c superconductivity in cuprates is still unclear.

In 2006, Y. Kamihara *et al.* discovered other high-T_c superconducting materials, namely FeSCs[6], which turn out to exhibit the T_c as high as 56K[7] and 65K[8]. LaOFeP is a first FeSC and the superconductivity was found by substituting oxygens with fluorines. Its critical temperature T_c was just 5K. In 2008, however, Y. Kamihara *et al.* measured a similar material LaOFeAs, and found the superconducting transition at 26K. After this discovery, the iron pnictides attract tremendous attention as new high-T_c superconductors. Moreover, in 2008 F.-C. Hsu *et al.* found that iron chalcogenides exhibit superconductivity at 8K in FeSe[9]. It was found that T_c of FeSe rises to 65K[8]. Hence the iron chalcogenides are also recognized as new high-T_c superconductors. These two materials, iron pnictides and chalcogenides, are referred frequently to as iron-based high-T_c superconductors. Similar to cuprates, FeSCs have the two-dimensional superconducting layers and the blocking layers. However, in contrast to cuprate superconductors, superconductivity occurs close to the spin-density-wave (SDW) phase, namely a metallic phase. Furthermore, multi-orbital degrees of freedoms are believed to be indispensable to the understanding of superconductivity. Because of these differences, a possible connection to cuprate superconductors is not straightforward. Nevertheless, FeSCs reveal that a high-T_c mechanism is hidden in a multi-orbital system. In fact, the mechanism of the high-T_c superconductivity in FeSCs is one of the hottest topics in condensed matter physics.

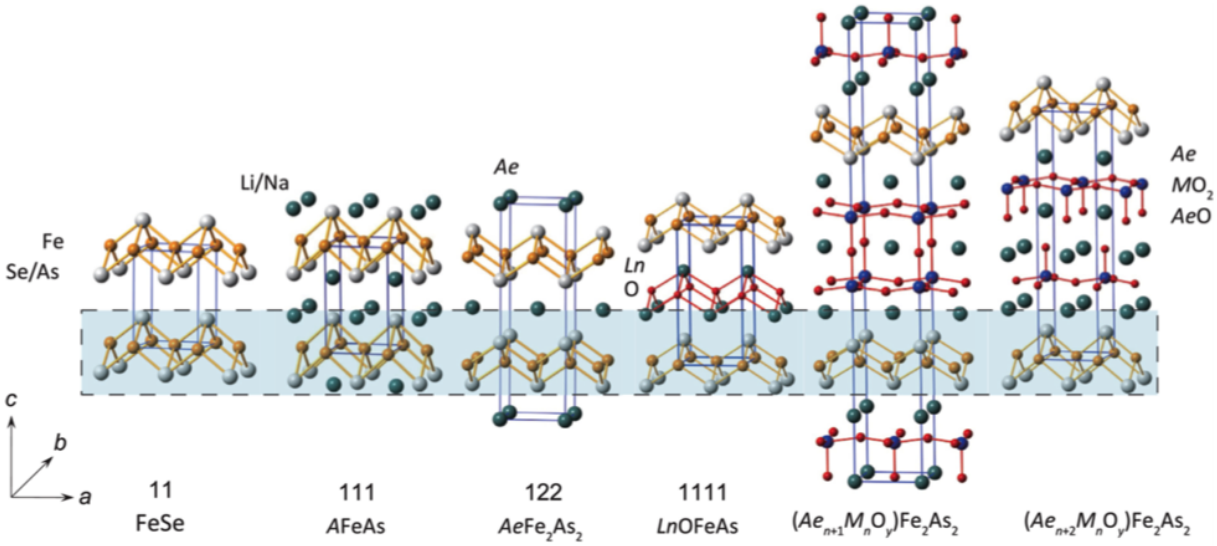

Figure 2: Crystal structures of iron pnictides and chalcogenides[10]. The leftmost is FeSe (iron chalcogenides) and the others are iron pnictides. Blue area is shared by all materials and is believed to be responsible for superconductivity. The yellow balls are the iron sites and the gray balls are the pnictides or chalcogenides sites.

1.2 Iron-based superconductors

Since we are insterested in a possible new mechanism of the superconductivity in FeSCs, we focus on FeSCs. We review their crystal structure in Section 1.2.1, phase diagram in Section 1.2.2, electronic structure in Section 1.2.3, and possible high-T_c mechanisms proposed so far in Section 1.2.4.

1.2.1 Crystal structure

FeSCs commonly have the two-dimensional layer composed of irons (Fe) and pnictogens (Pn) or chalcogens (Ch) as illustrated in Fig.2. The leftmost system is the typical structure of the iron chalcogenides (FeChs). The other five materials are the typical structures of iron pnictides (FePns). Those FePns have many different blocking layers, but they commonly have a two-dimensional layer composed of the Fe and Pn. Therefore superconducting instability is believed to be driven by electrons in the two-dimensional layer of the FePn or FeCh. The two-dimensional layer is illustrated in Fig.3 (a), where Fe sites exist on the same plane and the Pn or Ch sites exist above and below the Fe plane. Since there are two non-equivalent Pn (Ch) sites, a unit cell is given by the blue diamond shown in Fig.3 (a), which contains two Fe and two Pn (Ch) sites. For simplicity, however, a different unit cell, containing one Fe and one Pn (Ch), sites is frequently taken by neglecting non-equivalence of Pn (Ch) sites. This unit cell is shown in the green square in Fig.3 (a). We also take this simpified unit cell in our theoretical study in this thesis.

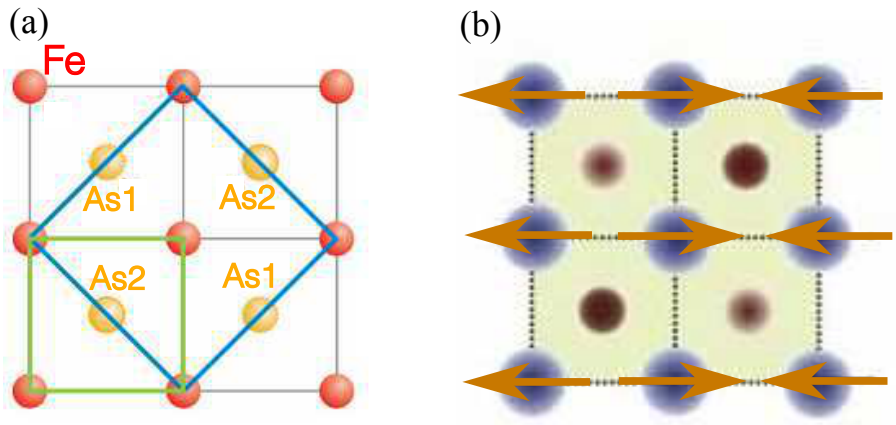

Figure 3: (a) FeAs layer. All Fe (red) sit on the same plane and half of As sites denoted by As1 (As2) is located above (below) the plane of Fe[11]. The blue diamond is the unit cell, containing two iron sites and two arsenic sites. The arsenic sites can be replaced by other pnictides and chalcogenides. The green square would be a unit cell if As1 were equivalent to As2. (b) Typical magnetic structure of iron-based superconductors[12]. The blue circles are the iron sites, and the dark (light) red circles are arsenic sites above (below) the plane of Fe. The arrow represents the direction of the spin of electrons. The spins align antiferromagnetically along the x-direction, and ferromagnetically along the y-direction. This spin structure is often called the stripe-type SDW.

1.2.2 Phase diagram

Figure 4 (a) is a schematic phase diagram of FeSCs, where the horizontal axis is electron (right) or hole (left) doping and the vertical axis is temperature. The red area is a SDW phase, and the spins of itinerant electrons originating from Fe sites align antiferromagnetically one direction, and ferromagnetically along the other direction as shown in Fig.3 (b). This spin structure is often called stripe-type SDW. Close to the SDW phase, an additional phase is realized as shown by the blue area in Fig.4 (a), where the orientational symmetry of the electronic system is broken, otherwise no additional symmetry is broken. This phase has the same symmetry as nematic liquid crystals and is driven by electron correlations. In this sense this phase is called as the electronic nematic phase, or more simply as the nematic phase. In the yellow area a superconducting phase is realized. Because of the proximity of the superconducting phase to the SDW phase, many researchers have considered that spin fluctuations are important to the high-T_c superconductivity in FeSCs.

However a close look at the phase diagram reveals that the nematic phase is also close to the superconducting phase, and is actually closer to the superconducting phase than the SDW phase. The importance of the nematic phase to the superconductivity is, not so highlighted compared with the SDW phase. While the nematic phase is realized in a small region close to the SDW phase in Fig.4 (a), it extends largely in an isovalent doping

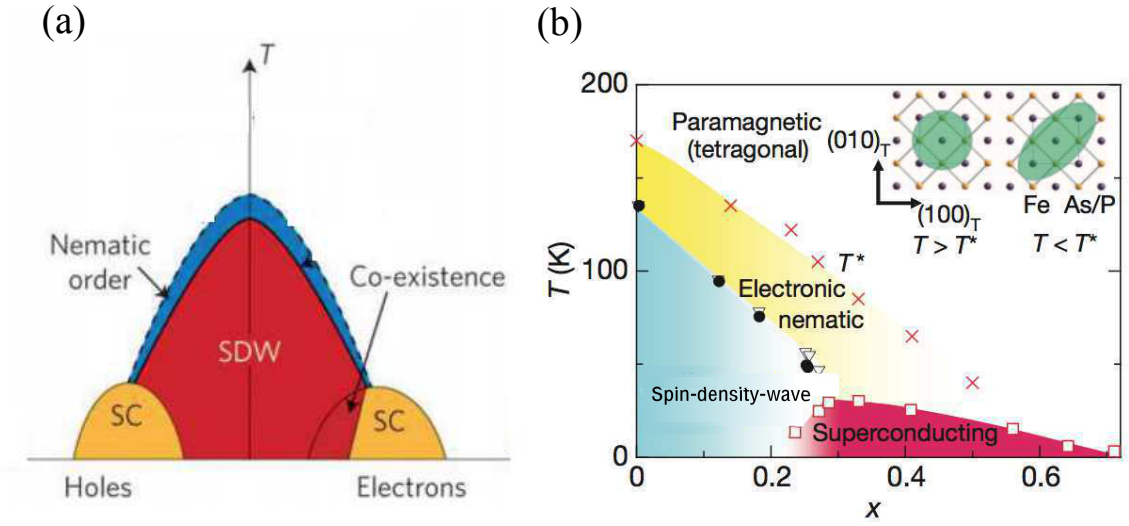

Figure 4: (a) Schematic phase diagram in the plane of carrier doping and temperature T[13]; hole carrier is doped on the left side and electron carrier on the right side. The red area is the SDW phase. In the blue area, the system breaks the orientational symmetry, keeping other symmetries unbroken. This phase is often called as the electonic nematic phase or simply as the nematic phase. The yellow regions are superconducting phases. There can be coexistence of superconductivity and magnetism on the electron-doped state. (b) Phase diagram of $BaFe_2$ $(As_{1-x}P_x)_2$[14]. The superconductivity occurs in the red region, and the SDW phase is realized inside the blue region. The electronic nematic phase is stabilized below T^* in a wider region (yellow) than Fig.4 (a). The inset is a sketch of the nematic instability. C_{4v} symmetry in the normal metallic phase (left) is reduced to C_{2v} symmetry inside the nematic phase (right) as symbolically shown by the green region; The yellow (purple) circles are the Fe (As/P) sites, and the lattice is rotated by 45° compared to Fig.3 (a).

system $BaFe_2$ $(As_{1-x}P_x)$ as shown in Fig.4 (b). The inset is a sketch of the electronic nematic instability, which occurs at T^*. Note that the lattice in the inset is rotated by 45° compared to Fig.3 (a). While the electronic system is isotropic in $T > T^*$, the system breaks the fourfold symmetry spontaneously and exhibits an anisotropy without magnetic order in $T < T^*$. This nematic phase occupies a large part of the phase diagram in some FeSCs. It seems reasonable to assume that in addition to spin fluctuations nematic fluctuations can be equally important for the superconductivity in FeSCs.

1.2.3 Electronic structure

The typical band structure in FeSCs is illustrated in Fig.5 (a). The band indices α, β and γ correspond to hole bands and η and δ electron bands. Those five bands originate mainly from five d orbitals of irons, namely d_{xz}, d_{yz}, d_{xy}, $d_{x^2-y^2}$, and $d_{3z^2-r^2}$ orbitals and all five bands cross the Fermi level (E_F). In this sense, the orbital degrees of freedom are likely

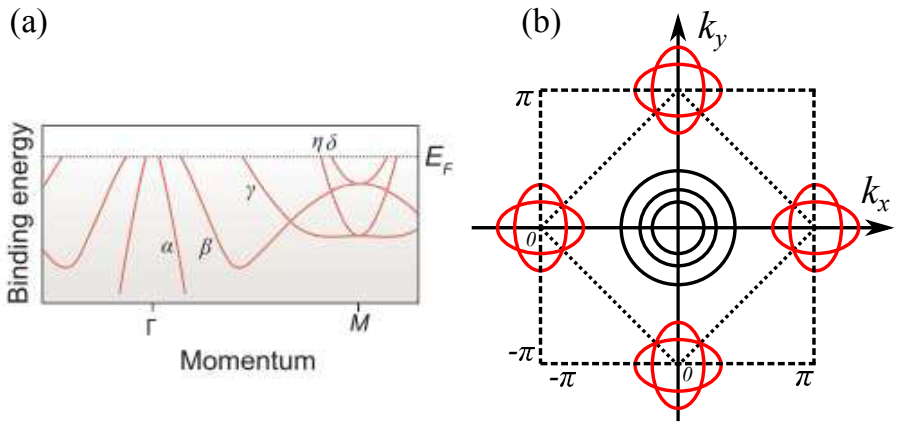

Figure 5: (a) Typical band structure of FeSCs[10]; E_F is the Fermi level. There are three hole-like bands, α, β, and γ, and two electron-like bands, η and δ. (b) Typical Fermi surfaces of FeSCs in the two-dimensional first Brillouin zone. The broken square is the zone boundary for the unit cell containing only one iron site, while the dotted line is that for the unit cell containing two iron sites [see also Fig.3 (a)]. There are three circular hole-pockets around the zone center (black) and two elliptical electron-pockets around $(\pm\pi, 0)$ and $(0, \pm\pi)$ (red).

important to the superconductivity[15]. The two-dimensional Fermi surfaces are shown schematically in Fig.5 (b). The dotted square is the boundary of the first Brillouin zone $(-\pi \leq k_x, k_y \leq \pi)$ for a unit cell with one iron atom [see Fig.3 (a)]. We have hole Fermi-pockets around the zone center and electron Fermi-pockets around momenta $\mathbf{k} = (\pm\pi, 0)$ and $(0, \pm\pi)$.

The presence of the five bands crossing the Fermi energy makes theoretical analysis very complicated. Therefore various efforts have been made to simplify the electronic band structure. One idea is to focus on the d_{xz}, d_{yz} and d_{xy} orbitals because they are the major components of the electronic bands close to the Fermi energy[10]. A more simplified model is proposed in Ref.[16] and [17], where only d_{zx} and d_{yz} orbitals are taken into account. We shall employ such a two-band model as a minimal model of FeSCs in Section 2.

1.2.4 Possible mechanisms of iron-based superconductors

Lattice fluctuations

L. Boeri *et al.*[18] applied the conventional electron-phonon mechanism to understand the superconductivity in FeSCs. They calculated the electron-phonon coupling for LaFeAsO in the density functional theory and found that the obtained maximum T_c reaches 0.8K, which is much smaller than experimental value $T_c \simeq 20-30$K. Hence it is unlikely that the superconductivity in FeSCs is driven by lattice fluctuations, suggesting other mechanisms.

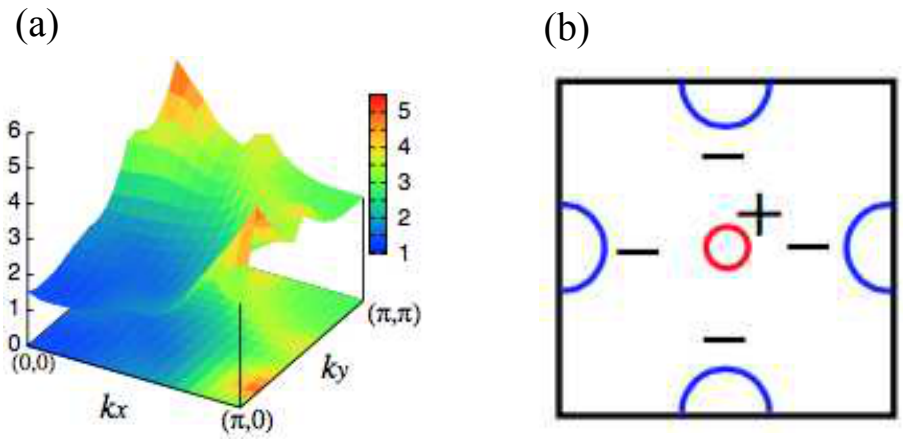

Figure 6: (a) Static spin susceptibility $\chi_s(\mathbf{k})$ in the momentum space $0 \leq k_x, k_y \leq \pi$[15]. There are two peaks around $(\pi, 0)$ and $(0, \pi)$. Spin fluctuations associated with those peaks drive $s_\pm$ superconductivity. (b) Sketch of the $s_\pm$-wave the pairing gap[15]. The red (blue) curve represents a hole (electron) pockets in the first Brillouin zone. The pairing gap have the same sign on each Fermi-pocket, but its sign is different between hole- and electron-pockets. In this sense, this gap is often called as $s_\pm$-wave symmetry.

Spin fluctuations

As many theoretical studies showed[19], antiferromagnetic spin fluctuations can drive superconductivity. Intuitively this may be apparent, because two electrons tend to have the opposite spin direction in the presence of antiferromagnetic fluctuations, which then makes a good chance to form a singlet pair unless magnetic instability occurs. As shown in Fig.4 (a) and (b), the superconducting phase is actually close to the SDW phase. Therefore it is natural to explore the superconductivity mediated by antiferromagnetic spin fluctuations. For the Fermi surfaces shown in Fig.5 (b), spin fluctuations with momentum around $(\pi, 0)$ and $(0, \pi)$ develop due to strong scattering between the hole and electron pockets. This is easily checked by computing the static spin susceptibility as shown in Fig.6 (a), where the susceptibility has two peaks around $(\pi, 0)$ and $(0, \pi)$. While these spin correlations can lead to the stripe-type SDW order with momentum $\mathbf{q} = (\pi, 0)$ observed in FeSCs [see Fig.3 (b)] on one hand, spin fluctuations around $\mathbf{q} = (\pi, 0)$ and $(0, \pi)$ can lead to $s_\pm$-wave superconductivity in FeSCs[20] on the other hand. Here $s_\pm$-wave means that the pairing gap is s-wave on each pocket but has the opposite sign between the hole and electron pockets as schematicaly shown in Fig.6 (b).

Many researchers have explored a possibility that the high-T_c superconductivity in the FeSCs is mediated by spin fluctuation. However, some of the FeSCs do not have the hole pockets, such as LiFeAs and FeSe, which makes it difficult to develop spin fluctuations. In fact, FeSe does not exhibit the SDW phase at ambient pressure. Resulting spin fluctuations may be rather weak in such materials. Nevertheless, all these materials show superconducting instability with $T_c = 8.5 - 19$K[21], suggesting that spin fluctuations

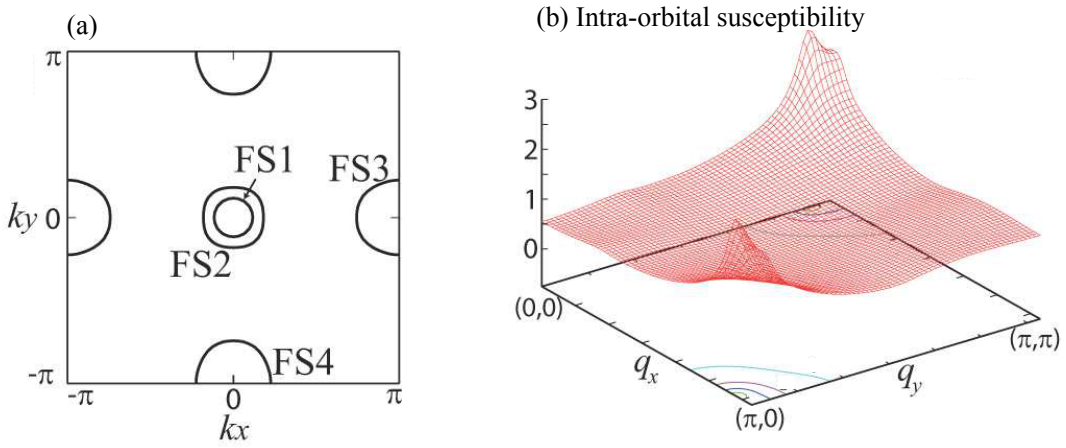

Figure 7: (a) Sketch of Fermi surfaces in the first Brillouin zone of FeSCs[23]. FS1 and FS2 are hole pockets, and FS3 and FS4 are electron pockets. (b) Intra-orbital susceptibility in momentum space $0 \leq q_x, q_y \leq \pi$ by five-orbital Hubbard-Holstein model[23].

alone may not provide a consistent understanding of the superconductivity in FeSCs.

Orbital fluctuations

Since the FeSCs are multiband systems, orbital fluctuations can be important for the superconductivity. T. D. Stanescu, V. Galitski and S. D. Sarma first studied such a possibility and found the superconductivity from orbital fluctuations with momentum around $(\pi, 0)$ and $(0, \pi)$[22]. These fluctuations originate from the nesting between the hole- and electron-pockets [see Fig.7 (a)] and the corresponding intra-orbital susceptibility actually shows a peak at $\mathbf{q} = (\pi, 0)$ as shown in Fig.7 (b). In contrast to the case of spin fluctuations, the intra-orbital fluctuations drive s_{++}-wave superconductivity, that is, the sign of the pairing gap does not change among different pockets.

Orbital nematic fluctuations

As seen in Figs.4 (a) and (b), the electronic nematic phase is present close to the superconducting phase. Hence it is reasonable to consider possible superconductivity from electronic nematic fluctuations. As the origin of nematic order, two scenarios are proposed: spin nematic[24, 25] and orbital nematic order[26, 27, 28]. Since Ref.[29] provides a general argument that the spin nematic order may not easily reproduce the actual phase diagram in FeSCs, we here focus on orbital nematic fluctuations.

Close to the orbital nematic phase, orbital nematic fluctuations develop. Y. Yanagi, Y. Yamakawa and Y. Ōno considered such fluctuations and showed that the orbital nematic fluctuations drive s_{++}-wave superconductivity by employing the two-dimensional 16-band $d-p$ model[30, 31], where not only five d-orbitals (d_{zx}, d_{yz}, d_{xy}, $d_{3z^2-r^2}$, and $d_{x^2-y^2}$) of irons but also three p-orbitals (p_x, p_y and p_z) of arsenics are taken into account. Figure 8

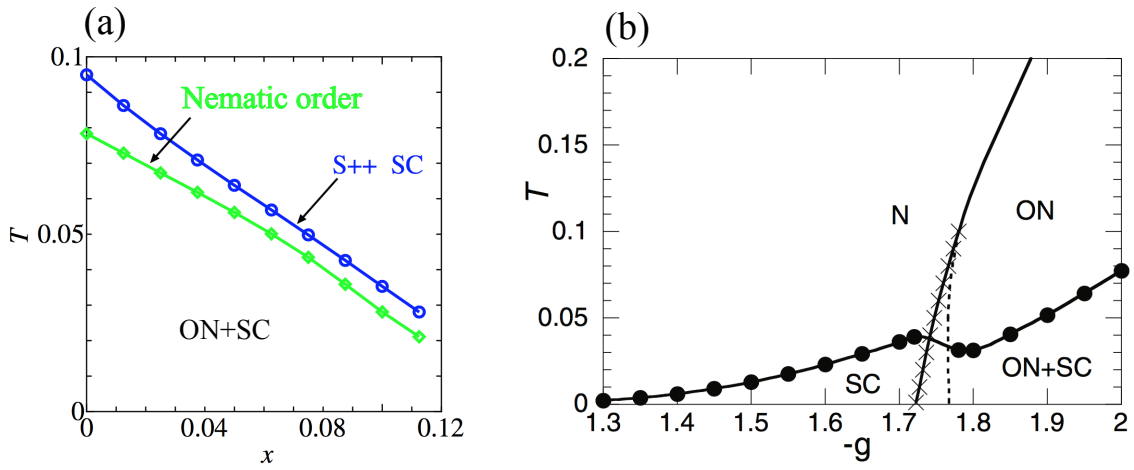

Figure 8: (a) Phase diagram obtained by Yanagi *et al.*[31]. The horizontal axis is doping x and the number of electrons per unit cell is given by $n = 24 + 2x$. The vertical axis is temperature T in units of eV. The blue and green lines denote the transition temperature, below which the s_{++}-wave superconductivity and orbital nematic order develop, respectively. (b) Phase diagram obtained by H. Yamase and R. Zeyher[32]. The horizontal axis is the strength of the orbital nematic interaction g, and the vertical axis is temperature T in units of their hopping integral t, which may be around 150 meV. There are four phases: Normal metallic phase (N), orbital nematic phase (ON), superconducting phase (SC) and coexistence of the orbital nematic and superconducting state (ON + SC). The line with filled circles denotes the superconducting transition line. The solid line denotes the orbital nematic transition line. In a region surrounded by the line with crosses and the dotted line, the orbital nematic phase becomes nonuniform.

(a) is their phase diagram, where the orbital nematic instability actually occurs in a wide region and superconducting instability appears just above the onset temperature of the orbital nematic order. This result clearly shows that orbital nematic fluctuations can drive superconductivity. However, their obtained T_c is unrealistically high [the energy units in Fig.8 (a) are eV] and moreover T_c is always higher than the nematic transition. These results sharply contradict with the typical phase diagram in FeSCs [Fig.4 (a) and (b)]: First, the observed T_c is not just above the nematic phase, and second, the superconductivity occurs not only outside the nematic phase, but also inside the nematic phase. The reason of these discrepancies likely lie in their crude approximation[30, 31]. They employed the Eliashberg theory[33], but completely neglected the self-energy effect of the electrons.

In 2013, H. Yamase and R. Zeyher[32] studied T_c of the superconductivity from orbital nematic fluctuations by employing the minimal two-band model. This model is much simpler than that by Y. Yanagi *et al.*[30, 31], and allowed them to study the self-energy effect and also to perform calculations down to very low temperature. Figure 8 (b) is their phase diagram in the plane of the strength of the orbital nematic interaction g and temperature T. They obtained T_c as high as that observed in experiments [the energy units in Fig.8 (b) are about 150 meV]. Moreover, the superconducting transition can also occur inside the nematic phase, similar to the typical phase diagram [Fig.4 (b)].

1.3 Motivation

In this thesis, we wish to explore further the superconducting mechanism due to orbital nematic fluctuations. This is motivated by the following considerations. First, since Ref.[32] implies that orbital nematic fluctuations can be a fully new mechanism of high-T_c superconductivity, it is worthwhile from a purely theoretical point of view to establish such a mechanism by clarifying the gap structure in the Eliashberg theory, which is the standard theory of superconductivity due to fluctuations. Second, the electronic nematic phase exists closer to the the superconducting phase than the SDW phase in FeSCs. Therefore we expect that the nematic fluctuations play an important for the high-T_c superconductivity. Third, a study in Ref.[32] assumed that the pairing gap is isotropic on each Fermi pocket and thus the momentum dependence of the pairing gap remains to be studied. In particular, the momentum depenence of the pairing gap can be observed directly by angle-resolved photoemission spectroscopy (ARPES), and thus the structure of the pairing gap is believed to be vital to identifying the superconducting mechanism. If we clarify the momentum dependence of the pairing gap, we can discuss more deeply possible superconductivity driven by the orbital nematic fluctuations in FeSCs through making a comparison with experimental data. Fourth, since the superconducting phase is realized close to both SDW and nematic phase, it is reasonable to assume that both spin fluctuations and orbital nematic fluctuations play some role to the superconducting

mechanism in the FeSCs. Hence it is very important to clarify a role of spin fluctuations in the same theoretical framework as the superconductivity from orbital nematic fluctuations. Such a work has not been done. Finally, a natural question arise about the interplay of orbital nematic fluctuations and spin fluctuations, for example, whether they work cooperatively to realize the superconductivity or not. This is a very interesting question and may shed an important light on the mechanism of high-T_c superconductivity in the FeSCs. The present thesis is motivated by those five considerations and we aim to provide theoretical insights into them.

Chapter 2

Theory and method

In this chapter, we first introduce our effective Hamiltonian, which describes electrons interacting with each other via orbital nematic interaction and spin interaction. We then derive susceptibilities associated with orbital nematic and spin fluctuations in the random phase approximation (RPA). To study whether those fluctuations can drive superconductivity, we employ the Eliashberg theory. We explain how to drive the linearized gap equations by including self-energy corrections. The Eliashberg equations are, however, too complicated to be solved numerically especially at low temperature. We then project momenta onto the Fermi pockets and simplify the equations to achieve numerical calculations down to low temperature to find a possible onset temperature of superconducting instability.

As explained in Section 1.2.1 the unit cell in FeSCs contains two irons. However, to simplify the calculations, we employ a unit cell containing only one iron. As a result, our model is defined on a square lattice where an iron sits on each site.

2.1 Hamiltonian

2.1.1 Kinetic term

Ab initio calculations showed that bands originating from all five d-orbitals of irons lie around the Fermi energy[34]. In particular, the bands from d_{xz}- and d_{yz}-orbitals play the major role in the orbital nematic physics. Hence we focus on d_{xz}- and d_{yz}-orbitals in the present thesis. Such a two-band model may be a minimal model especially for studying the orbital nematic physics in FeSCs. The kinetic term of the two-band model[16, 17] is given by

$$H_0 = \sum_{\mathbf{k},\sigma,\alpha,\beta} \xi_{\mathbf{k}}^{\alpha\beta} d_{\mathbf{k},\sigma,\alpha}^{\dagger} d_{\mathbf{k},\sigma,\beta} \,, \tag{1}$$

where $d_{\mathbf{k},\sigma,\alpha}^{\dagger}$ is a creation operator of an electron with momentum $\mathbf{k}$, spin σ, and orbital α. The orbital index $\alpha = 1, 2$ refers to the d_{xz}- and d_{yz}-orbitals, respectively. $\xi_{\mathbf{k}}^{\alpha\beta}$ is a

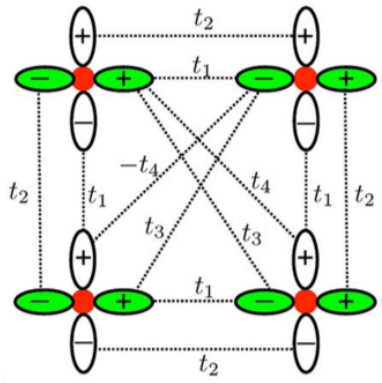

Figure 9: Hopping parameters in our two-band model[16]. The red circles are iron sites and the green (white) ellipses are the projections of the d_{xz}- (d_{yz}-) orbital onto the xy plane. t_1 and t_2 are the nearest-neighbor hoppings between the same orbital with σ bond and with π bond, respectively; t_3 and t_4 are the next-nearest-neighbor hoppings between the same and different orbitals, respectively.

tight binding dispersion of electrons and is given by

$$\xi^{11}_{\mathbf{k}} = -2t_1 \cos k_x - 2t_2 \cos k_y - 4t_3 \cos k_x \cos k_y - \mu, \tag{2}$$

$$\xi^{22}_{\mathbf{k}} = -2t_2 \cos k_x - 2t_1 \cos k_y - 4t_3 \cos k_x \cos k_y - \mu, \tag{3}$$

$$\xi^{12}_{\mathbf{k}} = \xi^{21}_{\mathbf{k}} = -4t_4 \sin k_x \sin k_y \,. \tag{4}$$

Here t_1, t_2, t_3 and t_4 are hopping integrals between irons as illustrated in Fig.9 and μ is the chemical potential. We choose the following parameters in this thesis,

$$\mu = 0.6t, \quad t_1 = -t, \quad t_2 = -1.5t, \quad t_3 = 1.2t, \quad t_4 = -0.95t, \tag{5}$$

which reproduce typical Fermi surfaces observed in FeSCs (Fig.10). In the following, all quantities with the dimension of energy are measured in units of t. The absolute value of t may be around $t = 150$ meV[15].

To find the Fermi surface, the Hamiltonian [Eq.(1)] should be written in the band representation, not in the orbital representation. We first write the Hamiltonian [Eq.(1)] in a matrix form

$$H_0 = \sum_{\mathbf{k},\sigma} (d^\dagger_{\mathbf{k},\sigma,1}, d^\dagger_{\mathbf{k},\sigma,2}) \begin{pmatrix} \xi^{11}_{\mathbf{k}} & \xi^{12}_{\mathbf{k}} \\ \xi^{12}_{\mathbf{k}} & \xi^{22}_{\mathbf{k}} \end{pmatrix} \begin{pmatrix} d_{\mathbf{k},\sigma,1} \\ d_{\mathbf{k},\sigma,2} \end{pmatrix} . \tag{6}$$

The eigenvalues of the matrix correspond to the energy bands

$$\lambda_{\mathbf{k},1} = \xi^+_{\mathbf{k}} + \sqrt{(\xi^-_{\mathbf{k}})^2 + (\xi^{12}_{\mathbf{k}})^2}, \tag{7}$$

$$\lambda_{\mathbf{k},2} = \xi^+_{\mathbf{k}} - \sqrt{(\xi^-_{\mathbf{k}})^2 + (\xi^{12}_{\mathbf{k}})^2}, \tag{8}$$

where

$$\xi^\pm_{\mathbf{k}} = \frac{1}{2} \left(\xi^{11}_{\mathbf{k}} \pm \xi^{22}_{\mathbf{k}} \right) . \tag{9}$$

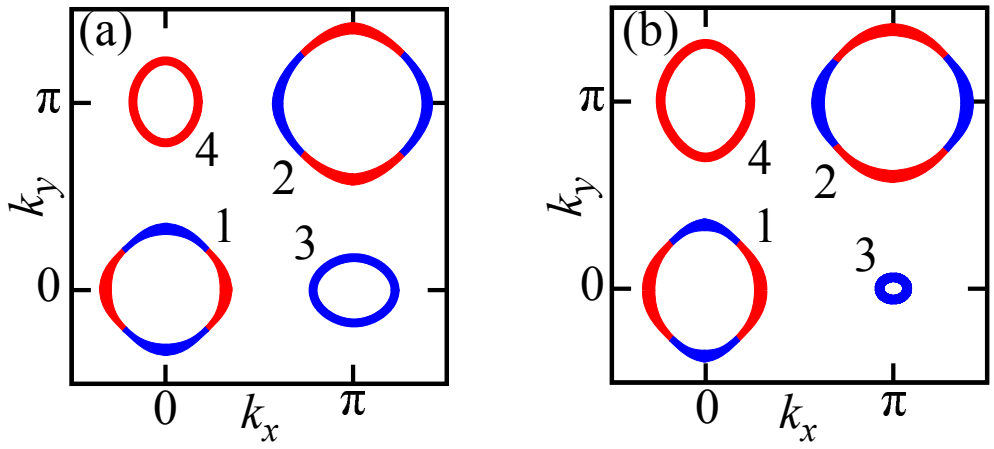

Figure 10: Typical Fermi surfaces in the minimal two-band model (a) in the normal metallic phase and (b) in the orbital nematic phase; we take $g/t = -1.8$, $n_- = 0.2271$ to describe the nematic phase. The d_{xz}- (d_{yz}-) orbital is dominant along the red (blue) curves and the line width depicts schematically the weight of each orbital. In the present thesis, we call each Fermi pocket as FS1, FS2, FS3, and FS4, respectively, as assigned by the number.

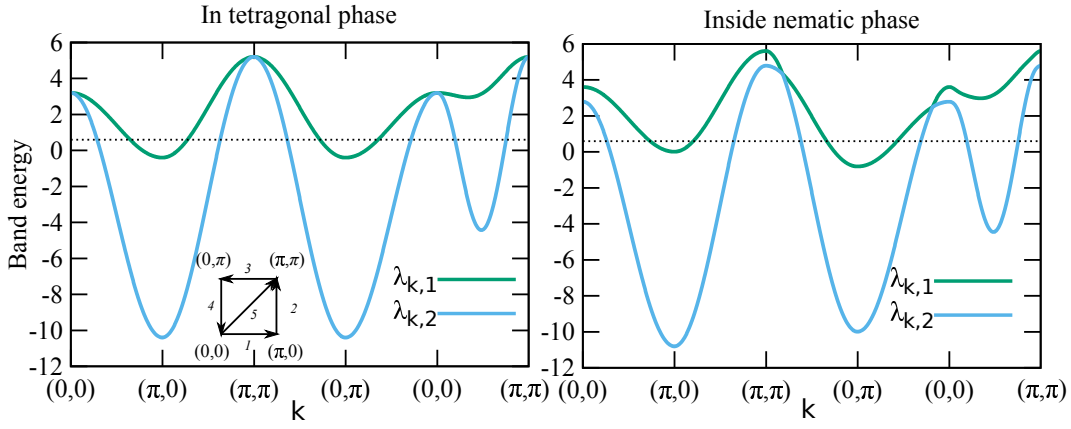

Figure 11: (a) Band dispersion $\lambda_{\mathbf{k},1}$ and $\lambda_{\mathbf{k},2}$ in the tetragonal phase along lines illustrated in the inset. (b) Band structure inside the nematic phase ($g/t = -1.8, n_- = 0.2271$). Note that the nematic order breaks the fourfold symmetry and thus the band dispersion along the $(0,0) - (\pi,0) - (\pi,\pi)$ direction becomes different from that along the $(\pi,\pi) - (0,\pi) - (0,0)$ direction. In addition, the nematic order lifts the degeneracy of $\lambda_{\mathbf{k},1}$ and $\lambda_{\mathbf{k},2}$ at $\mathbf{k} = (0,0)$ and (π,π). The dotted line denotes the Fermi energy.

The bands $\lambda_{\mathbf{k},1}$ and $\lambda_{\mathbf{k},2}$ are shown in Fig.11 (a). The band $\lambda_{\mathbf{k},1}$ forms two electron pockets around $\mathbf{k} = (\pi, 0)$ and $(0, \pi)$, corresponding to Fermi surfaces 3 and 4 (FS3 and FS4), respectively, in Fig.10 (a), whereas the band $\lambda_{\mathbf{k},2}$ forms two hole pockets around $\mathbf{k} = (0, 0)$ and (π, π) as shown in Fermi pockets 1 and 2 (FS1 and FS2) in Fig.10 (a). A unitary matrix $\hat{U}(\mathbf{k})$, which diagonalizes H_0, is easily calculated as

$$\begin{aligned}\hat{U}(\mathbf{k}) &= \begin{pmatrix} U_{11}(\mathbf{k}) & U_{12}(\mathbf{k}) \\ U_{21}(\mathbf{k}) & U_{22}(\mathbf{k}) \end{pmatrix}, \\ &= \frac{1}{\sqrt{\det \hat{U}(\mathbf{k})}} \begin{pmatrix} \xi^-_{\mathbf{k}} + \sqrt{\left(\xi^-_{\mathbf{k}}\right)^2 + \left(\xi^{12}_{\mathbf{k}}\right)^2} & \xi^{12}_{\mathbf{k}} \\ -\xi^{12}_{\mathbf{k}} & \xi^-_{\mathbf{k}} + \sqrt{\left(\xi^-_{\mathbf{k}}\right)^2 + \left(\xi^{12}_{\mathbf{k}}\right)^2} \end{pmatrix}, \end{aligned} \tag{10}$$

where $\det \hat{U}(\mathbf{k})$ is given by

$$\det \hat{U}(\mathbf{k}) = 2\sqrt{\left(\xi^-_{\mathbf{k}}\right)^2 + \left(\xi^{12}_{\mathbf{k}}\right)^2} \left(\xi^-_{\mathbf{k}} + \sqrt{\left(\xi^-_{\mathbf{k}}\right)^2 + \left(\xi^{12}_{\mathbf{k}}\right)^2} \right). \tag{11}$$

It is easy to check that the kinetic term is actually written as

$$H_0 = \sum_{\mathbf{k},\sigma} (c^\dagger_{\mathbf{k},\sigma,1}, c^\dagger_{\mathbf{k},\sigma,2}) \begin{pmatrix} \lambda_{\mathbf{k},1} & 0 \\ 0 & \lambda_{\mathbf{k},2} \end{pmatrix} \begin{pmatrix} c_{\mathbf{k},\sigma,1} \\ c_{\mathbf{k},\sigma,2} \end{pmatrix}, \tag{12}$$

where $c^\dagger_{\mathbf{k},\sigma,a}$ is a creation operator of an electron with the energy band $\lambda_{\mathbf{k},1}$ and $\lambda_{\mathbf{k},2}$ for $a = 1$ and 2, respectively. The new operator $c_{\mathbf{k},\sigma,a}$ is connected with the original operator $d_{\mathbf{k},\sigma,\alpha}$ by

$$\begin{aligned}\begin{pmatrix} d_{\mathbf{k},\sigma,1} \\ d_{\mathbf{k},\sigma,2} \end{pmatrix} &= \hat{U}(\mathbf{k}) \begin{pmatrix} c_{\mathbf{k},\sigma,1} \\ c_{\mathbf{k},\sigma,2} \end{pmatrix}, \\ &= \begin{pmatrix} U_{11}(\mathbf{k}) c_{\mathbf{k},\sigma,1} + U_{12}(\mathbf{k}) c_{\mathbf{k},\sigma,2} \\ U_{21}(\mathbf{k}) c_{\mathbf{k},\sigma,1} + U_{22}(\mathbf{k}) c_{\mathbf{k},\sigma,2} \end{pmatrix}. \end{aligned} \tag{13}$$

It is insightful to point out that the weight of each orbital component on the Fermi surfaces is described by the element of the unitary matrix $\hat{U}(\mathbf{k})$. We define a state $|n_1, n_2\rangle$, where there are n_1 electrons with the band energy $\lambda_{\mathbf{k},1}$ and n_2 electrons with $\lambda_{\mathbf{k},2}$. Then the electron number of the d_{xz}-orbital in the band $\lambda_{\mathbf{k},1}$ is computed to be

$$\langle 1, 0 | \, d^\dagger_{\mathbf{k},\sigma,1} d_{\mathbf{k},\sigma,1} \, | 1, 0 \rangle = U^2_{11}(\mathbf{k}). \tag{14}$$

Similarly the electron number of the d_{yz} orbital in the band $\lambda_{\mathbf{k},1}$ and that of the d_{xz} and d_{yz} orbital in the band $\lambda_{\mathbf{k},2}$ are obtained, respectively,

$$\langle 1, 0 | \, d^\dagger_{\mathbf{k},\sigma,2} d_{\mathbf{k},\sigma,2} \, | 1, 0 \rangle = U^2_{21}(\mathbf{k}), \tag{15}$$

$$\langle 0, 1 | \, d^\dagger_{\mathbf{k},\sigma,1} d_{\mathbf{k},\sigma,1} \, | 0, 1 \rangle = U^2_{12}(\mathbf{k}), \tag{16}$$

$$\langle 0, 1 | \, d^\dagger_{\mathbf{k},\sigma,2} d_{\mathbf{k},\sigma,2} \, | 0, 1 \rangle = U^2_{22}(\mathbf{k}). \tag{17}$$

The following relations

$$U_{11}^2(\mathbf{k}) + U_{21}^2(\mathbf{k}) = U_{12}^2(\mathbf{k}) + U_{22}^2(\mathbf{k}) = 1, \tag{18}$$

imply that $U_{11}^2(\mathbf{k})$ and $U_{21}^2(\mathbf{k})$ [$U_{12}^2(\mathbf{k})$ and $U_{22}^2(\mathbf{k})$] describe the ratio of the d_{xz}-orbital and d_{yz}-orbital in the band $\lambda_{\mathbf{k},1}$ ($\lambda_{\mathbf{k},2}$), respectively. Orbital components on each Fermi pocket is shown in Fig.10, where the d_{xz} (d_{yz}) orbital is dominant on the red (blue) curves and the thickness of the curves describes the weight of the corresponding orbital component schematically.

2.1.2 Orbital nematic interaction

While we shall consider both the orbital nematic interaction and the spin exchange interaction in this thesis, we first focus on the orbital nematic interaction. Its effective interaction H_1 was proposed by H. Yamase and R. Zeyher[32].

$$H_1 = \frac{g}{2} \sum_i n_{i-} n_{i-}, \tag{19}$$

where g is the strength of the orbital nematic interaction and

$$n_{i-} = n_{i,1} - n_{i,2}. \tag{20}$$

Here $n_{i,1}$ ($n_{i,2}$) is an operator of the electron number in the d_{xz} (d_{yz}) orbital, namely

$$n_{i,\alpha} = \sum_\sigma d_{i,\sigma,\alpha}^\dagger d_{i,\sigma,\alpha}. \tag{21}$$

If the expectation value of n_{i-} does not depend on i and becomes non-zero, we obtain $\langle n_{i,1} \rangle - \langle n_{i,2} \rangle \neq 0$, indicating that the occupation number in the d_{xz}-orbital becomes different from that in the d_{yz}-orbital. This implies that the system breaks the fourfold symmetry, but keeps the other symmetries unbroken. In this way, the electronic system acquires xy-anisotropy spontaneously due to the orbital order. We call such a state as the orbital nematic state, referring to the nematic liquid state, where only the orientational symmetry is broken. This state was originally proposed for $Sr_3Ru_2O_7$[35, 36] and was applied to FeSCs[26, 27, 28, 32], respectively.

Since the kinetic term is written in momentum space, we transform the interaction Eq.(19) in momentum space:

$$d_{i,\sigma,\alpha} = \frac{1}{\sqrt{N}} \sum_{\mathbf{k}} d_{\mathbf{k},\sigma,\alpha} e^{i\mathbf{k}\cdot\mathbf{r}_i}, \tag{22}$$

where N is the total number of lattice sites and $\mathbf{r}_i$ is the position of the i site. The resulting orbital nematic interaction is

$$H_1 = \frac{g}{2N} \sum_{\mathbf{q}} n_-(\mathbf{q}) n_-(-\mathbf{q}), \tag{23}$$

where

$$n_-(\mathbf{q}) = \sum_i n_{i-} e^{-i\mathbf{q}\cdot\mathbf{r}_i},$$
$$= \sum_{\mathbf{k},\sigma} (d^\dagger_{\mathbf{k},\sigma,1} d_{\mathbf{k}+\mathbf{q},\sigma,1} - d^\dagger_{\mathbf{k},\sigma,2} d_{\mathbf{k}+\mathbf{q},\sigma,2}). \tag{24}$$

It is convenient to rewrite Eq.(23) in the band representation by using the unitary matrix Eq.(10). As a result, $n_-(\mathbf{q})$ is written as

$$n_-(\mathbf{q}) = \sum_{\mathbf{k},\sigma} \sum_{a,b} V_{a,b}(\mathbf{k}, \mathbf{k}+\mathbf{q}) c^\dagger_{\mathbf{k},\sigma,a} c_{\mathbf{k}+\mathbf{q},\sigma,b}, \tag{25}$$

where

$$V_{a,b}(\mathbf{k}, \mathbf{k}') = \sum_{\alpha\beta} U^\dagger_{a,\alpha}(\mathbf{k}) (\tau_3)_{\alpha\beta} U_{\beta,b}(\mathbf{k}'), \tag{26}$$

$$\hat{\tau_3} = \begin{pmatrix} 1 & 0 \\ 0 & -1 \end{pmatrix}. \tag{27}$$

This $V_{a,b}(\mathbf{k}, \mathbf{k}')$ has the following relationships:

$$V_{a,b}(\mathbf{k}, \mathbf{k}') = V_{b,a}(\mathbf{k}', \mathbf{k}), \tag{28}$$
$$V_{a,b}(\mathbf{k}, \mathbf{k}') = V_{a,b}(\mathbf{k}, -\mathbf{k}'), \tag{29}$$
$$= V_{a,b}(-\mathbf{k}, \mathbf{k}'), \tag{30}$$
$$= V_{a,b}(-\mathbf{k}, -\mathbf{k}').. \tag{31}$$

The interaction part H_1 [Eq.(19)] becomes

$$H_1 = \frac{g}{2N} \sum_{a,b,c,d} \sum_{\mathbf{k},\mathbf{k}',\mathbf{q}} \sum_{\sigma,\sigma'} V_{a,b}(\mathbf{k}, \mathbf{k}+\mathbf{q}) V_{c,d}(\mathbf{k}'+\mathbf{q}, \mathbf{k}') c^\dagger_{\mathbf{k},\sigma,a} c_{\mathbf{k}+\mathbf{q},\sigma,b} c^\dagger_{\mathbf{k}'+\mathbf{q},\sigma',c} c_{\mathbf{k}',\sigma',d}. \tag{32}$$

2.1.3 Spin interaction

Next, we consider a spin interaction term, which should capture the typical magnetic property in FeSCs. As discussed in Section.1.2.2, FeSCs are metallic even in the magnetic phase. Hence we may consider the spin exchange interaction in momentum space:

$$H_2 = \frac{1}{2N} \sum_{\mathbf{q}} J(\mathbf{q}) \mathbf{S}(\mathbf{q}) \cdot \mathbf{S}(-\mathbf{q}), \tag{33}$$

where $\mathbf{S}(\mathbf{q})$ is an operator of total spin of the electronic system and is defined as

$$\mathbf{S}(\mathbf{q}) = \frac{1}{2} \sum_{\mathbf{k},\sigma,\sigma'} \sum_{\alpha} d^\dagger_{\mathbf{k},\sigma,\alpha} \boldsymbol{\sigma}_{\sigma\sigma'} d_{\mathbf{k}+\mathbf{q},\sigma',\alpha}, \tag{34}$$

where $\boldsymbol{\sigma} = (\sigma^x, \sigma^y, \sigma^z)$ are Pauli matrices

$$\sigma^x = \begin{pmatrix} 0 & 1 \\ 1 & 0 \end{pmatrix}, \quad \sigma^y = \begin{pmatrix} 0 & -i \\ i & 0 \end{pmatrix}, \quad \sigma^z = \begin{pmatrix} 1 & 0 \\ 0 & -1 \end{pmatrix}. \tag{35}$$

Note that the summation with respect to the orbital index α is taken in Eq.(34).

We need to specify a functional form of $J(\mathbf{q})$. Its minimal requirement may be that $J(\mathbf{q})$ shows a peak at $\mathbf{q} = (\pm\pi, 0)$ and $(0, \pm\pi)$ and that its sign becomes negative there, so that our model captures the actual magnetic structure in FeSCs, namely the stripe-type antiferromagnetic order as shown in Fig.3 (b). We consider two different forms of $J(\mathbf{q})$, Lorentz-type $J_\Gamma(\mathbf{q})$ and $J_1 - J_2$-type $J_{12}(\mathbf{q})$, both of which fulfill our minimal requirement.

i) Lorentz-type $J_\Gamma(\mathbf{q})$

The Lorentz-type $J_\Gamma(\mathbf{q})$ is defined as

$$J_\Gamma(\mathbf{q}) = -2J \left[\frac{\Gamma}{(q_x - \pi)^2 + q_y^2 + \Gamma^2} + \frac{\Gamma}{(q_x + \pi)^2 + q_y^2 + \Gamma^2} + \right. \\ \left. \frac{\Gamma}{(q_y - \pi)^2 + q_x^2 + \Gamma^2} + \frac{\Gamma}{(q_y + \pi)^2 + q_x^2 + \Gamma^2} \right]. \quad (36)$$

It is clear that $J_\Gamma(\mathbf{q})$ has a peak at $\mathbf{q} = (\pm\pi, 0)$ and $(0, \pm\pi)$ and its peak width is determined by Γ; the magnitude of $J_\Gamma(\mathbf{q})$ is scaled by the prefactor J. In the present thesis, we fix $\Gamma = 1$. We consider the Lorentz-type $J_\Gamma(\mathbf{q})$ as an appropriate form in the itinerant limit or the weak-coupling limit in the sense that the functional form of $J_\Gamma(\mathbf{q})$ is defined in momentum space. In other words, $J_\Gamma(\mathbf{q})$ leads to an exponential-like decay of spin exchange interaction in real space.

ii) $J_1 - J_2$ -type $J_{12}(\mathbf{q})$

As the opposite limit to the case of $J_\Gamma(\mathbf{q})$, we may also consider a spin exchange interaction from a real space point of view:

$$H_2 = \frac{1}{2} \sum_{\langle i,j \rangle} J_1 \mathbf{S}_i \cdot \mathbf{S}_j + \frac{1}{2} \sum_{\langle\langle i,j \rangle\rangle} J_2 \mathbf{S}_i \cdot \mathbf{S}_j, \quad (37)$$

where $\langle i,j \rangle$ denotes the nearest-neighbor pairs of iron sites, $\langle\langle i,j \rangle\rangle$ the next-nearest-neighbor pairs, and

$$\mathbf{S}_i = \frac{1}{2} \sum_\alpha \sum_{\sigma,\sigma'} d^\dagger_{i,\sigma,\alpha} \boldsymbol{\sigma}_{\sigma,\sigma'} d_{i,\sigma',\alpha} = \frac{1}{N} \sum_{\mathbf{q}} \mathbf{S}(\mathbf{q}) e^{i\mathbf{q}\cdot\mathbf{r}_i}. \quad (38)$$

The spin interaction [Eq.(37)] then becomes

$$H_2 = \frac{1}{2N} \sum_{\mathbf{q}} J_{12}(\mathbf{q}) \mathbf{S}(\mathbf{q}) \cdot \mathbf{S}(-\mathbf{q}), \quad (39)$$

where

$$J_{12}(\mathbf{q}) = 2[J_1(\cos q_x + \cos q_y) + 2J_2 \cos q_x \cos q_y]. \quad (40)$$

This $J_1 - J_2$-type interaction is frequently studied in the frustrated system[37]. In the present thesis we fix $J_1/t = 1$ and vary J_2 to control the strength of spin interaction. In

this case $J_{12}(\mathbf{q})$ has a peak at $\mathbf{q}=(\pm\pi,0)$ and $(0,\pm\pi)$ in $J_2/t \geq 0.5$, although the peak shifts to $\mathbf{q}=(\pm\pi,\pm\pi)$ for small J_2/t (≤ 0.5). Since we are mainly interested in a region near SDW phase, where J_2/t is larger than 0.5, our $J_{12}(\mathbf{q})$ may be regarded as the spin interaction in the localized limit, the opposite limit to the case of $J_\Gamma(\mathbf{q})$ [Eq.(36)].

For latter convenience, we write the spin interaction H_2 [Eq.(33)] in the band representation by using the unitary matrix $\hat{U}(\mathbf{k})$ [Eq.(10)]. The Hamiltonian H_2 consists of the longitudinal spin interaction (H_2^{zz}) and the transverse spin interaction ($H_2^{\pm}$)

$$H_2 = H_2^{zz} + H_2^{\pm}, \tag{41}$$

$$H_2^{zz} = \frac{1}{2N}\sum_{\mathbf{q}} J(\mathbf{q}) S^z(\mathbf{q}) S^z(-\mathbf{q}), \tag{42}$$

$$H_2^{\pm} = \frac{1}{4N}\sum_{\mathbf{q}} J(\mathbf{q}) [S^+(\mathbf{q}) S^-(-\mathbf{q}) + S^-(\mathbf{q}) S^+(-\mathbf{q})], \tag{43}$$

where $S^{\pm}(\mathbf{q}) = S^x(\mathbf{q}) \pm i S^y(\mathbf{q})$. Using Eq.(13), the spin operators are written as

$$S^z(\mathbf{q}) = \sum_{\mathbf{k}}\sum_{\sigma}\sum_{a,b} W_{a,b}(\mathbf{k},\mathbf{k}+\mathbf{q})\frac{\sigma}{2} c^\dagger_{\mathbf{k},\sigma,a} c_{\mathbf{k}+\mathbf{q},\sigma,b}, \tag{44}$$

$$S^+(\mathbf{q}) = \sum_{\mathbf{k}}\sum_{a,b} W_{a,b}(\mathbf{k},\mathbf{k}+\mathbf{q}) c^\dagger_{\mathbf{k},\uparrow,a} c_{\mathbf{k}+\mathbf{q},\downarrow,b}, \tag{45}$$

$$S^-(\mathbf{q}) = \sum_{\mathbf{k}}\sum_{a,b} W_{a,b}(\mathbf{k},\mathbf{k}+\mathbf{q}) c^\dagger_{\mathbf{k},\downarrow,a} c_{\mathbf{k}+\mathbf{q},\uparrow,b}, \tag{46}$$

$$W_{a,b}(\mathbf{k},\mathbf{k}') = \sum_{\alpha,\beta} U^\dagger_{a,\alpha}(\mathbf{k})(\tau_0)_{\alpha\beta} U_{\beta,b}(\mathbf{k}'). \tag{47}$$

The form factor $W_{a,b}(\mathbf{k},\mathbf{k}')$ includes $\tau_0 = \begin{pmatrix} 1 & 0 \\ 0 & 1 \end{pmatrix}$, which is different from the case of the orbital nematic interaction [see Eq.(26)]. The resulting H_2^{zz} and $H_2^{\pm}$ become

$$H_2^{zz} = \frac{1}{2N}\sum_{\mathbf{q},\mathbf{k},\mathbf{k}'}\sum_{\sigma,\sigma'}\sum_{a,b,c,d} J(\mathbf{q})\frac{\sigma}{2} W_{a,b}(\mathbf{k},\mathbf{k}+\mathbf{q})\frac{\sigma'}{2} W_{c,d}(\mathbf{k}'+\mathbf{q},\mathbf{k}') c^\dagger_{\mathbf{k},\sigma,a} c_{\mathbf{k}+\mathbf{q},\sigma,b} c^\dagger_{\mathbf{k}'+\mathbf{q},\sigma',c} c_{\mathbf{k}',\sigma',d}, \tag{48}$$

$$H_2^{\pm} = \frac{1}{2N}\sum_{\mathbf{q},\mathbf{k},\mathbf{k}'}\sum_{a,b,c,d} J(\mathbf{q}) W_{a,b}(\mathbf{k},\mathbf{k}+\mathbf{q}) W_{c,d}(\mathbf{k}'+\mathbf{q},\mathbf{k}') c^\dagger_{\mathbf{k},a,\uparrow} c_{\mathbf{k}+\mathbf{q},b,\downarrow} c^\dagger_{\mathbf{k}'+\mathbf{q},c,\downarrow} c_{\mathbf{k}',d,\uparrow}. \tag{49}$$

Note that the vertex Eq.(47) has the following properties:

$$W_{a,b}(\mathbf{k},\mathbf{k}') = W_{b,a}(\mathbf{k}',\mathbf{k}), \tag{50}$$

$$W_{a,b}(\mathbf{k},\mathbf{k}') = W_{a,b}(-\mathbf{k},\mathbf{k}'), \tag{51}$$

$$= W_{a,b}(\mathbf{k},-\mathbf{k}'), \tag{52}$$

$$= W_{a,b}(-\mathbf{k},-\mathbf{k}'),, \tag{53}$$

which are the same properties as Eqs.(28)-(31).

2.2 Mean-field approximation

Our total Hamiltonian consists of three terms

$$H = H_0 + H_1 + H_2, \tag{54}$$

where H_0, H_1, and H_2 are defined in Eqs.(6), (19), and (33) in the orbital representation, respectively, and in Eqs.(12), (32), and (48)-(49) in the band representation, respectively. This Hamiltonian can yield not only superconducting instability but also orbital nematic and SDW instabilities. Before analyzing superconductivity, we first study orbital nematic and SDW instabilities in mean-field theory and determine the phase diagram.

We first focus on the orbital nematic instability. The Hamiltonian reads

$$H^{\mathrm{ON}} = \sum_{\mathbf{k},\sigma,\alpha,\beta} \xi_{\mathbf{k}}^{\alpha\beta} d_{\mathbf{k},\sigma,\alpha}^{\dagger} d_{\mathbf{k},\sigma,\beta} + \frac{g}{2} \sum_i n_{i-} n_{i-}, \tag{55}$$

in the orbital representation. We decouple the interaction term by introducing the mean field $\langle n_{i-} \rangle$,

$$\frac{g}{2} \sum_i n_{i-} n_{i-} \simeq g \sum_i \left[\langle n_{i-} \rangle n_{i-} - \frac{g}{2} \langle n_{i-} \rangle^2 \right] \tag{56}$$

$$= g n_- \sum_{\mathbf{k},\sigma} (d_{\mathbf{k},\sigma,1}^{\dagger} d_{\mathbf{k},\sigma,1} - d_{\mathbf{k},\sigma,2}^{\dagger} d_{\mathbf{k},\sigma,2}) - \frac{g}{2} N (n_-)^2. \tag{57}$$

In the second line we assume that the mean field is uniform, namely $\langle n_{i-} \rangle = n_-$. This assumption is actually good as we discuss in Fig.29 in Section.3. The resulting mean-field Hamiltonian is

$$H_{\mathrm{MF}}^{\mathrm{ON}} = \sum_{\mathbf{k},\sigma} (d_{\mathbf{k},\sigma,1}^{\dagger}, d_{\mathbf{k},\sigma,2}^{\dagger}) \begin{pmatrix} \xi_{\mathbf{k},1} & \xi_{\mathbf{k}}^{12} \\ \xi_{\mathbf{k}}^{12} & \xi_{\mathbf{k},2} \end{pmatrix} \begin{pmatrix} d_{\mathbf{k},\sigma,1} \\ d_{\mathbf{k},\sigma,2} \end{pmatrix} - \frac{g}{2} N (n_-)^2, \tag{58}$$

where

$$\xi_{\mathbf{k},1} = \xi_{\mathbf{k}}^{11} + g n_-, \quad \xi_{\mathbf{k},2} = \xi_{\mathbf{k}}^{22} - g n_-. \tag{59}$$

Formally this expression is the same as the kinetic term Eq.(6). The only differences are $\xi_{\mathbf{k}}^{11}$ and $\xi_{\mathbf{k}}^{22}$ acquire the contribution of the orbital nematic order with the opposite sign.

Writing the inverse of temperature as $\beta = T^{-1}$, we can easily calculate the grand canonical potential Ω for the mean-field Hamiltonian [Eq.(58)]

$$e^{-\beta\Omega} = \mathrm{Tr} e^{-\beta H_{\mathrm{MF}}^{\mathrm{ON}}}$$

$$= \prod_{\mathbf{k},\sigma} (1 + e^{-\beta\lambda_{\mathbf{k},1}})(1 + e^{-\beta\lambda_{\mathbf{k},2}}) e^{\frac{\beta g N (n_-)^2}{2}}, \tag{60}$$

that is,

$$\Omega = -\frac{2}{\beta} \sum_{\mathbf{k}} [\log(1 + e^{-\beta\lambda_{\mathbf{k},1}}) + \log(1 + e^{-\beta\lambda_{\mathbf{k},2}})] - \frac{g}{2} N (n_-)^2. \tag{61}$$

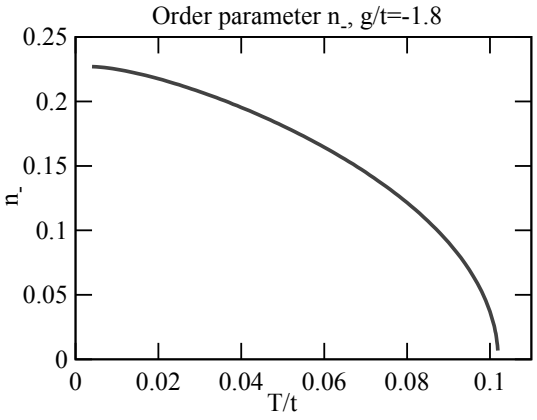

Figure 12: Temperature dependence of order parameter of the orbital nematic state ($g/t = -1.8$).

The self-consistency equation is determined by the condition

$$\frac{\partial \Omega}{\partial n_-} = 0. \tag{62}$$

which yields

$$n_- = \frac{2}{N}\sum_{\mathbf{k}} \frac{\xi^-_{\mathbf{k}}}{\sqrt{(\xi^-_{\mathbf{k}})^2 + (\xi^{12}_{\mathbf{k}})^2}}[f(\lambda_{\mathbf{k},1}) - f(\lambda_{\mathbf{k},2})]. \tag{63}$$

Here $f(x)$ is the Fermi distribution function,

$$f(x) = \frac{1}{e^{\beta x}+1}. \tag{64}$$

Solving Eq.(63), we determine a value of the mean-field. We find that n_- can become finite for $g/t \leq -1.76$, where the orbital nematic phase is stabilized (see details Fig.29 in Section 3). Figure 12 is the temperature dependence of n_- for $g/t = -1.8$. Using the value of n_- at each temperature, we can easily obtain the band dispersion [Fig.11 (b)] and Fermi surfaces as well as the weight of the orbital components there [Eqs.(28)-(31)] [Fig.10 (b)]. In the nematic phase ($n_- > 0$), the d_{xz}-orbital is occupied more than the d_{yz}-orbital. As a result, FS3 in Fig.10 (b) substantially shrinks and can disappear for a larger n_-, whereas FS1 and FS4 expand along the k_y direction; FS2, on the other hand, slightly expands along the k_x direction for the parameter in Fig.10 (b). The band dispersion necessarily becomes anisotropic between the $(0,0)-(\pi,0)-(\pi,\pi)$ direction and the $(0,0)-(0,\pi)-(\pi,\pi)$ direction as shown in Fig.11 (b). In addition, the nematic order lifts the band degeneracy at $\mathbf{k} = (0,0)$ and (π,π).

For the SDW order we may employ the following Hamiltonian

$$H^{\rm SDW} = \sum_{\mathbf{k},\sigma}\sum_{\alpha,\beta} \varepsilon^{\alpha\beta}_{\mathbf{k}} d^\dagger_{\mathbf{k},\sigma,\alpha} d_{\mathbf{k},\sigma,\beta} + \frac{1}{2N}\sum_{\mathbf{q}} J(\mathbf{q})\mathbf{S}(\mathbf{q})\cdot\mathbf{S}(-\mathbf{q}). \tag{65}$$

When we introduce a mean-field order such as

$$\langle S^z(\mathbf{Q})\rangle = m e^{i\mathbf{Q}\cdot\mathbf{r}} \tag{66}$$

for $\mathbf{Q} = (\pm\pi, 0), (0, \pm\pi)$ and decouple the interaction term, we would then obtain the mean-field Hamiltonian. However, it turns out that the assumption of $\mathbf{Q} = (\pm\pi, 0)$ and $(0, \pm\pi)$ is not valid in a low temperature region that we are interested in. In such a region, the SDW order tends to become *incommensurate*, that is, its modulation vector slightly shifts from $(\pm\pi, 0)$ and $(0, \pm\pi)$ in a whole parameter region where we study superconducting instability in the present thesis. In addition, we do not consider a possible superconducting instability inside the SDW phase in the present thesis. Therefore instead of determing the SDW order parameter, we determine the SDW phase boundary by computing the static spin susceptibility in the RPA as we shall show in Section 3.2,

2.3 Susceptibilities in RPA

We derive the orbital nematic susceptibility and the spin susceptibility in the Matsubara formalism in the RPA. These susceptibilities play a role of glues of Cooper pairing in the Eliashberg theory as we shall explain in Section 2.4. Moreover the static limit of those susceptibilities determines the phase boundary of the orbital nematic order, SDW order, and their possible incommensurate orders.

2.3.1 Orbital nematic susceptibility

The orbital nematic susceptibility is defined as

$$\chi^{\mathrm{ON}}(\mathbf{q}, iq_m) = \frac{1}{N}\int_0^\beta d\tau e^{iq_m\tau}\langle T_\tau n_-(\mathbf{q},\tau)n_-(-\mathbf{q},0)\rangle, \tag{67}$$

where T_τ is the time-order operator, and $q_m = 2m\pi T$ is bosonic Matsubara frequency with m being an integer. The τ dependence of operators $A(\mathbf{q},\tau) = e^{\tau H_0}A(\mathbf{q})e^{-\tau H_0}$ and the expectation value are defined, respectively, as

$$\langle A\rangle = \frac{\mathrm{Tr}Ae^{-\beta H^{\mathrm{ON}}}}{\mathrm{Tr}e^{-\beta H^{\mathrm{ON}}}}. \tag{68}$$

We calculate the susceptibility using a diagramatic method in the RPA. The orbital nematic interaction Eq.(23) is described in Fig.13 diagrammatically. The wavy line is the bare interaction g, the open circles are the vertex $V_{a,b}(\mathbf{k}, \mathbf{k}+\mathbf{q})$ [see Eq.(26)], and the lines with an arrow are the bare Green's functions. Note that we here use the band representation and thus the kinetic term is already diagonalized [Eq.(12)]. Therefore the bare Green's function is also diagonalized to be

$$\begin{aligned}\hat{\mathcal{G}}^{(0)}(\mathbf{k}, ik_n) &= \begin{pmatrix} \mathcal{G}^{(0)}_{11}(\mathbf{k}, ik_n) & \mathcal{G}^{(0)}_{12}(\mathbf{k}, ik_n) \\ \mathcal{G}^{(0)}_{21}(\mathbf{k}, ik_n) & \mathcal{G}^{(0)}_{22}(\mathbf{k}, ik_n)\end{pmatrix}, \\ &= \begin{pmatrix} \dfrac{1}{ik_n - \lambda_{\mathbf{k},1}} & 0 \\ 0 & \dfrac{1}{ik_n - \lambda_{\mathbf{k},2}}\end{pmatrix},\end{aligned} \tag{69}$$

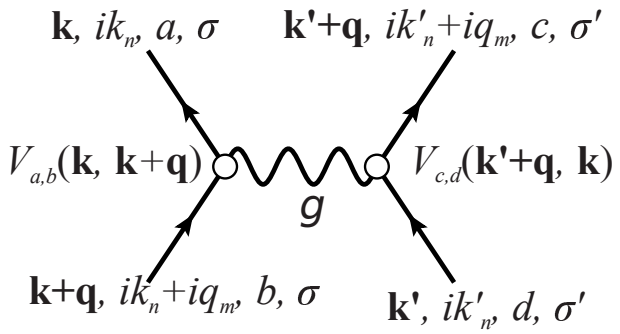

Figure 13: Diagramatic representation of the orbital nematic interaction [see Eq.(23)]. The line with an arrow is the bare Green's function and the wavy line is the orbital nematic interaction. The white circle denotes the vertex $V_{a,b}(\mathbf{k},\mathbf{k}')$.

where k_n is fermionic Matsubara frequency $k_n = (2n-1)\pi T$ and n is an integer.

In the RPA, $\chi^{\rm ON}$ is computed as a series of bubble diagrams as shown in Fig.14. Writing the single bubble as $-\chi_0^{\rm ON}(\mathbf{q}, iq_m)$, we obtain the RPA susceptibility:

$$-\chi^{\rm ON}(\mathbf{q},iq_m) = -\chi_0^{\rm ON}(\mathbf{q},iq_m) + [-\chi_0^{\rm ON}(\mathbf{q},iq_m)g\chi_0^{\rm ON}(\mathbf{q},iq_m)] + [-\chi_0^{\rm ON}(\mathbf{q},iq_m)g\chi_0^{\rm ON}(\mathbf{q},iq_m)g\chi_0^{\rm ON}(\mathbf{q},iq_m)] + \cdots \quad (70)$$

$$= -\chi_0^{\rm ON}(\mathbf{q},iq_m)\left\{1 + [-g\chi_0^{\rm ON}(\mathbf{q},iq_m)] + [-g\chi_0^{\rm ON}(\mathbf{q},iq_m)]^2 + \cdots\right\} \quad (71)$$

$$= -\frac{\chi_0^{\rm ON}(\mathbf{q},iq_m)}{1+g\chi_0^{\rm ON}(\mathbf{q},iq_m)}. \quad (72)$$

If we put $g=0$, we would obtain $\chi^{\rm ON}(\mathbf{q},iq_m) = \chi_0^{\rm ON}(\mathbf{q},iq_m)$. Hence $\chi_0^{\rm ON}(\mathbf{q},iq_m)$ is often called as the bare susceptibility. Since $\chi_0^{\rm ON}(\mathbf{q},iq_m)$ corresponds to the single bubble, its explicit form is easily computed by using the bare Green's function because Eq.(69) is already diagonalized. That is,

$$\chi_0^{\rm ON}(\mathbf{q},iq_m)$$

$$= \frac{1}{N}\int_0^\beta d\tau e^{iq_m\tau}\langle T_\tau n_-(\mathbf{q},\tau)n_-(-\mathbf{q},0)\rangle_0 \quad (73)$$

$$= -\frac{1}{\beta N}\sum_{\mathbf{k},n,\sigma}\sum_{a,b,c,d}\mathcal{G}^{(0)}_{c,a}(\mathbf{k},ik_n)V_{a,b}(\mathbf{k},\mathbf{k}+\mathbf{q})\mathcal{G}^{(0)}_{b,d}(\mathbf{k}+\mathbf{q},ik_n+iq_m)V_{d,c}(\mathbf{k}+\mathbf{q},\mathbf{k}), \quad (74)$$

$$= -\frac{2}{N}\sum_{\mathbf{k}}\left\{C^+_{\mathbf{k},\mathbf{k}+\mathbf{q}}\left[\frac{f(\lambda_{\mathbf{k}+\mathbf{q},1})-f(\lambda_{\mathbf{k},1})}{\lambda_{\mathbf{k}+\mathbf{q},1}-\lambda_{\mathbf{k},1}-iq_m} + \frac{f(\lambda_{\mathbf{k}+\mathbf{q},2})-f(\lambda_{\mathbf{k},2})}{\lambda_{\mathbf{k}+\mathbf{q},2}-\lambda_{\mathbf{k},2}-iq_m}\right] + C^-_{\mathbf{k},\mathbf{k}+\mathbf{q}}\left[\frac{f(\lambda_{\mathbf{k}+\mathbf{q},1})-f(\lambda_{\mathbf{k},2})}{\lambda_{\mathbf{k}+\mathbf{q},1}-\lambda_{\mathbf{k},2}-iq_m} + \frac{f(\lambda_{\mathbf{k}+\mathbf{q},1})-f(\lambda_{\mathbf{k},2})}{\lambda_{\mathbf{k}+\mathbf{q},1}-\lambda_{\mathbf{k},2}+iq_m}\right]\right\}, \quad (75)$$

where

$$C^\pm_{\mathbf{k},\mathbf{k}+\mathbf{q}} = \frac{1}{2}\left(1 \pm \frac{\xi^-_{\mathbf{k}}\xi^-_{\mathbf{k}+\mathbf{q}} - \xi^{12}_{\mathbf{k}}\xi^{12}_{\mathbf{k}+\mathbf{q}}}{\sqrt{(\xi^-_{\mathbf{k}})^2+(\xi^{12}_{\mathbf{k}})^2}\sqrt{(\xi^-_{\mathbf{k}+\mathbf{q}})^2+(\xi^{12}_{\mathbf{k}+\mathbf{q}})^2}}\right). \quad (76)$$

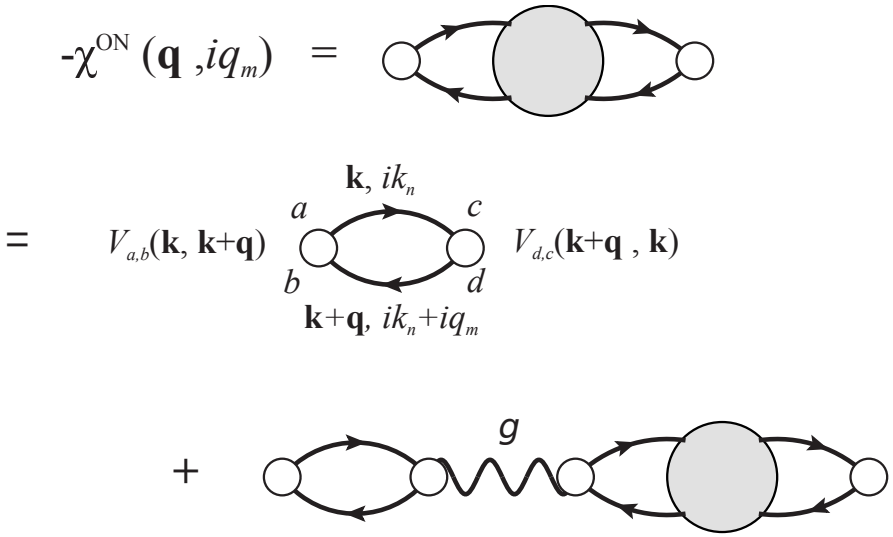

Figure 14: The orbital nematic susceptibility in the RPA. The line with an arrow is the bare Green's function of electrons, and the white circle is the vertex Eq.(26). The wavy line is the bare orbital nematic interaction.

After the analytical continuation, $iq_m \to \omega + i\eta$ with $\eta = +0$, we obtain the dynamical susceptibility. In particular, in the static limit, $\chi^{\rm ON}(\mathbf{q}, 0)$ corresponds to the static orbital nematic susceptibility.

2.3.2 Spin susceptibility

There are two spin susceptibilities: longitudinal and transverse ones. We first consider the longitudinal spin susceptibility

$$\chi^{zz}(\mathbf{q}, iq_m) = \int_0^\beta d\tau e^{iq_m\tau} \langle T_\tau S^z(\mathbf{q}, \tau) S^z(-\mathbf{q}, 0)\rangle. \tag{77}$$

In the band representation, the longitudinal spin interaction is given in Eq.(48), which can be written diagrammatically in Fig.15. The black circles denote vertexes Eq.(44) and the spring is the bare spin interaction $J(\mathbf{q})$.

Similar to the case of the orbital nematic susceptibility, the longitudinal spin susceptibility in the RPA is described by a series of the simple bubble connected by the spin interaction as shown in Fig.16. Writing the single bubble as $-\chi_0^{zz}(\mathbf{q}, iq_m)$, we obtain

$$-\chi^{zz}(\mathbf{q}, iq_m) = -\chi_0^{zz}(\mathbf{q}, iq_m) \left\{1 + [-J(\mathbf{q})\chi_0^{zz}(\mathbf{q}, iq_m)] + [-J(\mathbf{q})\chi_0^{zz}(\mathbf{q}, iq_m)]^2 + \cdots\right\} \tag{78}$$

$$= -\frac{\chi_0^{zz}(\mathbf{q}, iq_m)}{1 + J(\mathbf{q})\chi_0^{zz}(\mathbf{q}, iq_m)}. \tag{79}$$

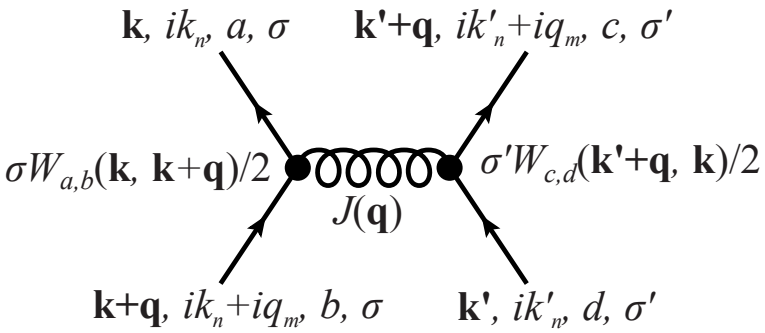

Figure 15: Diagrammatic representation of the longitudinal component of the spin interaction [see Eq.(48)]. The line with an arrow are the bare Green's function of electrons, the black circle the vertex $\frac{\sigma}{2}W_{a,b}(\mathbf{k},\mathbf{k}')$, and the spring the bare spin interaction $J(\mathbf{q})$.

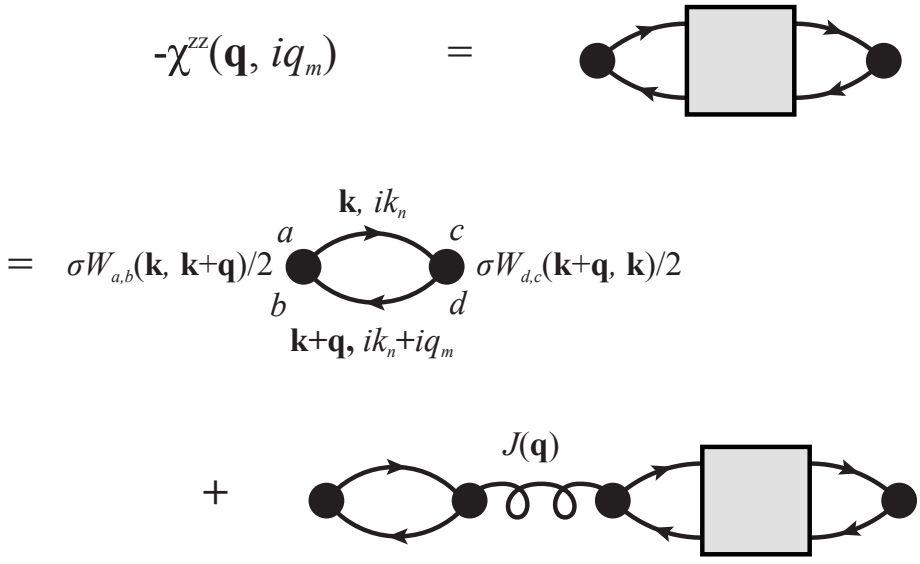

Figure 16: Diagrammatic representation of the longitudinal spin susceptibility in the RPA. The line with an arrow is the bare Green's funtion of electrons, the black filled circle the vertex Eq.(47), and the spring the bare spin interaction.

The bare spin susceptibility $\chi_0^{zz}(\mathbf{q}, iq_m)$ is easily computed from Eqs.(47) and (69):

$$\chi_0^{zz}(\mathbf{q}, iq_m) = \int_0^\beta d\tau e^{iq_m\tau}\langle T_\tau S^z(\mathbf{q},\tau)S^z(-\mathbf{q},0)\rangle_0 \tag{80}$$

$$= -\frac{1}{\beta N}\sum_{\mathbf{k},n,\sigma}\sum_{a,b,c,d}\mathcal{G}^{(0)}_{c,a}(\mathbf{k}, ik_n)\frac{\sigma}{2}W_{a,b}(\mathbf{k},\mathbf{k}+\mathbf{q})\mathcal{G}^{(0)}_{b,d}(\mathbf{k}+\mathbf{q}, ik_n+iq_m)\frac{\sigma}{2}W_{d,c}(\mathbf{k}+\mathbf{q},\mathbf{k}) \tag{81}$$

$$= -\frac{2}{N}\sum_{\mathbf{k}}\left\{D^+_{\mathbf{k},\mathbf{k}+\mathbf{q}}\left[\frac{f(\lambda_{\mathbf{k}+\mathbf{q},1})-f(\lambda_{\mathbf{k},1})}{\lambda_{\mathbf{k}+\mathbf{q},1}-\lambda_{\mathbf{k},1}-iq_m}+\frac{f(\lambda_{\mathbf{k}+\mathbf{q},2})-f(\lambda_{\mathbf{k},2})}{\lambda_{\mathbf{k}+\mathbf{q},2}-\lambda_{\mathbf{k},2}-iq_m}\right]+\right.$$
$$\left. D^-_{\mathbf{k},\mathbf{k}+\mathbf{q}}\left[\frac{f(\lambda_{\mathbf{k}+\mathbf{q},1})-f(\lambda_{\mathbf{k},2})}{\lambda_{\mathbf{k}+\mathbf{q},1}-\lambda_{\mathbf{k},2}-iq_m}+\frac{f(\lambda_{\mathbf{k}+\mathbf{q},1})-f(\lambda_{\mathbf{k},2})}{\lambda_{\mathbf{k}+\mathbf{q},1}-\lambda_{\mathbf{k},2}+iq_m}\right]\right\}, \tag{82}$$

where the form factor $D^\pm_{\mathbf{k},\mathbf{k}+\mathbf{q}}$ are given by

$$D^\pm_{\mathbf{k},\mathbf{k}+\mathbf{q}} = \frac{1}{2}\left(1 \pm \frac{\xi^-_{\mathbf{k}}\xi^-_{\mathbf{k}+\mathbf{q}}+\xi^{12}_{\mathbf{k}}\xi^{12}_{\mathbf{k}+\mathbf{q}}}{\sqrt{(\xi^-_{\mathbf{k}})^2+(\xi^{12}_{\mathbf{k}})^2}\sqrt{(\xi^-_{\mathbf{k}+\mathbf{q}})^2+(\xi^{12}_{\mathbf{k}+\mathbf{q}})^2}}\right). \tag{83}$$

Note that the functional form of Eq.(82) is the same as the orbital nematic case [Eq.(75)], but the sign in front of $\xi^{12}_{\mathbf{k}}\xi^{12}_{\mathbf{k}+\mathbf{q}}$ in Eq.(83) is different from that in Eq.(76). The dynamical longitudinal spin susceptibility is obtained by the analytical continuation $iq_m \to \omega + i0$. In the static limit, $\chi^{zz}(\mathbf{q}, 0)$ is reduced to the static longitudinal spin susceptibility, which we shall use when determing the phase boundary of the SDW phase in Figs.44 and 50.

The transverse spin susceptibility is defined as

$$\chi^\pm(\mathbf{q}, iq_m) = \int_0^\beta d\tau e^{iq_m\tau}\langle T_\tau S^+(\mathbf{q},\tau)S^-(-\mathbf{q},0)\rangle. \tag{84}$$

In the disordered phase where SU(2) symmetry is preserved, the transverse spin susceptibility is the same as the longitudinal one except for a factor of 2:

$$\chi^\pm(\mathbf{q}, iq_m) = 2\chi^{zz}(\mathbf{q}, iq_m). \tag{85}$$

2.4 Eliashberg theory

To explore a possible superconducting instability from orbital nematic and spin fluctuations, we employ the Eliashberg theory, which is the standard theory of the superconductivity driven by fluctuations. First, we construct the pairing interaction, namely the effective interaction between electrons in the Cooper channel in Section 2.4.1. Next, we consider the self-energy contribution by evaluating the Fock diagram in Section 2.4.2. While the self-energy effect is frequently neglected in the study of superconductivity in FeSCs, it is crucially important to discussing the onset temperature of superconductivity. Finally we obtain the linearized Eliashberg equations, which are the central expressions

of the present thesis. The Eliashberg equations are, however, not easy to solve because of the limitation of computer resources such as memory capacity. Hence recalling that superconductivity is driven mainly by electrons near the Fermi energy, we simplify the Eliashberg equations by focusing on such electrons. This simplification[32, 38] allows us to solve the Eliashberg equations even at low temperature [Section 2.4.4].

2.4.1 Pairing interaction

We consider pairing interactions mediated by orbital nematic and spin fluctuations. In the present two-band model, the Cooper pairing can form, in principle, between different bands. However, we do not consider such a possibility in the present thesis because such a pairing would likely have a finite momentum of the center of mass. Instead we consider possible pairing between electrons in the same band with the opposite direction of spin. Note that this does not necessarily exclude a possible triplet pairing. Although we shall confirm by explicit calculations that a triplet state is not stabilized in our model, we find a triplet pairing as the fourth leading instability in the orbital nematic phase [see Fig.69 (c)].

Our total pairing interaction $\Gamma_{\uparrow\downarrow,ab}(\mathbf{k}, ik_n; \mathbf{k}', ik_{n'})$ is given by

$$\Gamma_{\uparrow\downarrow,ab}(\mathbf{k}, ik_n; \mathbf{k}', ik_{n'}) = \Gamma^{\mathrm{ON}}_{\uparrow\downarrow,ab}(\mathbf{k}, ik_n; \mathbf{k}', ik_{n'}) + \Gamma^{zz}_{\uparrow\downarrow,ab}(\mathbf{k}, ik_n; \mathbf{k}', ik_{n'}) + \Gamma^{\pm}_{\uparrow\downarrow,ab}(\mathbf{k}, ik_n; \mathbf{k}', ik_{n'}), \tag{86}$$

where $\Gamma^{\mathrm{ON}}_{\uparrow\downarrow,ab}(\mathbf{k}, ik_n; \mathbf{k}', ik_{n'})$ comes from orbital nematic fluctuations, and $\Gamma^{zz}_{\uparrow\downarrow,ab}(\mathbf{k}, ik_n; \mathbf{k}', ik_{n'})$ and $\Gamma^{\pm}_{\uparrow\downarrow,ab}(\mathbf{k}, ik_n; \mathbf{k}', ik_{n'})$ are due to longitudinal and transverse spin fluctuations, respectively. We derive those pairing interactions one by one.

Orbital nematic interaction

First we consider the pairing interaction from orbital nematic fluctuations $\Gamma^{\mathrm{ON}}_{\uparrow\downarrow}(\mathbf{k}, ik_n; \mathbf{k}', ik_{n'})$, which is described in Fig.17 diagrammaticaly. This figure contains the double wavy line, which is the propagator of orbital nematic fluctuations, $\tilde{g}(\mathbf{k}-\mathbf{k}', ik_n - ik_{n'})$. In the RPA it is given by a series of simple bubbles as shown in Fig.18. Hence its calculation is very similar to the calculation of the orbital nematic susceptibility [see Section 2.3.1].

$$\begin{aligned}
\tilde{g}(\mathbf{k}-\mathbf{k}', ik_n - ik_{n'}) &= g + g[-\chi^{\mathrm{ON}}_0(\mathbf{k}-\mathbf{k}', ik_n - ik_{n'})]g + \\
&\quad g[-\chi^{\mathrm{ON}}_0(\mathbf{k}-\mathbf{k}', ik_n - ik_{n'})]g[-\chi^{\mathrm{ON}}_0(\mathbf{k}-\mathbf{k}', ik_n - ik_{n'})]g + \cdots, && (87)\\
&= g\{1 + [-g\chi^{\mathrm{ON}}_0(\mathbf{k}-\mathbf{k}', ik_n - ik_{n'})] + [-g\chi^{\mathrm{ON}}_0(\mathbf{k}-\mathbf{k}', ik_n - ik_{n'})]^2 + \cdots\}, && (88)\\
&= \frac{g}{1 + g\chi^{\mathrm{ON}}_0(\mathbf{k}-\mathbf{k}', ik_n - ik_{n'})}, && (89)\\
&= g - \frac{g^2\chi^{\mathrm{ON}}_0(\mathbf{k}-\mathbf{k}', ik_n - ik_{n'})}{1 + g\chi^{\mathrm{ON}}_0(\mathbf{k}-\mathbf{k}', ik_n - ik_{n'})}, && (90)\\
&= \tilde{g}_{\mathrm{Ins}} + \tilde{g}_{\mathrm{Ret}}(\mathbf{k}-\mathbf{k}', ik_n - ik_{n'}). && (91)
\end{aligned}$$

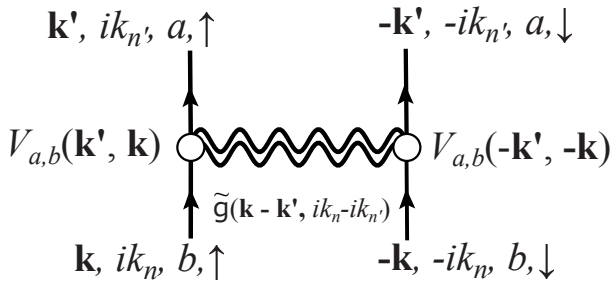

Figure 17: Diagrammatic representation of the pairing interaction from orbital nematic fluctuations. The line with an arrow is the bare Green's function of electrons, and the open circle denotes the vertex Eq.(26), and the double wavy line is the propagator of orbital nematic fluctuations $\tilde{g}(\mathbf{k}-\mathbf{k}', ik_n - ik_{n'})$.

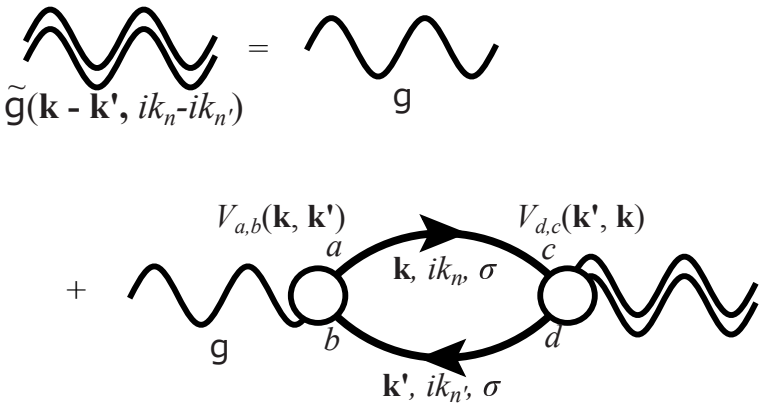

Figure 18: Diagrammatic representation of the pairing interaction due to the orbital nematic interaction in the RPA. The single wavy line is the bare orbital nematic interaction, the line with an arrow is the bare Green's function, and the open circle is the vertex Eq.(26).

Note that we split $\tilde{g}$ into two parts in Eq.(90). One is

$$\tilde{g}_{\rm Ret}(\mathbf{q}, iq_m) = \frac{-g^2\chi_0^{\rm ON}(\mathbf{q}, iq_m)}{1 + g\chi_0^{\rm ON}(\mathbf{q}, iq_m)}, \tag{92}$$

which accounts for the retardation effect. The other part is $\tilde{g}_{\rm Ins} = g$, which is the instantaneous term and does not account for fluctuations. While superconducting instability can occur also from the term $\tilde{g}_{\rm Ins}$, we assume that such an instantaneous effect is cancelled by the Coulomb repulsion that we neglected in our model. For example, we would include an interaction

$$H_1^+ = \frac{g^+}{2}\sum_i n_{i+}n_{i+}, \tag{93}$$

where $n_{i+} = n_{i,1} + n_{i,2}$. Recalling the orbital nematic interaction is given by its odd part [see Eq.(19)], it is natural to assume the presence of its even part of interactions. The sign of g^+ would be positive due to the Coulomb repulsion, which cancel the effect of the superconducting instability due to $\tilde{g}_{\rm Ins}$. Needless to say, the interaction term H_1^+ yields additional fluctuations, which, however, may not be enhanced near the orbital nematic phase nor near the SDW phase. Therefore we do not consider fluctuation effects due to Eq.(93). Instead we focus on the effect of $\tilde{g}_{\rm Ret}$ on the superconducting instability and put hereafter

$$\tilde{g}_{\rm Ins} = 0, \tag{94}$$

and thus

$$\tilde{g} = \tilde{g}_{\rm Ret}. \tag{95}$$

Going back to Fig.17, we then obtain the pairing interaction from orbital nematic fluctuations as

$$\Gamma^{ON}_{\uparrow\downarrow,ab}(\mathbf{k}, ik_n; \mathbf{k}', ik_{n'}) = V^2_{a,b}(\mathbf{k}, \mathbf{k}')\tilde{g}_{\rm Ret}(\mathbf{k}-\mathbf{k}'; ik_n - ik_{n'}). \tag{96}$$

Longitudinal spin interaction

Similarly the pairing interaction from the longitudinal spin fluctuations is given by Fig.19. The double spring $\tilde{J}^z(\mathbf{k}-\mathbf{k}', ik_n - ik_{n'})$ is the propagator of the longitudinal spin fluctuations, which we calculate in the RPA as shown in Fig.20:

$$\begin{aligned}\tilde{J}^z(\mathbf{k}-\mathbf{k}', ik_n - ik_{n'}) &= J(\mathbf{k}-\mathbf{k}') + J(\mathbf{k}-\mathbf{k}')[-\chi_0^{zz}(\mathbf{k}-\mathbf{k}', ik_n - ik_{n'})]J(\mathbf{k}-\mathbf{k}') \\ &+ J(\mathbf{k}-\mathbf{k}')[-\chi_0^{zz}(\mathbf{k}-\mathbf{k}', ik_n - ik_{n'})]J(\mathbf{k}-\mathbf{k}')[-\chi_0^{zz}(\mathbf{k}-\mathbf{k}', ik_n - ik_{n'})]J(\mathbf{k}-\mathbf{k}') + \cdots,\end{aligned} \tag{97}$$

$$= J(\mathbf{k}-\mathbf{k}')\{1 + [-J(\mathbf{k}-\mathbf{k}')\chi_0^{zz}(\mathbf{k}-\mathbf{k}', ik_n - ik_n')] + [-J(\mathbf{k}-\mathbf{k}')\chi_0^{zz}(\mathbf{k}-\mathbf{k}', ik_n - ik_n')]^2 + \cdots\}, \tag{98}$$

$$= \frac{J(\mathbf{k}-\mathbf{k}')}{1 + J(\mathbf{k}-\mathbf{k}')\chi_0^{zz}(\mathbf{k}-\mathbf{k}', ik_n - ik_{n'})}. \tag{99}$$

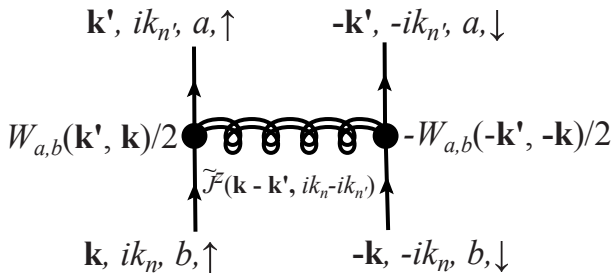

Figure 19: Pairing interaction from the longitudinal spin fluctuations. The line with an arrow is the bare Green's function, and the black filled circle is the vertex Eq.(47), and the double spring is the propagator of the longitudinal spin fluctuations $\tilde{J}^z(\mathbf{k}-\mathbf{k}', ik_n - ik_{n'})$.

This propagator consists of the retarded $\tilde{J}^z_{\rm Ret}(\mathbf{k}-\mathbf{k}', ik_n - ik_{n'})$ and the instantaneous term $\tilde{J}^z_{\rm Ins}(\mathbf{k}-\mathbf{k}')$:

$$\tilde{J}^z(\mathbf{k}-\mathbf{k}, ik_n - ik_{n'}) = \tilde{J}^z_{\rm Ins}(\mathbf{k}-\mathbf{k}') + \tilde{J}^z_{\rm Ret}(\mathbf{k}-\mathbf{k}', ik_n - ik_{n'}) \tag{100}$$

where

$$\tilde{J}^z_{\rm Ins}(\mathbf{k}-\mathbf{k}') = J(\mathbf{k}-\mathbf{k}'), \tag{101}$$

$$\tilde{J}^z_{\rm Ret}(\mathbf{k}-\mathbf{k}', ik_n - ik_{n'}) = -\frac{J^2(\mathbf{k}-\mathbf{k}')\chi_0^{zz}(\mathbf{k}-\mathbf{k}', ik_n - ik_{n'})}{1 + J(\mathbf{k}-\mathbf{k}')\chi_0^{zz}(\mathbf{k}-\mathbf{k}', ik_n - ik_{n'})}. \tag{102}$$

In contrast to the case of the pairing interaction due to the orbital nematic interaction, the instantaneous part $\tilde{J}^z_{\rm Ins}$ can be relevant to superconducting instability and thus we keep it in the present theory. It is insightful to distinguish the effect of the instantaneous interaction from the retardation effect and to clarify each effect on superconductivity. Therefore, we write our pairing interaction due to longitudinal spin interactions as follows:

$$\Gamma^{zz}_{\uparrow\downarrow,ab}(\mathbf{k}, ik_n; \mathbf{k}', ik_{n'}) = -\frac{1}{4}W^2_{a,b}(\mathbf{k},\mathbf{k}')[\tilde{J}^z_{\rm Ins}(\mathbf{k}-\mathbf{k}') + \tilde{J}^z_{\rm Ret}(\mathbf{k}-\mathbf{k}', ik_n - ik_{n'})]. \tag{103}$$

Spin transverse interactions

The spin interaction also contain the transverse component. In the RPA, the pairing interaction from the transverse spin fluctuations is described by as a series of ladder diagrams, which is shown up to the third order in Fig.21. The dotted lines in Fig.21 is bare transverse interaction shown in Fig.22, where we include the vertex $W_{a,b}(\mathbf{k},\mathbf{k}')$ [Eq.(47)] in the bare transverse interaction. Moreover, a single ladder diagram is twice as large as a single bubble in the normal phase, where spin rotational symmetry is preserved. Hence we can write the pairing interaction from transverse spin fluctuations by using χ_0^{zz}.

As we show in Eqs.(50)-(53), we have $W_{a,b}(\mathbf{k},-\mathbf{k}')W_{a,b}(-\mathbf{k},\mathbf{k}') = [W_{a,b}(\mathbf{k},\mathbf{k}')]^2$. Hence the first term in Fig.21 is given by

$$-\frac{1}{2}J(\mathbf{k}+\mathbf{k}')[W_{a,b}(\mathbf{k},\mathbf{k}')]^2. \tag{104}$$

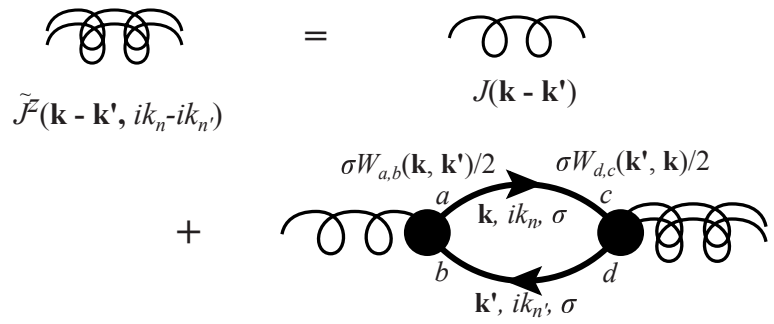

Figure 20: Diagrammatic representation of longitudinal spin fluctuations (double wavy line) in the RPA. The line with an arrow is the bare Green's function, and the black filled circle is the vertex Eq.(47) multiplied by spin σ, and the single spring is the bare spin interaction $J(\mathbf{q})$.

The second term then becomes

$$\sum_{\mathbf{k}_1,n_1,a_1,b_1}\left[-\frac{1}{2}J(-\mathbf{k}'-\mathbf{k})\right]^2[W_{a,b}(\mathbf{k},\mathbf{k}')]^2$$
$$\times\left\{[W_{a_1,b_1}(\mathbf{k}_1,-\mathbf{k}'+\mathbf{k}_1-\mathbf{k})]^2\left[-\frac{1}{\beta N}\mathcal{G}^{(0)}_{a_1}(\mathbf{k}_1,ik_{n_1})\mathcal{G}^{(0)}_{b_1}(-\mathbf{k}'+\mathbf{k}_1-\mathbf{k},-ik_{n'}+ik_{n_1}-ik_n)\right]\right\}. \tag{105}$$

Recalling Eq.(81), we see that the second term [Eq.(105)] is written by using χ_0^{zz}:

$$\left[\frac{1}{2}J(\mathbf{k}+\mathbf{k}')\right]^2[W_{a,b}(\mathbf{k},\mathbf{k}')]^2\cdot 2\chi_0^{zz}(\mathbf{k}+\mathbf{k}',ik_n+ik_{n'}). \tag{106}$$

Similarly, the third term is

$$\left[-\frac{1}{2}J(\mathbf{k}+\mathbf{k}')\right]^3$$
$$\times\left\{\left(-\frac{1}{\beta N}\right)\sum_{a_1,b_1,\mathbf{k}_1,n_1}[W_{b_1,a_1}(\mathbf{k}_1-\mathbf{k}'-\mathbf{k},\mathbf{k}_1)]^2\,\mathcal{G}^{(0)}_{a_1}(\mathbf{k}_1,ik_{n_1})\mathcal{G}^{(0)}_{b_1}(\mathbf{k}_1-\mathbf{k}'-\mathbf{k},ik_{n_1}-ik_{n'}-ik_n)\right.$$
$$\left.\times\left(-\frac{1}{\beta N}\right)\sum_{a_2,b_2,\mathbf{k}_2,n_2}[W_{b_2,a_2}(\mathbf{k}_2-\mathbf{k}'-\mathbf{k},\mathbf{k}_2)]^2\,\mathcal{G}^{(0)}_{a_2}(\mathbf{k}_2,ik_{n_2})\mathcal{G}^{(0)}_{b_2}(\mathbf{k}_2-\mathbf{k}'-\mathbf{k},ik_{n_2}-ik_{n'}-ik_n)\right\}, \tag{107}$$

$$=\left[-\frac{1}{2}J(\mathbf{k}+\mathbf{k}')\right]^3[2\chi_0^{zz}(\mathbf{k}+\mathbf{k}',ik_n+ik_{n'})]^2. \tag{108}$$

Hence taking the sum of the ladder diagrams (Fig.21), we obtain the pairing interaction

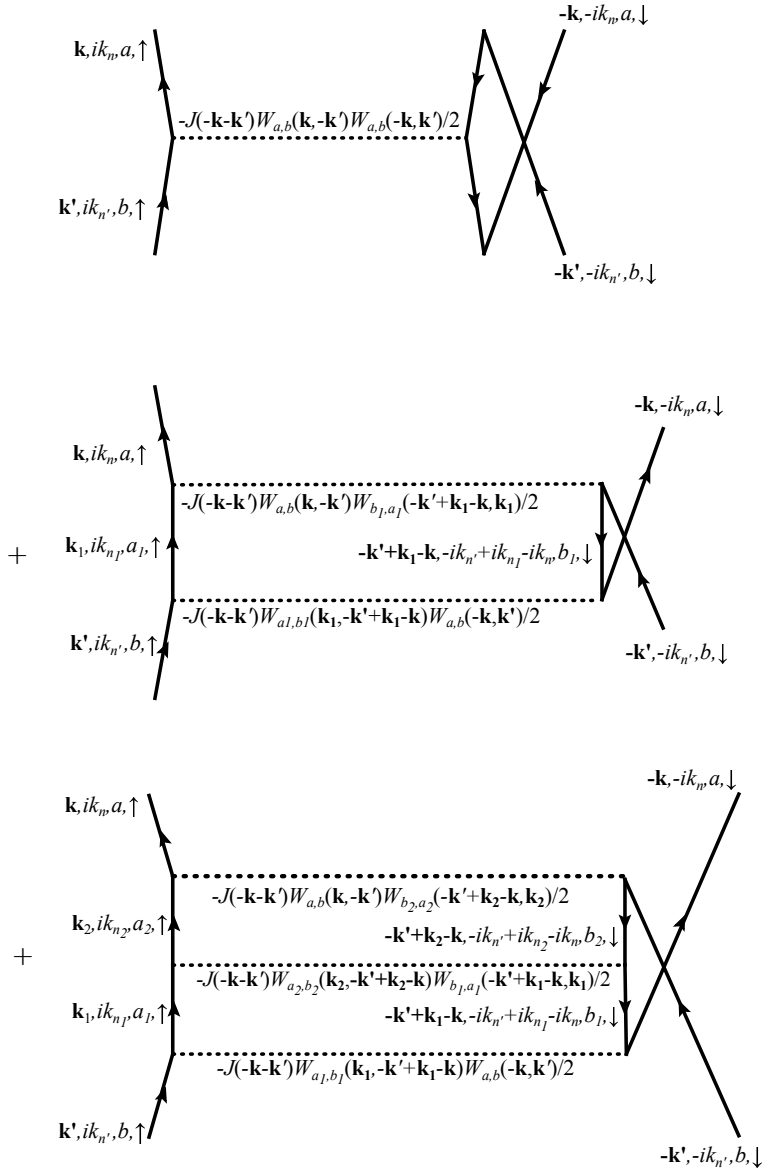

Figure 21: Diagrammatic representatiton of the pairing interaction from transverse spin fluctuations up to the third order. The line with an arrow is the bare Green's function, and the dotted line bare transverse spin interaction $-J(\mathbf{q})W_{a,b}(\mathbf{k},\mathbf{k}+\mathbf{q})W_{c,d}(\mathbf{k}'+\mathbf{q},\mathbf{k}')/2$

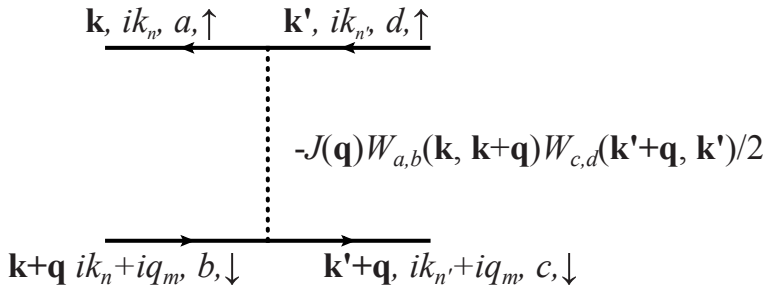

Figure 22: Diagram of the transverse component of the spin interaction (dotted line). The line with an arrow is the bare Green's function of electrons.

from the transverse spin interaction as follows:

$$\Gamma^{\pm}_{\uparrow\downarrow,ab}(\mathbf{k}, ik_n; \mathbf{k}', ik_{n'}) = -\frac{1}{2}J(\mathbf{k}+\mathbf{k}')[W_{a,b}(\mathbf{k}, \mathbf{k}')]^2 \times \left\{1 + \left[-\frac{1}{2}J(\mathbf{k}+\mathbf{k}')2\chi_0^{zz}(\mathbf{k}+\mathbf{k}', ik_n + ik_{n'})\right] + \left[-\frac{1}{2}J(\mathbf{k}+\mathbf{k}')2\chi_0^{zz}(\mathbf{k}+\mathbf{k}', ik_n + ik_{n'})\right]^2 + \cdots\right\}, \quad (109)$$

$$= -\frac{1}{2}J(\mathbf{k}+\mathbf{k}')[W_{a,b}(\mathbf{k}, \mathbf{k}')]^2\left\{1 + [-J(\mathbf{k}+\mathbf{k}')\chi_0^{zz}(\mathbf{k}+\mathbf{k}', ik_n + ik_{n'})] + [-J(\mathbf{k}+\mathbf{k}')\chi_0^{zz}(\mathbf{k}+\mathbf{k}', ik_n + ik_{n'})]^2 + \cdots\right\}, \quad (110)$$

$$= -\frac{1}{2}J(\mathbf{k}+\mathbf{k}')[W_{a,b}(\mathbf{k}, \mathbf{k}')]^2\frac{1}{1 + J(\mathbf{k}+\mathbf{k}')\chi_0^{zz}(\mathbf{k}+\mathbf{k}', ik_n + ik_{n'})}, \quad (111)$$

$$= -\frac{1}{2}[W_{a,b}(\mathbf{k}, \mathbf{k}')]^2\tilde{J}^z(\mathbf{k}+\mathbf{k}', ik_n + ik_{n'}). \quad (112)$$

Note that the arguments of $\tilde{J}^z$ in Eq.(112) are $\mathbf{k}+\mathbf{k}', ik_n + ik_{n'}$ whereas they are $\mathbf{k}-\mathbf{k}'$ and $ik_n - ik_{n'}$ in the longitudinal spin interaction [Eq.(103)].

2.4.2 Self-energy

The self-energy effect in the Eliashberg theory is frequently neglected and is not much discussed in the context of FeSCs. However, we shall show in Section 3 that the self-energy effect is crucially important to the onset temperature of superconducting instability. In the Eliashberg theory, the self-energy effect is considered in the Fock diagram. There are three contributions:

$$\Sigma_{a,b}(\mathbf{k}, ik_n) = \Sigma^{ON}_{a,b}(\mathbf{k}, ik_n) + \Sigma^{zz}_{a,b}(\mathbf{k}, ik_n) + \Sigma^{\pm}_{a,b}(\mathbf{k}, ik_n), \quad (113)$$

where $\Sigma^{\rm ON}_{a,b}(\mathbf{k}, ik_n)$ is from the orbital nematic interaction [Eq.(32)], whereas $\Sigma^{zz}_{a,b}(\mathbf{k}, ik_n)$ and $\Sigma^{\pm}_{a,b}(\mathbf{k}, ik_n)$ are due to the longitudinal [Eq.(48)] and transverse [Eq.(49)] spin interaction, respectively.

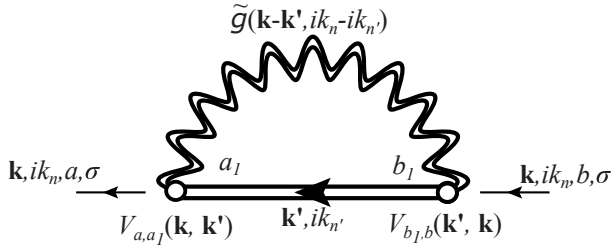

Figure 23: Self-energy diagram from the orbital nematic fluctuations (the double wavy line). The double line with an arrow is the full Green's function, whereas the open circles are the vertex Eq.(26).

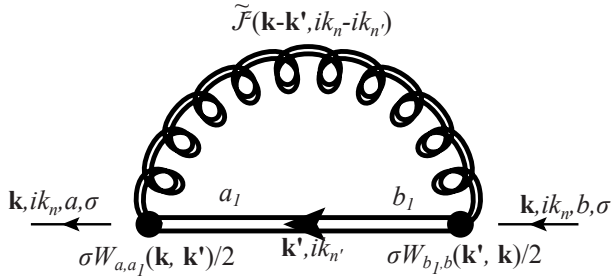

Figure 24: Fock diagram due to the longitudinal spin interaction (double spring line). The open circles are the vertex Eq.(47) and the double line with an arrow is the full Green's function of electrons.

We first evaluate $\Sigma^{\rm ON}_{a,b}(\mathbf{k}, ik_n)$, which is given by the diagram shown in Fig.23. Note that the Green's function of electrons is described in Fig.23 by a double line, namely a renormalized Green's function so that the self-energy effect is considered self-consistently. In this diagram, the double wavy line and the two open circles are the same as those of the pairing interaction in Fig.17 , but the arguments and band indices of V are different. The Fock diagram is written as

$$\Sigma^{\rm ON}_{a,b}(\mathbf{k}, ik_n) = -\frac{1}{\beta N}\sum_{a_1,b_1}\sum_{\mathbf{k}',n'}\tilde{g}(\mathbf{k}-\mathbf{k}', ik_n - ik_{n'}) \times V_{a,a_1}(\mathbf{k},\mathbf{k}')\mathcal{G}_{a_1,b_1}(\mathbf{k}', ik_{n'})V_{b_1,b}(\mathbf{k}',\mathbf{k}), \quad (114)$$

where $\mathcal{G}_{a_1,b_1}(\mathbf{k}', ik_{n'})$ is the full Green's function of electrons.

Figure 24 is the self-energy due to the longitudinal spin interaction $\Sigma^{zz}_{a,b}(\mathbf{k}, ik_n)$, which is a diagram similar to Fig.23. The vertex $\frac{\sigma}{2}W_{a,b}(\mathbf{k},\mathbf{k}')$ comes from Eq.(48) [see also Fig.15] and the longitudinal spin interaction $\tilde{J}^z$ is already computed in Eq.(99). Hence the Fock diagram Fig.24 is evaluated as

$$\Sigma^{zz}_{a,b}(k) = -\frac{1}{\beta N}\sum_{a_1,b_1}\sum_{\mathbf{k}',n'}\frac{1}{4}\tilde{J}^z(\mathbf{k}-\mathbf{k}', ik_n - ik_{n'})W_{a,a_1}(\mathbf{k},\mathbf{k}')\mathcal{G}_{a_1,b_1}(\mathbf{k}', ik_{n'})W_{b_1,b}(\mathbf{k}',\mathbf{k}). \quad (115)$$

Note again that the full Green's function $\mathcal{G}_{a_1,b_1}(\mathbf{k}', ik_{n'})$ enters Eq.(115).

We next consider the self-energy due to the transverse spin interaction [Eq.(49)]. While symbolically it is described as the same diagram as Figs.23 and 24, we present more details in Fig.25. The first term in Fig.25 is calculated as below:

$$\frac{1}{\beta N}\sum_{\mathbf{k}',n'}\sum_{a_1,b_1}\left[-\frac{1}{2}J(\mathbf{k}-\mathbf{k}')\right]^2 W_{b_1,b}(\mathbf{k}',\mathbf{k})W_{a,a_1}(\mathbf{k},\mathbf{k}') \times\left(-\frac{1}{\beta N}\right)\sum_{c_1,c}\sum_{\mathbf{k}_1,n_1}[W_{c,c_1}(\mathbf{k}_1,\mathbf{k}_1-\mathbf{k}+\mathbf{k}')]^2 \times\mathcal{G}^{(0)}_{c}(\mathbf{k}_1,ik_{n_1})\mathcal{G}^{(0)}_{c_1}(\mathbf{k}_1-\mathbf{k}+\mathbf{k}',ik_{n_1}-ik_n+ik_{n'})\mathcal{G}_{a_1,b_1}(\mathbf{k}',ik_{n'}), \quad (116)$$

$$=\frac{1}{\beta N}\sum_{\mathbf{k}',n',a_1,b_1}\left[-\frac{1}{2}J(\mathbf{k}-\mathbf{k}')\right]^2 W_{a,a_1}(\mathbf{k},\mathbf{k}')\mathcal{G}_{a_1,b_1}(\mathbf{k}',ik_{n'})W_{b_1,b}(\mathbf{k}',\mathbf{k})[2\chi_0^{zz}(\mathbf{k}-\mathbf{k}',ik_n-ik_{n'})]. \quad (117)$$

Similarly the second term is calculated as

$$\frac{1}{\beta N}\sum_{a_1,b_1,\mathbf{k}',n'}\left[-\frac{1}{2}J(\mathbf{k}-\mathbf{k}')\right]^3 \times\left(-\frac{1}{\beta N}\right)\sum_{c_1,d_1,\mathbf{k}_1,n_1}[W_{c_1,d_1}(\mathbf{k}_1+\mathbf{k}'-\mathbf{k},\mathbf{k}_1)]^2\mathcal{G}^{(0)}_{c_1}(\mathbf{k}_1+\mathbf{k}'-\mathbf{k},ik_{n_1}+ik_{n'}-ik_n)\mathcal{G}^{(0)}_{d_1}(\mathbf{k}_1,ik_{n_1}) \times\left(-\frac{1}{\beta N}\right)\sum_{c_2,d_2,\mathbf{k}_2,n_2}[W_{c_2,d_2}(\mathbf{k}_2+\mathbf{k}'-\mathbf{k},\mathbf{k}_2)]^2\mathcal{G}^{(0)}_{c_2}(\mathbf{k}_2+\mathbf{k}'-\mathbf{k},ik_{n_2}+ik_{n'}-ik_n)\mathcal{G}^{(0)}_{d_2}(\mathbf{k}_2,ik_{n_2}) \times W_{b_1,b}(\mathbf{k}',\mathbf{k})W_{a,a_1}(\mathbf{k},\mathbf{k}')\mathcal{G}_{a_1,b_1}(\mathbf{k}',ik_{n'}), \quad (118)$$

$$=\frac{1}{\beta N}\sum_{a_1,b_1,\mathbf{k}',n'}\left[-\frac{1}{2}J(\mathbf{k}-\mathbf{k}')\right]^3 W_{a,a_1}(\mathbf{k},\mathbf{k}')W_{b_1,b}(\mathbf{k}',\mathbf{k})\mathcal{G}_{a_1,b_1}(\mathbf{k}',ik_{n'})[2\chi_0^{zz}(\mathbf{k}-\mathbf{k}',ik_n-ik_{n'})]^2. \quad (119)$$

The third term becomes

$$-\frac{1}{\beta N}\sum_{a_1,b_1,\mathbf{k}',n'}\left[-\frac{1}{2}J(\mathbf{k}-\mathbf{k}')\right]^4 \times\left(-\frac{1}{\beta N}\right)\sum_{c_1,d_1,\mathbf{k}_1,n_1}[W_{c_1,d_1}(\mathbf{k}_1+\mathbf{k}'-\mathbf{k},\mathbf{k}_1)]^2\mathcal{G}^{(0)}_{c_1}(\mathbf{k}_1+\mathbf{k}'-\mathbf{k},ik_{n_1}+ik_{n'}-ik_n)\mathcal{G}^{(0)}_{d_1}(\mathbf{k}_1,ik_{n_1}) \times\left(-\frac{1}{\beta N}\right)\sum_{c_2,d_2,\mathbf{k}_2,n_2}[W_{c_2,d_2}(\mathbf{k}_2+\mathbf{k}'-\mathbf{k},\mathbf{k}_2)]^2\mathcal{G}^{(0)}_{c_2}(\mathbf{k}_2+\mathbf{k}'-\mathbf{k},ik_{n_2}+ik_{n'}-ik_n)\mathcal{G}^{(0)}_{d_2}(\mathbf{k}_2,ik_{n_2}) \times\left(-\frac{1}{\beta N}\right)\sum_{c_3,d_3,\mathbf{k}_3,n_3}[W_{c_3,d_3}(\mathbf{k}_3+\mathbf{k}'-\mathbf{k},\mathbf{k}_3)]^2\mathcal{G}^{(0)}_{c_3}(\mathbf{k}_3+\mathbf{k}'-\mathbf{k},ik_{n_3}+ik_{n'}-ik_n)\mathcal{G}^{(0)}_{d_3}(\mathbf{k}_3,ik_{n_3}) \times W_{b_1,b}(\mathbf{k}',\mathbf{k})W_{a,a_1}(\mathbf{k},\mathbf{k}')\mathcal{G}_{a_1,b_1}(\mathbf{k}',ik_{n'}), \quad (120)$$

$$=\frac{1}{\beta N}\left[-\frac{1}{2}J(\mathbf{k}-\mathbf{k}')\right]^4 W_{a,a_1}(\mathbf{k},\mathbf{k}')W_{b_1,b}(\mathbf{k}',\mathbf{k})\mathcal{G}_{a_1,b_1}(\mathbf{k}',ik_{n'})[2\chi_0^{zz}(\mathbf{k}-\mathbf{k}',ik_n-ik_{n'})]^3. \quad (121)$$

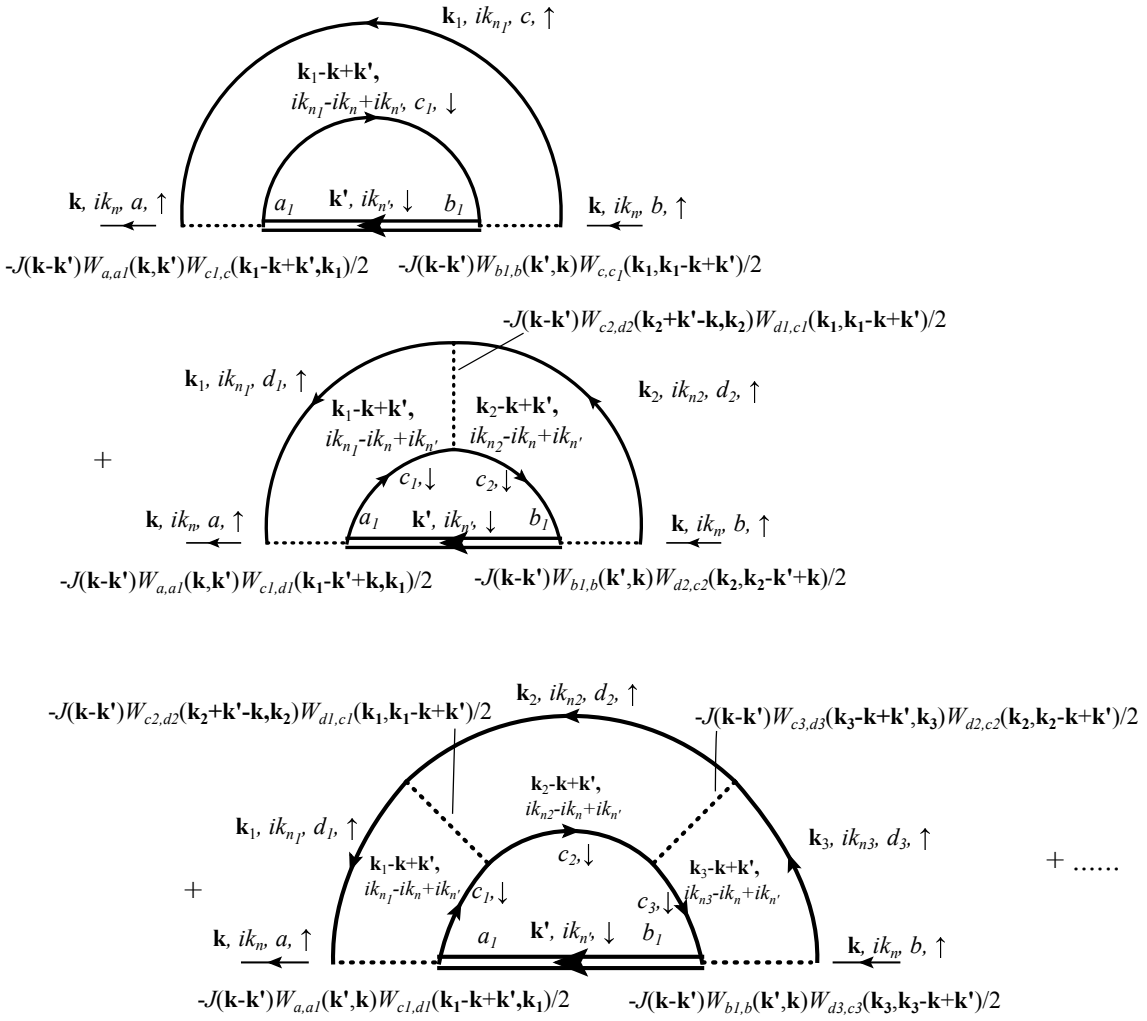

Figure 25: Self-energy due to the transverse spin interaction. The curves with an arrow are the bare Green's functions, and the dotted lines are the bare transverse spin interactions (see Fig.22). The double lines with an arrow are the full Green's functions of electrons.

Summing all the terms, we obtain

$$\Sigma^{\pm}_{a,b}(\mathbf{k}, ik_n) = \frac{1}{\beta N}\sum_{a_1,b_1,\mathbf{k}',n'} W_{a,a_1}(\mathbf{k},\mathbf{k}')\mathcal{G}_{a_1,b_1}(\mathbf{k}', ik_{n'})W_{b_1,b}(\mathbf{k}',\mathbf{k})\left[-\frac{1}{2}J(\mathbf{k}-\mathbf{k}')\right]$$
$$\times\{-J(\mathbf{k}-\mathbf{k}')\chi_0^{zz}(\mathbf{k}-\mathbf{k}', ik_n - ik_{n'}) + \left[-J(\mathbf{k}-\mathbf{k}')\chi_0^{zz}(\mathbf{k}-\mathbf{k}', ik_n - ik_{n'})\right]^2 + \cdots\}, \tag{122}$$

$$= -\frac{1}{2\beta N}\sum_{a_1,b_1,\mathbf{k}',n'} W_{a,a_1}(\mathbf{k},\mathbf{k}')\mathcal{G}_{a_1,b_1}(\mathbf{k}', ik_{n'})W_{b_1,b}(\mathbf{k}',\mathbf{k})$$
$$\times\frac{J^2(\mathbf{k}-\mathbf{k}')\chi_0^{zz}(\mathbf{k}-\mathbf{k}', ik_n - ik_{n'})}{1 + J(\mathbf{k}-\mathbf{k}')\chi_0^{zz}(\mathbf{k}-\mathbf{k}', ik_n - ik_{n'})}, \tag{123}$$

$$= \frac{1}{2\beta N}\sum_{a_1,b_1,\mathbf{k}',n'} W_{a,a_1}(\mathbf{k},\mathbf{k}')\mathcal{G}_{a_1,b_1}(\mathbf{k}', ik_{n'})W_{b_1,b}(\mathbf{k}',\mathbf{k})\tilde{J}^z_{\mathrm{Ret}}(\mathbf{k}-\mathbf{k}', ik_n - ik_{n'}). \tag{124}$$

In contrast to the case of the pairing interaction from the transverse spin fluctuations [Eq.(112)], the momentum and energy transfer of $\tilde{J}^z$ is given by $\mathbf{k}-\mathbf{k}'$ and $ik_n - ik_{n'}$, similar to $\Sigma^{\mathrm{ON}}_{a,b}(\mathbf{k}, ik_n)$ [Eq.(114)] and $\Sigma^{zz}_{a,b}(\mathbf{k}, ik_n)$ [Eq.(115)].

The total self-energy may be written in a compact form

$$\Sigma_{a,b}(\mathbf{k}, ik_n) = \Sigma^{\mathrm{ON}}_{a,b}(\mathbf{k}, ik_n) + \Sigma^{zz}_{a,b}(\mathbf{k}, ik_n) + \Sigma^{\pm}_{a,b}(\mathbf{k}, ik_n) \tag{125}$$

$$= -\frac{1}{\beta N}\sum_{\mathbf{k}',n',a_1,b_1} X^{a_1,b_1}_{a,b}(\mathbf{k}, ik_n;\mathbf{k}', ik_{n'})\mathcal{G}_{a_1,b_1}(\mathbf{k}', ik_{n'}), \tag{126}$$

where

$$X^{a_1,b_1}_{a,b}(\mathbf{k}, ik_n;\mathbf{k}', ik_{n'}) = \Big\{\tilde{g}(\mathbf{k}-\mathbf{k}', ik_n - ik_{n'})V_{a,a_1}(\mathbf{k},\mathbf{k}')V_{b_1,b}(\mathbf{k}',\mathbf{k}) +$$
$$\frac{1}{4}[3\tilde{J}^z_{\mathrm{Ret}}(\mathbf{k}-\mathbf{k}', ik_n - ik_{n'}) + \tilde{J}^z_{\mathrm{Ins}}(\mathbf{k}-\mathbf{k}')]W_{a,a_1}(\mathbf{k},\mathbf{k}')W_{b_1,b}(\mathbf{k}',\mathbf{k})\Big\}. \tag{127}$$

Although $\Sigma^{\pm}_{a,b}$ consists of the retarded term from the spin fluctuations [Eq.(124)], $\Sigma^{zz}_{a,b}$ contains from both the retarded and instantaneous term from the spin fluctuations [Eq.(115)]. This is the reason why the prefactors of $\tilde{J}^z_{\mathrm{Ins}}$ and $\tilde{J}^z_{\mathrm{Ret}}$ in Eq.(127) are different.

On the other hand, the self-energy is determined by the Dyson equation

$$\mathcal{G}_{a,b}{}^{-1}(\mathbf{k}, ik_n) = \mathcal{G}^{(0)}_{a,b}{}^{-1}(\mathbf{k}, ik_n) - \Sigma_{a,b}(\mathbf{k}, ik_n). \tag{128}$$

Since the full Green's function $\mathcal{G}_{a,b}(\mathbf{k}, ik_n)$ is included also in $\Sigma_{a,b}(\mathbf{k}, ik_n)$, Eq.(128) is the self-consistency equation for the self-energy $\Sigma_{a,b}(\mathbf{k}, ik_n)$. In the Eliashberg theory, we consider the effect of renormalization of quasi-particle weight as a major self-energy effect. In addition, we assume that the major contribution to $\Sigma_{a,b}(\mathbf{k}, ik_n)$ comes from the intraband component and neglect the interband contribution. Therefore our self-energy is appoximated as

$$\Sigma_{a,b}(\mathbf{k}, ik_n) \simeq [1 - Z_a(\mathbf{k}, ik_n)]ik_n\delta_{a,b} \tag{129}$$

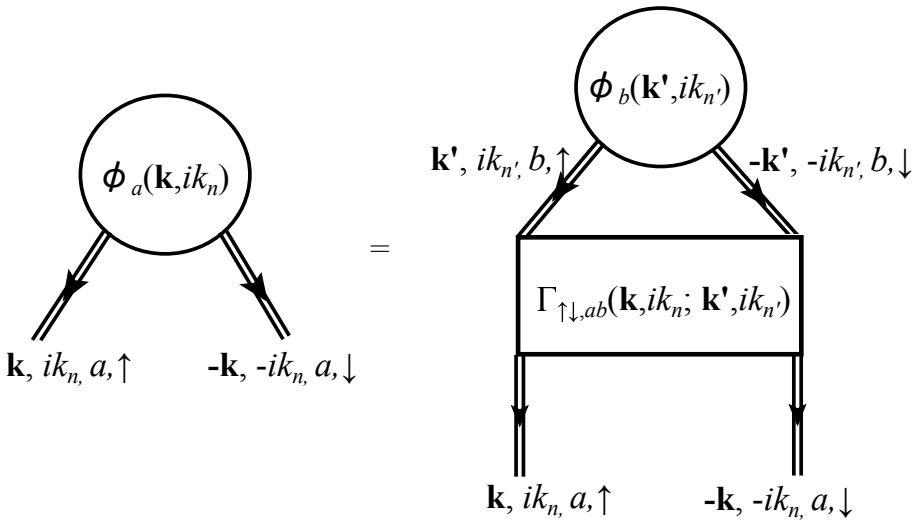

Figure 26: Diagrammatic representation of the linearized gap equation. The circle is the pairing gap function and the box is the pairing interaction; the arrowed double line is the full Green's function.

in the Eliashberg theory. The Dyson's equation [Eq.(128)] and the bare Green's function [Eq.(69)] imply that the full Green's function becomes

$$\mathcal{G}_{a,b}(\mathbf{k}, ik_n) = \begin{pmatrix} \dfrac{1}{ik_n Z_1(\mathbf{k}, ik_n) - \lambda_{\mathbf{k},1}} & 0 \\ 0 & \dfrac{1}{ik_n Z_2(\mathbf{k}, ik_n) - \lambda_{\mathbf{k},2}} \end{pmatrix}_{a,b}. \tag{130}$$

Therefore the self-energy Eq.(126) becomes

$$\Sigma_{a,b}(\mathbf{k}, ik_n) \simeq \frac{1}{\beta N} \sum_{\mathbf{k}', n', c} X^{c,c}_{a,b}(\mathbf{k}, ik_n; \mathbf{k}', ik_{n'}) \frac{ik_{n'} Z_c(\mathbf{k}', ik_{n'}) + \lambda_{\mathbf{k}',c}}{\left[k_{n'} Z_c(\mathbf{k}', ik_{n'})\right]^2 + \left(\lambda_{\mathbf{k}',c}\right)^2} \tag{131}$$

Comparing Eq.(131) with Eq.(129), we obtain the self-consistency equation of $Z_a(\mathbf{k}, ik_n)$

$$[1 - Z_a(\mathbf{k}, ik_n)] ik_n = \frac{1}{\beta N} \sum_{\mathbf{k}', ik_{n'}, c} X^{c,c}_{a,a}(\mathbf{k}, ik_n; \mathbf{k}', ik_{n'}) \frac{ik_n Z_c(\mathbf{k}', ik_{n'})}{\left[k_{n'} Z_c(\mathbf{k}', ik_{n'})\right]^2 + (\lambda_{\mathbf{k}',c})^2}. \tag{132}$$

This equation is the self-energy part of the Eliashberg theory. In addition, it follows that

$$Z_a(\mathbf{k}, ik_n) = Z_a(-\mathbf{k}, ik_n), \tag{133}$$

because

$$X^{cc}_{a,b}(\mathbf{k}, ik_n; \mathbf{k}', ik_{n'}) = X^{cc}_{a,b}(-\mathbf{k}, ik_n; -\mathbf{k}', ik_{n'}). \tag{134}$$

2.4.3 Linearized Eliashberg equation

Since we are interested in the onset temperature of superconducting instability as well as the momentum dependence of the pairing gap, we study the linearized gap equation. The

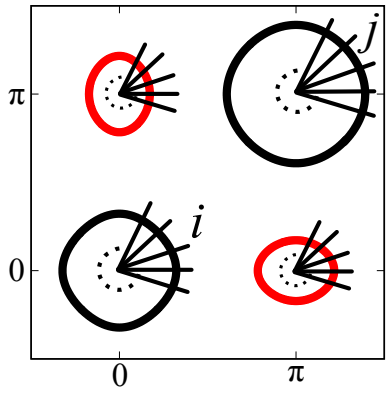

Figure 27: Fermi surfaces in the first quadrant of the first Brillouin zone. Each Fermi pocket is divided into small segments to include the momentum dependence of $\Delta_a(\mathbf{k}, ik_n)$ and $Z_a(\mathbf{k}, ik_n)$.

gap equation is described in Fig.26 graphically, which implies

$$\phi_a(\mathbf{k}, ik_n) = -\frac{1}{\beta N}\sum_{b,\mathbf{k}',n'} \Gamma_{\uparrow\downarrow,ab}(\mathbf{k}, ik_n; \mathbf{k}', ik_{n'})\mathcal{G}_b(\mathbf{k}', ik_{n'})\mathcal{G}_b(-\mathbf{k}', -ik_{n'})\phi_b(\mathbf{k}', ik_{n'}). \quad (135)$$

Here we give a single a or b as an index of $\mathcal{G}$ because it is diagonal [see Eq.(130)]. The gap $\phi_a(\mathbf{k}, ik_n)$ in Eq.(135) is connected with the physical gap function $\Delta_a(\mathbf{k}, ik_n)$ via the renormalization function $Z_a(\mathbf{k}, ik_n)$

$$\phi_a(\mathbf{k}, ik_n) = Z_a(\mathbf{k}, ik_n)\Delta_a(\mathbf{k}, ik_n). \quad (136)$$

Using Eq.(130), we obtain the linearized gap equation

$$\Delta_a(\mathbf{k}, ik_n) = -\frac{1}{\beta N Z_a(\mathbf{k}, ik_n)}\sum_{b,\mathbf{k}',n'} \frac{\Gamma_{\uparrow\downarrow,ab}(\mathbf{k}, ik_n; \mathbf{k}, ik_n')}{\left[k_{n'}Z_b(\mathbf{k}', ik_{n'})\right]^2 + \left(\lambda_{\mathbf{k}',b}\right)^2} Z_b(\mathbf{k}', ik_{n'})\Delta_b(\mathbf{k}', ik_{n'}). \quad (137)$$

2.4.4 Simplification of Eliashberg equations

Equations (132) and (137) are called as the coupled Eliashberg equations. Solving these equations is, however, very demanding in general. In particular, we aim to determine not only the momentum dependence of the pairing gap but also the onset temperature of superconductivity, which is expected to occur at temperature much lower than t. To achieve our aim, we make the following simplifications of the Eliashberg equations.

Since superconductivity is a phenomenon near the Fermi surface, we project the pairing interaction Γ and the renormalization function Z on each Fermi pocket. This idea itself was employed already in Ref.[32]. We extend such a formalism by including the momentum dependence of both pairing gap and renormalization function. That is, we divide each Fermi pocket to small segments as illustrated in Fig.27. Although we show the

Fermi surface in the first quadrand of the first Brillouin zone ($0 \leq k_x, k_y \leq \pi$) in Fig.27, our calculations are done in the whole of the first Brillouin zone ($-\pi \leq k_x, k_y \leq \pi$). We denote each Fermi-surface segment in terms of i, which carries information of the momentum $\mathbf{k}$ and the band index a, namely,

$$Z_a(\mathbf{k}, ik_n) \to Z_i(ik_n) \tag{138}$$

$$\Delta_a(\mathbf{k}, ik_n) \to \Delta_i(ik_n). \tag{139}$$

The pairing interactions occurs between electrons on the Fermi-surface segments i and j. Hence we averaged out the pairing interaction Eqs.(96), (103), (112), respectively,

$$\Gamma^{ON}_{i,j}(ik_n, ik_{n'}) = \langle \Gamma^{\rm ON}_{\uparrow\downarrow,ab}(\mathbf{k}, ik_n; \mathbf{k}', ik_{n'})\rangle \tag{140}$$

$$= \frac{\frac{1}{N}\sum_{\mathbf{k}\in {\rm FS}_i}\frac{1}{N}\sum_{\mathbf{k}'\in {\rm FS}_j}[V_{i,j}(\mathbf{k},\mathbf{k}')]^2\tilde{g}(\mathbf{k}-\mathbf{k}', ik_n - ik_{n'})}{\frac{1}{N}\sum_{\mathbf{k}\in {\rm FS}_i}\frac{1}{N}\sum_{\mathbf{k}'\in {\rm FS}_j}}, \tag{141}$$

$$\Gamma^{zz}_{i,j}(ik_n, ik_{n'}) = \langle \Gamma^{zz}_{\uparrow\downarrow,ab}(\mathbf{k}, ik_n; \mathbf{k}', ik_{n'})\rangle \tag{142}$$

$$= -\frac{1}{4}\frac{\frac{1}{N}\sum_{\mathbf{k}\in {\rm FS}_i}\frac{1}{N}\sum_{\mathbf{k}'\in {\rm FS}_j}[W_{i,j}(\mathbf{k},\mathbf{k}']^2\tilde{J}^z(\mathbf{k}-\mathbf{k}', ik_n - ik_{n'})}{\frac{1}{N}\sum_{\mathbf{k}\in {\rm FS}_i}\frac{1}{N}\sum_{\mathbf{k}'\in {\rm FS}_j}}, \tag{143}$$

$$\Gamma^{\pm}_{i,j}(ik_n, ik_{n'}) = \langle \Gamma^{\pm}_{\uparrow\downarrow,ab}(\mathbf{k}, ik_n; \mathbf{k}', ik_{n'})\rangle \tag{144}$$

$$= -\frac{1}{2}\frac{\frac{1}{N}\sum_{\mathbf{k}\in {\rm FS}_i}\frac{1}{N}\sum_{\mathbf{k}'\in {\rm FS}_j}[W_{i,j}(\mathbf{k},\mathbf{k}')]^2[\tilde{J}^z(\mathbf{k}+\mathbf{k}', ik_n + ik_{n'})]}{\frac{1}{N}\sum_{\mathbf{k}\in {\rm FS}_i}\frac{1}{N}\sum_{\mathbf{k}'\in {\rm FS}_j}}. \tag{145}$$

$$\tag{146}$$

Here $\sum_{\mathbf{k}\in FS_i}$ is a summation with respect to $\mathbf{k}$ on each Fermi-surface segment i. Note that the vertices $V_{a,b}(\mathbf{k},\mathbf{k}')$ and $W_{a,b}(\mathbf{k},\mathbf{k}')$ are written in the above expressions as $V_{i,j}(\mathbf{k},\mathbf{k}')$ and $W_{i,j}(\mathbf{k},\mathbf{k}')$, respectively. Similarly

$$X_{i,j}(ik_n, ik_{n'}) = \langle X^{b,b}_{a,a}(\mathbf{k}, ik_n; \mathbf{k}', ik_{n'})\rangle$$

$$= \frac{1}{\frac{1}{N}\sum_{\mathbf{k}\in {\rm FS}_i}\frac{1}{N}\sum_{\mathbf{k}'\in {\rm FS}_j}}\frac{1}{N}\sum_{\mathbf{k}\in {\rm FS}_i}\frac{1}{N}\sum_{\mathbf{k}'\in {\rm FS}_j}\Big\{\tilde{g}(\mathbf{k}-\mathbf{k}', ik_n - ik_{n'})[V_{i,j}(\mathbf{k},\mathbf{k}')]^2$$

$$+\frac{1}{4}[3\tilde{J}^z_{\rm Ret}(\mathbf{k}-\mathbf{k}', ik_n - ik_{n'}) + \tilde{J}^z_{\rm Ins}(\mathbf{k}-\mathbf{k}')][W_{i,j}(\mathbf{k},\mathbf{k}')]^2\Big\}. \tag{147}$$

The momentum dependence perpendicular the Fermi surface in the band $\lambda_{\mathbf{k},a}$ is considered by replacing it with the density of state:

$$\frac{1}{N}\sum_{\mathbf{k}\in {\rm FS}_i}\frac{1}{A^2 + (\lambda_{\mathbf{k},i})^2} = \int_{-\Lambda}^{\Lambda} d\varepsilon \frac{1}{N}\sum_{\mathbf{k}\in {\rm FS}_i}\delta(\varepsilon - \lambda_{\mathbf{k},i})\frac{1}{A^2+\varepsilon^2} \tag{148}$$

$$= \int_{-\Lambda}^{\Lambda} d\varepsilon N_i(\varepsilon)\frac{1}{A^2+\varepsilon^2}. \tag{149}$$

Here Λ is a cutoff and $N_i(\varepsilon)$ is the density of states on the Fermi-surface segment i. Assuming that the density of states is approximated by its value as at the Fermi energy

$N_i(0)$, we can evaluate Eq.(149):

$$\frac{1}{N}\sum_{\mathbf{k}\in \mathrm{FS}_i}\frac{1}{A^2+(\lambda_{\mathbf{k},i})^2} \simeq N_i(0)\int_{-\Lambda}^{\Lambda} d\varepsilon \frac{1}{A^2+\varepsilon^2} \simeq N_i(0)\int_{-\infty}^{\infty} d\varepsilon \frac{1}{A^2+\varepsilon^2} \tag{150}$$

$$= \frac{\pi N_i(0)}{|A|}. \tag{151}$$

The resulting Eliashberg equations Eqs.(132) and (137) become

$$(1-Z_i(ik_n))ik_n = \frac{\pi}{\beta}\sum_{j,n'} N_j(0)\frac{ik_{n'}X_{i,j}(ik_n,ik_{n'})Z_j(ik_{n'})}{|k_{n'}Z_j(ik_{n'})|}, \tag{152}$$

$$\Delta_i(ik_n) = -\frac{\pi}{\beta Z_i(ik_n)}\sum_{j,n'} N_j(0)\frac{\Gamma_{i,j}(ik_n,ik_{n'})}{|k_{n'}|}\frac{Z_j(ik_{n'})}{|Z_j(ik_{n'})|}\Delta_j(ik_{n'}), \tag{153}$$

where

$$\Gamma_{i,j}(ik_n,ik_{n'}) = \Gamma_{i,j}^{ON}(ik_n,ik_{n'}) + \Gamma_{i,j}^{zz}(ik_n,ik_{n'}) + \Gamma_{i,j}^{\pm}(ik_n,ik_{n'}). \tag{154}$$

It may be reasonable to assume that electrons can be treated as a Fermi liquid, which allows us to invoke $Z_i(ik_n) \geq 1$. Equations (152) and (153) are then reduced to

$$Z_i(ik_n) = 1 - \frac{\pi}{\beta}\sum_{j,n'} N_j(0)\frac{k_{n'}X_{i,j}(ik_n,ik_{n'})}{k_n|k_{n'}|} \tag{155}$$

$$\Delta_i(ik_n) = -\frac{\pi}{\beta Z_i(ik_n)}\sum_{j,n'} N_j(0)\frac{\Gamma_{i,j}(ik_n,ik_{n'})}{|k_{n'}|}\Delta_j(ik_{n'}). \tag{156}$$

Note that the Z dependence on the right band side on Eq.(152) is cancelled out in Eq.(155). Hence we need to solve Eq.(156), which can be regarded as an eigenvalue equation, that is,

$$\lambda\Delta_i(ik_n) = \sum_{j,n'} M_{i,n;j,n'}\Delta_j(ik_{n'}), \tag{157}$$

where the matrix $M_{i,n:j,n'}$ is given by

$$M_{i,n;j,n'} = -\frac{\pi N_j(0)}{\beta}\frac{\Gamma_{i,j}(ik_n,ik_{n'})}{Z_i(ik_n)|k_{n'}|}. \tag{158}$$

Hence the solution of the Eliashberg equation is obtained when λ reaches unity and the superconducting state is realized in $\lambda \geq 1$. We compute the eigenvalues λ of Eq.(157) with decreasing temperature and find the temperature at which $\lambda = 1$ is obtained. The corresponding eigenvector $\Delta_i(ik_n)$ describes the momentum dependence of the pairing gap. While the pairing gap $\Delta_i(ik_n)$ and the renormalization function $Z_i(ik_n)$ depend on Matsubara frequency, we show their momentum dependences at the lowest Matsubara frequency, namely at $k_0 = \pi T$, in Section 3, as usually done in studies of superconductivity.

Chapter 3

Results

Previous studies[23, 30, 31, 32] found that orbital nematic fluctuations can be a high-T_c mechanism of the superconductivity in FeSCs. However, the structure of the pairing gap has not been clarified in the presence of the self-energy effect, although it is observed directly by angle-resolved photoemission spectroscopy (ARPES) and can play a crucial role to identify the mechanism of the superconductivity. Therefore we solve the Eliashberg equations [Eqs.(155) and (156)] numerically by including the self-energy effect [Eq.(155)] and determine the structure of the pairing gap as well as T_c from orbital nematic fluctuations in Section 3.1. In FeSCs, spin fluctuations are also expected to be present. Hence employing the same theoretical framework as orbital nematic fluctuations, we study the superconductivity from spin fluctuations alone in Section 3.2 and from both the orbital nematic and spin fluctuations in Section 3.3. Since spin fluctuations alone turn out to be difficult to realize superconductivity, we also study possible superconductivity from the instantaneous spin interaction in Section 3.4.

3.1 Superconductivity from orbital nematic fluctuations

First we study the superconductivity from the orbital nematic fluctuations [Eq.(92)] by solving Eliashberg equations [Eqs.(155) and (156)] numerically; the spin interactions [Eqs.(101) and (102)] is fully discarded in the present subsection. After clarifying the parameter region, where the orbital nematic phase is stabilized in Section 3.1.1, we consider superconducting instability in the tetragonal phase in Section 3.1.2 and in the nematic phase in Section 3.1.3. Obtained results are summerized in Section 3.1.4.

3.1.1 Static orbital nematic susceptibility

Before studying superconducting instability from orbital nematic fluctuations, we first study the static orbital nematic susceptibility [Eq.(72)]. Figure 28 (a) shows the mo-

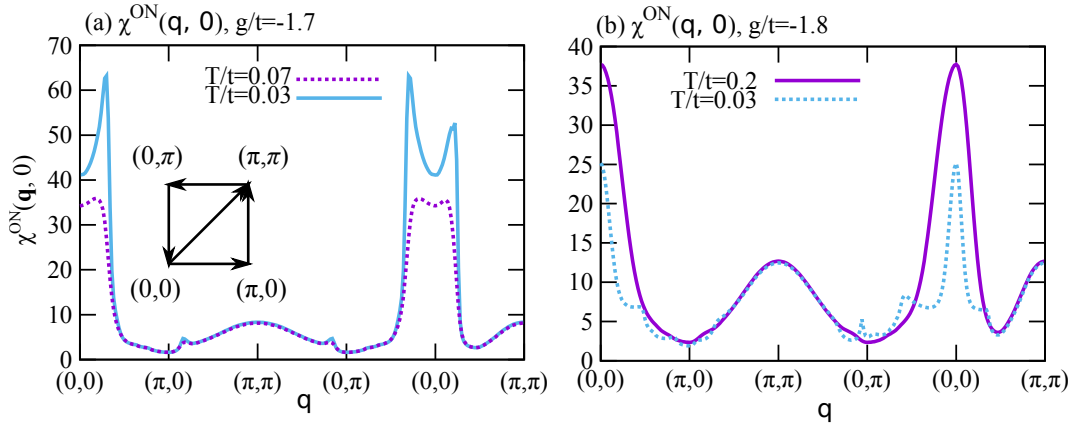

Figure 28: Static orbital nematic susceptibility $\chi^{ON}(\mathbf{q}, 0)$ for several choices of temperature (a) in the tetragonal phase ($g/t = -1.7$) and (b) in the nematic phase ($g/t = -1.8$).

mentum dependence of the static susceptibility for several choices of temperature. The static suseptibility is enhanced around $\mathbf{q} = (0, 0)$. For $g/t = -1.7$, the susceptibility has a peak away from $\mathbf{q} = (0, 0)$ and the peak develops with decreasing temperature [Fig.28 (a)]. The susceptibility, however, does not diverge at any $\mathbf{q}$ down to zero temperature. With increasing the interaction strength g, the peak height increases and the peak position shifts closer to $\mathbf{q} = (0, 0)$. The susceptibility finally diverges at a momentum slightly away from $\mathbf{q} = (0, 0)$ at $g/t = -1.76$ near zero temperature, signalling the orbital nematic phase characterized by the momentum slightly away from $\mathbf{q} = (0, 0)$. This finite $\mathbf{q}$-region is, however, very limited and the susceptibility has a peak at $\mathbf{q} = (0, 0)$ for $g/t = -1.8$ [Fig.28 (b)] and diverges at $T/t \simeq 0.10$. Below this temperature, the orbital nematic order develops. The susceptibility is then suppressed due to the nematic order, but still has a peak at $\mathbf{q} = (0, 0)$ at $T/t = 0.03$ as shown in Fig.28 (b).

The divergence of the static susceptibility [Eq.(74)] determines the phase boundary of the orbital nematic phase. Hence we solve the equation

$$1 + g\chi_0^{\rm ON}(\mathbf{q}, 0) = 0 \tag{159}$$

in the plane of the strength of the orbital nematic interaction g and temperature T. The obtained phase boundary is shown in Fig.29. While there is a small region surrounded by dotted line and the solid line where the orbital nematic order is characterized by a momentum slightly shifted from $\mathbf{q} = (0, 0)$, most of the orbital nematic phase is characterized by the momentum $\mathbf{q} = (0, 0)$.

3.1.2 Superconductivity in the tetragonal phase

We take $g = -1.7t$ where the tetragonal state is stable down to zero temperature as shown in Fig.29. We calculate orbital nematic fluctuations $\tilde{g}_{\rm Ret}(\mathbf{q}, iq_m)$ [Eq.(92)] and obtain the superconducting pairing potential $\Gamma_{i,j}^{\rm ON}$ [Eq.(141)] and the renormalization function

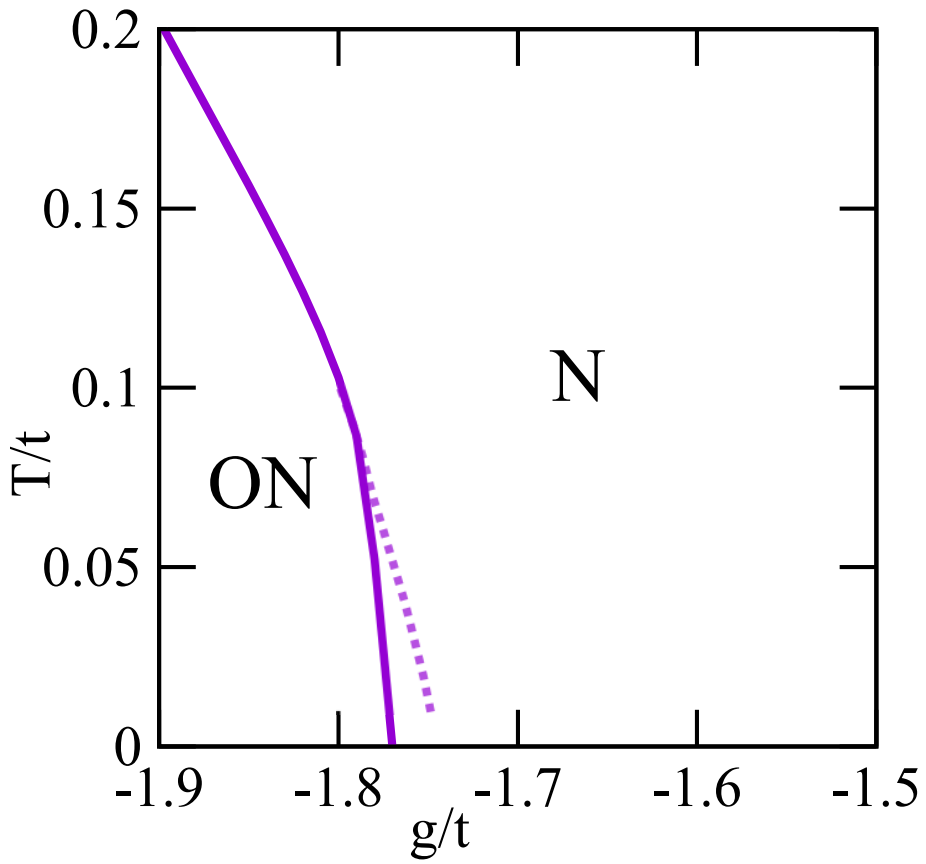

Figure 29: Orbital nematic phase diagram in the plane of the strength of the orbital nematic interaction g and temperature T. The orbital nematic (ON) phase is stabilized below the solid line. In the small region surrounded by the solid and dotted line, the ON order is characterized by a momentum slightly away from $\mathbf{q} = (0, 0)$.

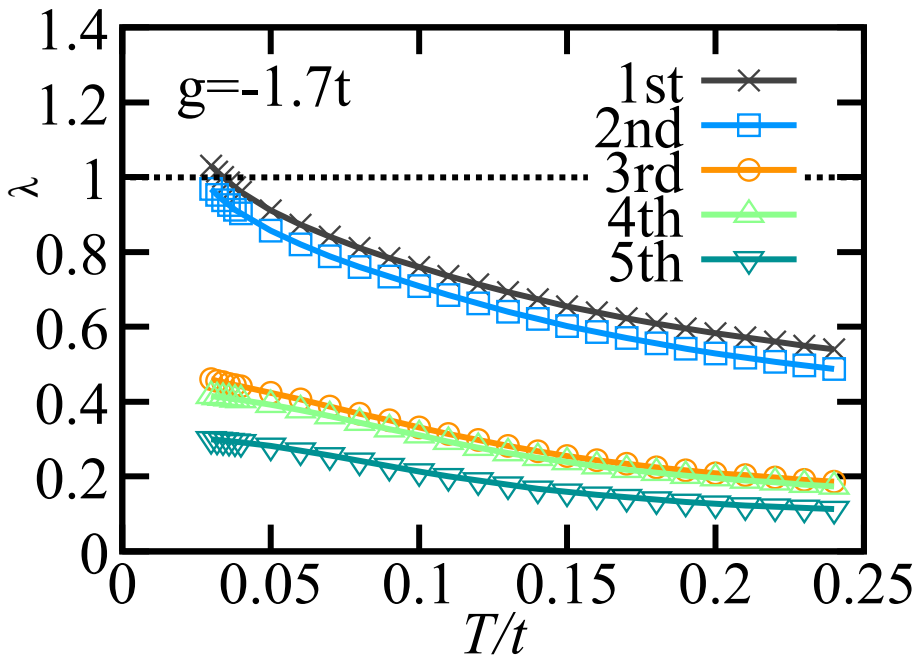

Figure 30: Temperature dependence of the five largest eigenvalues of the Eliashberg equations in the tetragonal phase ($g/t = -1.7$). At $T = 0.034t$, the largest eigenvalue exceeds unity, where the superconducting instability occurs.

$Z_i(ik_n)$ [Eq.(155)]. We then diagonalize the matrix Eq.(158) numerically and calculate its eigenvalues and eigenvectors at various temperatures. The temperature at which the largest eigenvalue exceeds unity is the onset temperature of superconductivity and the corresponding eigenvector describes the momentum dependence of the superconducting gap.

We show five largest eigenvalues as a function of temperature in Fig.30. With decreasing temperature, all those eigenvalues are enhanced and the largest eigenvalue exceeds unity at $T_c/t = 0.034$, where the superconducting instability occurs. Because we have allowed the momentum dependence of the pairing gap, there is a possiblity that T_c could be increased compared with T_c obtained in Ref.[32] where the pairing gap on each Fermi pocket is assumed to be constant. However, obtained T_c turns out to be almost the same as that in Ref.[32].

We show the gap function corresponding to the largest eigenvalue at T_c along each Fermi pocket in Fig.31. The pairing gap has the same sign on all FSs. In this sense, the pairing gap is characterized by s_{++}-wave symmetry. The modulation of the gap is at most 4% on FS2 and thus the pairing gap is considered to be almost isotropic. The weak modulation on the hole pockets can be understood in terms of the orbital components on each Fermi pocket (see Fig.10), that is, the gap is slightly suppressed around a region where the two orbitals have the same weight on the hole pockets around $\theta = \pi/4, 3\pi/4, 5\pi/4$, and $7\pi/4$. On the other hand, the very small modulation on the

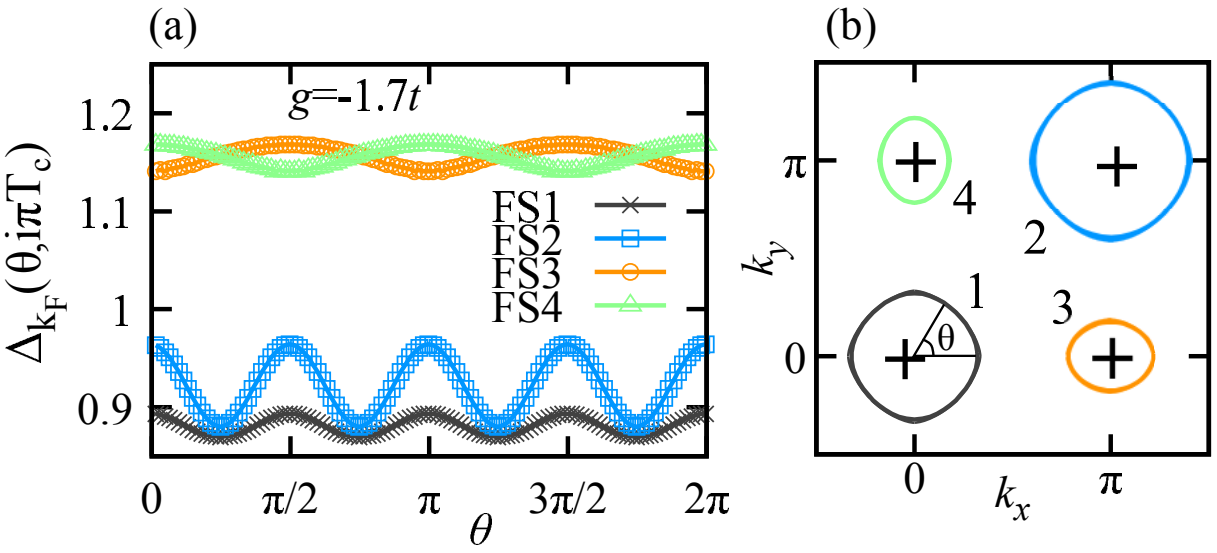

Figure 31: (a) Momentum dependence of the leading pairing gap in the tetragonal phase at $T = T_c$. The horizontal axis θ is an angle measured from the k_x axis on each Fermi pocket shown in (b). (b) Sketch of the pairing gap, where the size of the gap is expressed with the thickness of each Fermi pocket.

electron pockets comes from the shape of the Fermi surfaces. The gap becomes larger on a region where the curvature of the electron pockets is smaller. We defer the pairing gap corresponding to subleading instabilities to the Appendix (Section 5.1). Here we just mention that the second largest eigenvalue corresponds to $d_{x^2-y^2}$-wave superconductivity and is nearly degenerate with the leading one, similar to the previous study [32].

Figure 32 shows the momentum dependence of the renormalization function [Eq.(155)]. On the electron pockets a value of Z is around 1.6 and is nearly isotropic on the hole pockets. Z might seem to have a large anisotropy, but the anisotropy is at most 6%. A value of Z becomes as large as around 3.6 on the electron pockets, which indicates that orbital nematic fluctuations lead to strong-coupling superconductivity, not weak-coupling BCS superconductivity.

To clarify the major scattering processes to drive the superconductivity, we compute the eigenvalues of the Eliashberg equations for three different scattering processes, namely within the the same Fermi pockets ("Intra"-scattering processes), between the hole and electron pockets ("$(\pi, 0)$"-scattering processes), and between the different hole (electron) pockets ("(π, π)"-scattering processes) [see Fig.33 (b)]. The eigenvalue of the Eliashberg equation, denoted by "All" in Fig.33 (a), is computed by considering all three scattering processes and is almost reproduced only by the intra-Fermi-pocket scattering processes. This means that the superconductivity from orbital nematic fluctuations is driven essentially by the scattering processes with a small momentum transfer. This result is reasonable because orbital nematic fluctuations occur around momentum transfer $\mathbf{q} = (0, 0)$.

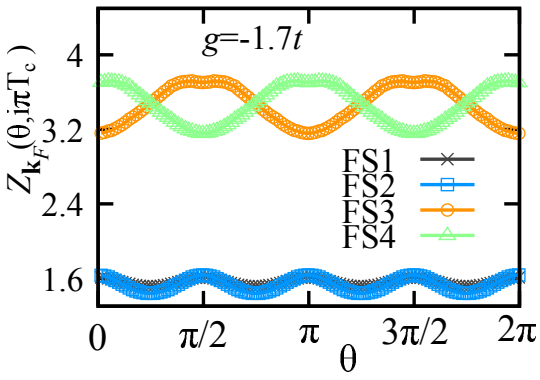

Figure 32: Momentum dependence of the renormalization function along each pocket in the tetragonal phase ($g/t = -1.7$); θ is defined in Fig.31 (b). The color corresponds to each Fermi pocket.

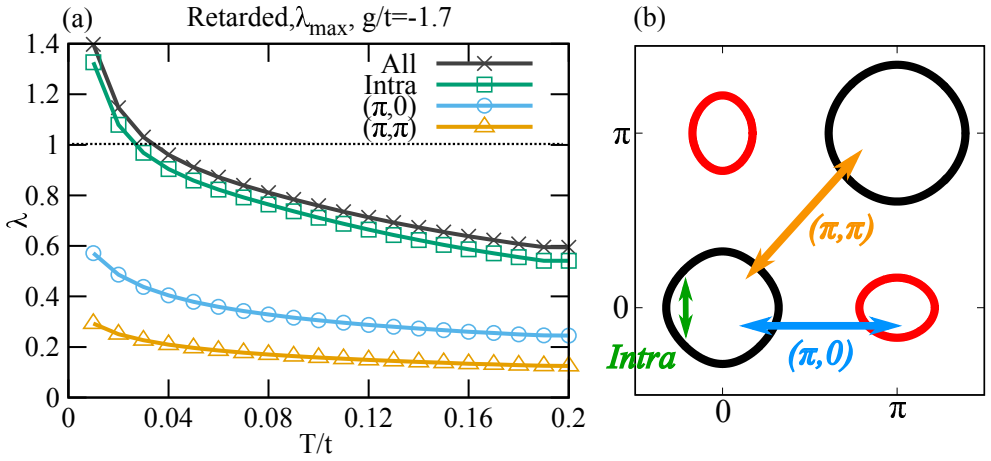

Figure 33: (a) The temperature depenence of the largest eigenvalues in the tetragonal phase for specific scattering processes. "All" denotes that all scattering processes are considered and is the same as the largest eigenvalue in Fig.30. "Intra" considers scattering processes only within the same Fermi pocket, "$(\pi, 0)$" only between hole and electron pockets, and "(π, π)" only between the hole (electron) pockets, as shown in (b). (b) Sketch of scattering processes. There are three different scattering processes: intra Fermi-pocket scattering processes (green), $(\pi, 0)$-scattering processes (blue), and (π, π)-scattering processes (orange).

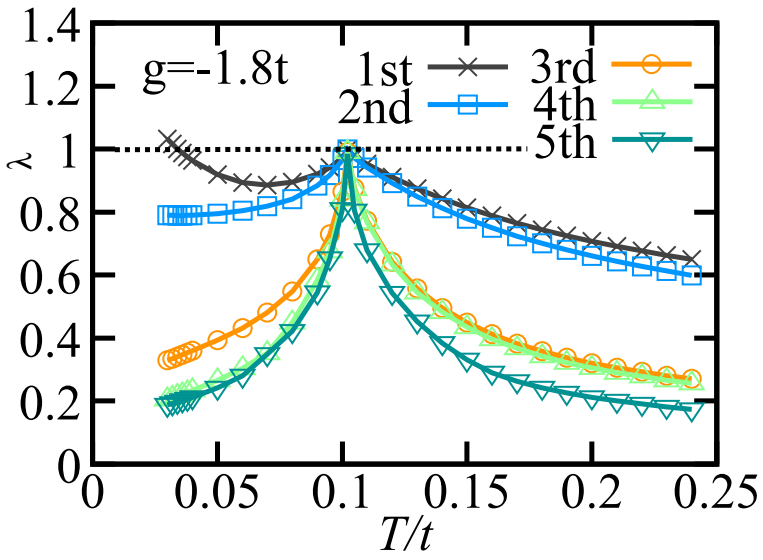

Figure 34: Temperature dependence of the eigenvalues of the Eliashberg equations for $g/t = -1.8$. The eigenvalues are plotted from the first to the fifth largest ones.

Orbital nematic fluctuations, also contain fluctuations with large momentum transfer, although they are weak. It is rather surprising that those weak fluctuations especially "$(\pi, 0)$" processes in Fig.33 (a) can lead to the eigenvalue as large as $\lambda \simeq 0.6$ at low temperature. In Fig.33 (a), the eigenvalue of "All" processes becomes slightly larger than that of "Intra" processes. This indicates that all scattering processes contained in orbital nematic fluctuations work cooperatively to drive the superconductivity.

3.1.3 Superconductivity inside the nematic phase

Next we choose $g = -1.8t$ in Fig.29, where orbital nematic instability occurs at $T_{\rm ON} \simeq 0.10t$. Below $T_{\rm ON}$, the orbital nematic order n_- becomes finite. A value of n_- is determined by solving the self-consistent equation [Eq.(63)] and its temperature dependence is already shown in Fig.12. This nematic order leads to breaking of fourfold symmetry; FS1 and FS4 (FS2) are elongated along the k_y (k_x) direction whereas FS3 becomes small to shrink as shown in Fig.10. The effect of the nematic order enter Eq.(59) and nematic fluctuations inside the nematic phase are computed by using the dispersion Eq.(59). As expected, the orbital nematic susceptibility is strongly suppressed with increasing the nematic order parameter as shown in Fig.28 (b). A natural question is whether superconductivity occurs even in such a situation.

We solve the Eliashberg equations [Eqs.(155) and (156)] for $g = -1.8t$ and its eigenvalue is plotted as a function of temperature in Fig.34. With decreasing temperature, not only the largest eigenvalue but also the second, third, fourth and fifth largest one increase and approach unity at $T/t \simeq 0.10$. This temperature corresponds to $T_{\rm ON}$, namely the onset temperature of the orbital nematic phase. All the eigenvalues, however, do

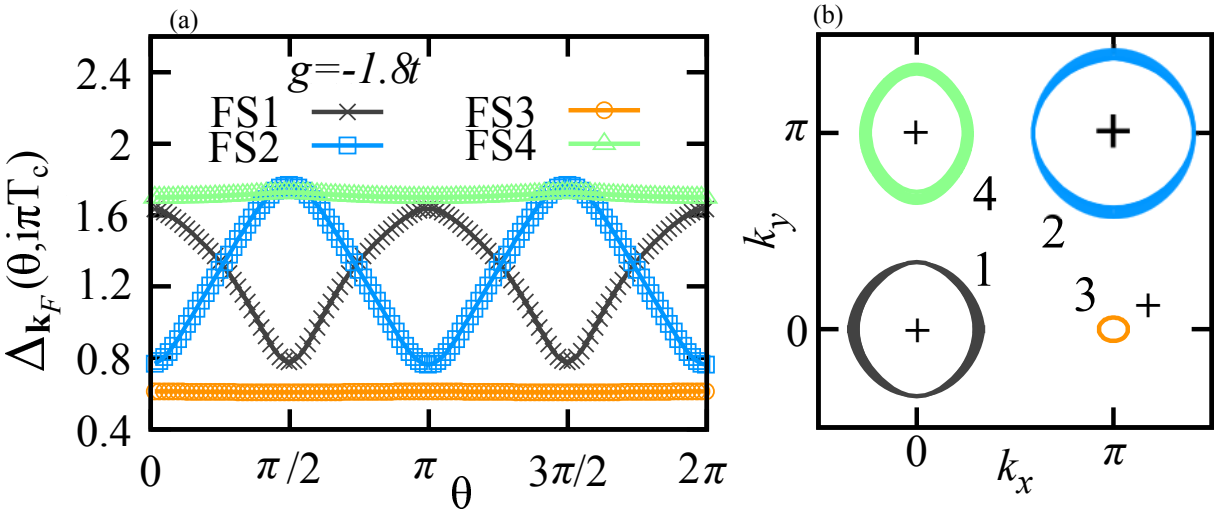

Figure 35: Momentum dependence of the leading pairing gap along each Fermi pocket in the nematic phase ($g/t = -1.8$). See the caption in Fig.31 for details.

not exceed unity and instead are suppressed below $T_{\rm ON}$, leaving a cusp structure there. This seemingly odd result is easily understood in terms of the self-energy effect. Around $T_{\rm ON}$, the orbital nematic fluctuations become very strong, which tends to drive the superconductivity. On the other hand, the renormalization function $Z_i(ik_n)$ [Eq.(155)] is also enhanced around $T_{\rm ON}$, which tends to suppress the superconducting instability. These two opposite effects make a cusp around $T_{\rm ON}$ in Fig.34 and the resulting superconducting instability does not occur. When the system enters the nematic phase below $T_{\rm ON}$, orbital nematic fluctuations are suppressed due to the development of the nematic order [see Figs.28 (b) and 12]. All eigenvalues in Fig.34, therefore, are suppressed below $T_{\rm ON}$. However, the largest eigenvalue starts to increase below $T \simeq 0.07t$ and finally exceeds unity at $T_c/t = 0.034$ where the superconducting instability occurs.

The corresponding pairing gap in the leading instability is shown in Fig.35. The symmetry of the pairing gap remains s_{++}-wave even in the nematic order. The pairing gap stays nearly isotropic on the electron pockets, but it acquires a large anisotropy on the hole pockets. The modulation becomes as large as 40% with a large gap at $\theta = 0, \pi$ ($\pi/2$, $3\pi/2$) on the FS1 (FS2). This modulation can be understood in terms of the orbital components on each Fermi pocket (see Fig.10). In the nematic phase, the d_{xz}-orbital is occupied more than the d_{yz}-orbital. The pairing gap then becomes large (small) on the region where d_{xz} (d_{yz})-orbital is dominant, leading to a large modulation of the pairing gap. For the pairing gap corresponding to other eigenvalues, see the Appendix (Section 5.1).

While values of Z (Fig.36) on FS1 and FS2 do not change much compared with the corresponding results in the tetragonal phase (Fig.32), the nematic order strongly suppresses Z to be $\simeq 2.5$ and $\simeq 1.8$ on FS3 and FS4, respectively. This is because

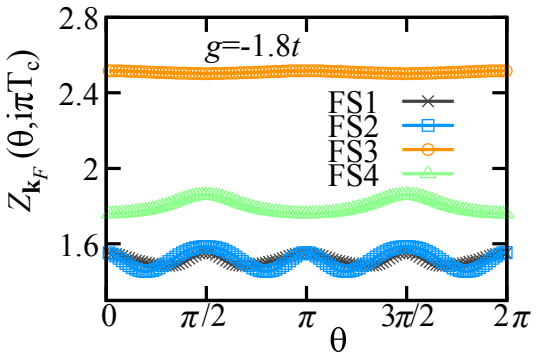

Figure 36: Momentum dependence of the renormalization function along each pocket in the nematic phase ($g/t = -1.8$).

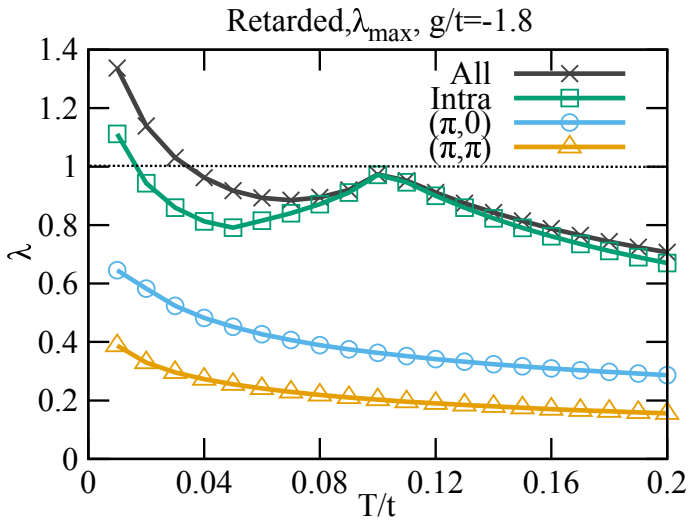

Figure 37: Temperature dependence of the largest eigenvalues of the Eliashberg equations for various scattering processes, "All", "Intra", "$(\pi, 0)$", and "(π, π)"; see the caption in Fig.33.

nematic fluctuations are suppressed inside the nematic phase, although they are still strong enough to drive superconductivity (Fig.34).

To clarify the major scattering processes driving the superconductivity inside the nematic phase, we compute the eigenvalue of the Eliashberg equations by classifying scattering processes into three: within the same Fermi pocket, between the hole and electron pockets, and between the different hole (electron) pockets; See Fig.33 (b). Obtained eigenvalues are plotted as a function of temperature in Fig.37. Intra-pocket scattering processes are the major contributions to the superconductivity inside the nematic phase. However, scattering processes of "$(\pi, 0)$" and "(π, π)" yield sizable eigenvalues, which reash as large as 0.6 and 0.4, respectively, at lowest temperature. The three different scattering processes work cooperatively in the sense that the eigenvalue of "All" becomes larger than that of "Intra".

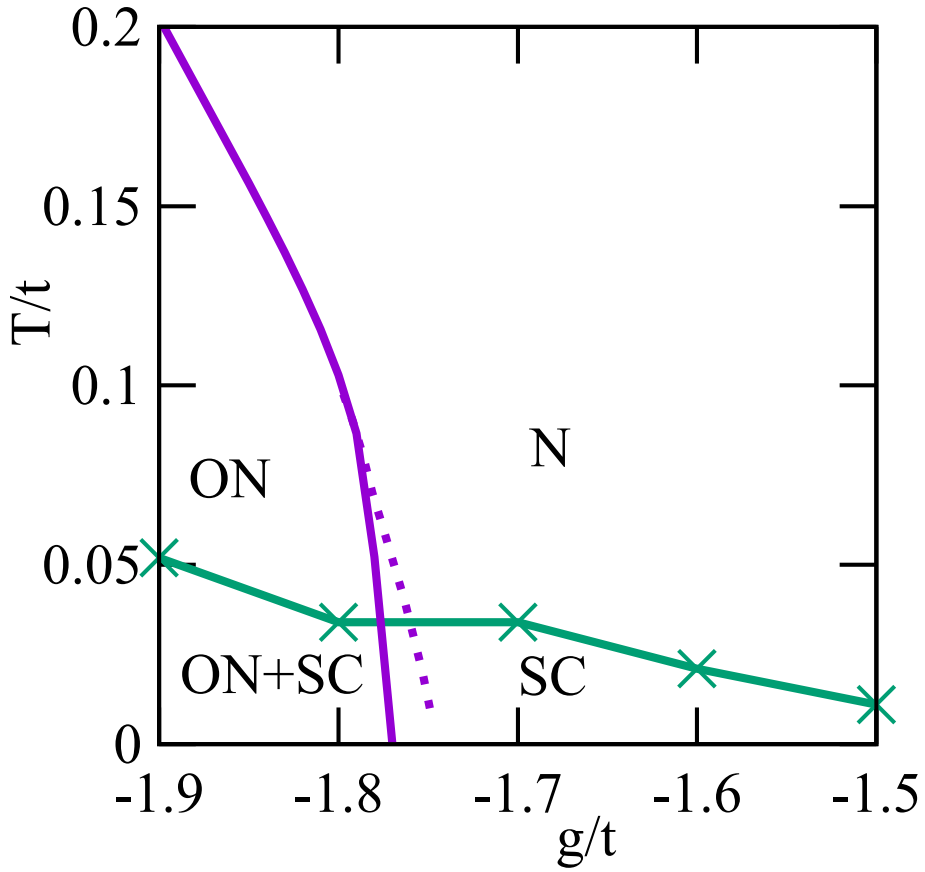

Figure 38: Phase diagram when considering only the orbital nematic fluctuations in the plane of the interaction strength g/t and the temperature T/t. The purple line shows the boundary of orbital nematic phase (ON) and the green line the boundary of the superconducting phase (SC). "N" is the normal metallic phase, namely the tetragonal phase.

3.1.4 Summary of superconductivity from orbital nematic fluctuations

We perform similar calculations in both tetragonal and nematic phases by choosing different values of g and summarize obtained T_c in Fig.38. T_c tends to be enhanced upon approaching the orbital nematic phase. The superconducting instability occurs also inside the nematic phase, which may lead to the coexistence of the superconductivity and the orbital nematic order at lower temperature. Our T_c is enhanced upon deeply entering the nematic phase. This may be due to the subtle balance among three factors: i) a value of g becomes larger, which induces stronger fluctuations, ii) nematic fluctuations are suppressed inside the nematic phase, which is not favorable to superconducting instability from a view of the pairing potential, and iii) on the other hand, the suppression of the nematic fluctuations inside the nematic phase is favorable to the superconductivity from a view of the self-energy effect. For $g/t = -1.9$, FS3 disappears due to a large nematic order. However, a high T_c is still obtained and the gap structure is qualitatively the same as that for $g/t = -1.8$ (Fig.35); See the Appendix (Section 5.1) for details. In our phase diagram (Fig.38), T_c varies from $0.01t$ to $0.05t$. Since a comparison with first-principle calculations[15] suggests that the value of t is about 150 meV, orbital nematic fluctuations can drive T_c with $15K - 75K$, which is comparable to T_c in FeSCs. Therefore we confirm that orbital nematic fluctuations indeed provide a new high-T_c mechanism after our achieving more complete calculations including the momentum dependence of the pairing gap, which was neglected in the previous study [32]. While the pairing gap is almost isotropic s_{++}-wave in the tetragonal phase, it acquires a large anisotropy on the hole pockets in the nematic phase, although the gap on the electron pockets remains almost isotropic.

3.2 Superconductivity from spin fluctuations

In FeSCs, spin fluctuations are also expected to be present. Given that there are much less studies about the self-energy effect and the actual value of T_c of superconductivity in the spin fluctuation mechanism, it is worthwhile studying possible superconductivity due to spin fluctuations in the same theoretical scheme as the orbital nematic case. As a pairing interaction [Eqs.(143) and (145)], we consider only spin fluctuations and discard orbital nematic fluctuations in this section. To study the effect of the nematic order, we shall introduce a finite strength of the orbital nematic interaction g $(= -1.8t)$, but even in such a case, associated nematic fluctuations are still discarded in this section. As mentioned in Section 2 we consider two types of spin interactions, namely the Lorentz type [Eq.(36)] and the $J_1 - J_2$ type [Eq.(40)]. We first study the superconductivity from the Lorentz-type spin fluctuations in Section 3.2.1, and the $J_1 - J_2$-type spin fluctuations in Section 3.2.2. Obtained results are summarized in Section 3.2.3.

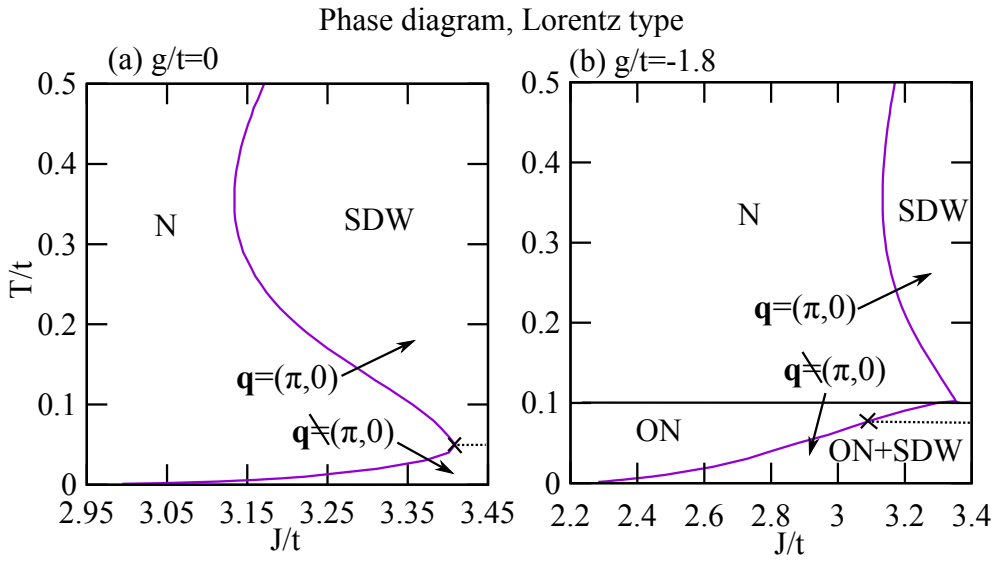

Figure 39: Magnetic phase diagram due to the Lorentz-type spin fluctuations (a) in the absence of the nematic order ($g/t = 0$) and (b) in the presence of the nematic order at low temperature ($g/t = -1.8$). "N" stands for the normal metallic (tetragonal) phase and the SDW phase can be characterized by the momentum slightly away from $\mathbf{q} = (\pi, 0)$ below the temperature marked by cross. The solid line in (b) denotes the onset temperature of the orbital nematic order.

3.2.1 Lorentz-type spin interaction

We study the superconductivity from the Lorentz-type spin fluctuations [Eq.(36)], which may correspond to the itinerant limit of the spin interaction (see discussions in Section 2.1.3). We first consider the case in the absence of the nematic order and determine a magnetic phase diagram [Fig.39 (a)] in the plane of the spin interaction strength J [see Eq.(36)] and temperature T by the solving the equation

$$1 + J(\mathbf{q})\chi^{zz}(\mathbf{q}, 0) = 0, \tag{160}$$

where the static spin susceptibility diverges [see Eq.(82)]. The parameter Γ in Eq.(36) is fixed $\Gamma = 1.0$ in this thesis. We find that the transition line starts to bend inward below $T \simeq 0.3t$ and bend back outward below $T \simeq 0.05t$. To understand this peculiar dependence, we show the $\mathbf{q}$-dependence of the static susceptibility [Eq.(82)] in Fig.40 (a) in the tetragonal phase at $T/t = 0.10$ and 0.01 for $J/t = 3.20$. Since these susceptibility is calculated in the tetragonal phase, the peaks at $\mathbf{q} = (\pi, 0)$ and $(0, \pi)$ are equivalent. We find that the bending in $0.3t \geq T \geq 0.05t$ comes from the fact that the Fermi surface nesting does not occur perfectly at $\mathbf{q} = (\pi, 0)$ and $(0, \pi)$ (see Fig.10), and thus the resulting susceptibility is suppressed at $\mathbf{q} = (\pi, 0)$ and $(0, \pi)$ at lower T. The peak position then shifts slightly away from $\mathbf{q} = (\pi, 0)$ and $(0, \pi)$ as shown in the results at $T = 0.01t$ in Fig.40 (a). With further decreasing temperature, the susceptibility diverges at $\mathbf{q} \neq (\pi, 0)$,

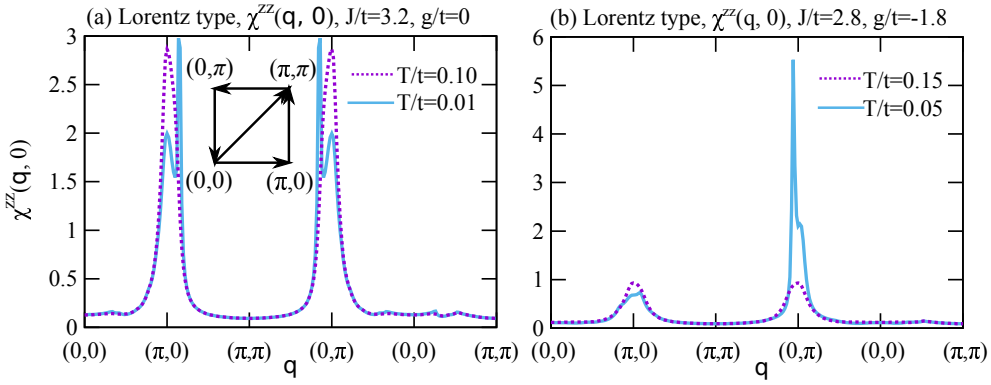

Figure 40: Static spin susceptibility $\chi^{zz}(\mathbf{q}, 0)$ for the Lorentz-type spin interaction for several choices of temperature (a) in the absence of the nematic order ($g/t = -1.7$) and (b) in the presence of the nematic order at lower temperature ($g/t = -1.8$) along the line illustrated in the inset.

leading to SDW phase characterized by the momentum slightly far away from $\mathbf{q} = (\pi, 0)$. As a result, the transition line has a tale below $T/t = 0.05t$ in Fig.39 (a).

To explore possible superconductivity near the SDW phase we solve the Eliashberg equations [Eqs.(155) and (156)] by considering spin fluctuations alone [Eqs.(143) and (145)]; not only orbital nematic fluctuations [Eq.(141)] but also the instantaneous spin interaction [Eq.(101)] is discarded. The eigenvalue of the Eliashberg equations is plotted in Fig.41 (a) as a function of temperature, where we also plot the eigenvalue for three different scattering processes: "Intra", "$(\pi, 0)$", and "(π, π)" scattering processes in the same way as Fig.33. The eigenvalue from the $(\pi, 0)$ scattering procceses (blue) is the largest, indicating that the spin fluctuations with momentum transfer around $\mathbf{q} = (\pi, 0)$ tend to drive superconductivity. However, the largest eigenvalue does not reach unity even in the vicinity of the SDW transitions [see Fig.39 (a) for $J/t = 3.2$ at $T/t \simeq 0.01$]. On the other hand, the eigenvalues from the intra-pocket scattering processes (green) and the (π, π) scattering processes (orange) are quite small. In particular, the former is almost zero. Hence one would safely neglect the intra-pocket scattering processes. However, the intra-pocket scattering processes play an important role. In fact, the eigenvalue from all scattering processes (gray line) is almost reproduced by considering $(\pi, 0)$- and intra-pocket-scattering processes (yellow line). This means that the weak intra-pocket scattering processes suppress the eigenvalues coming from the $(\pi, 0)$ scattering processes about 7%. The intra-pocket scattering processes occur for a small $\mathbf{q}$, typically around $\mathbf{q} = (0, 0)$. Given that the static susceptibility becomes very weak around $\mathbf{q} = (0, 0)$ [Fig.40 (a)], spin fluctuations associated with a small $\mathbf{q}$ are also very small. It is surprising that such weak fluctuations are responsible for the suppression of the eigenvalue. We call this suppression as a self-restraint effect of superconductivity due to spin fluctuations in the sense that dominant spin fluctuations around momentum transfer $\mathbf{q} = (\pi, 0)$ necessarily have some tail far away $\mathbf{q} = (\pi, 0)$, yielding very weak intra-pocket scattering

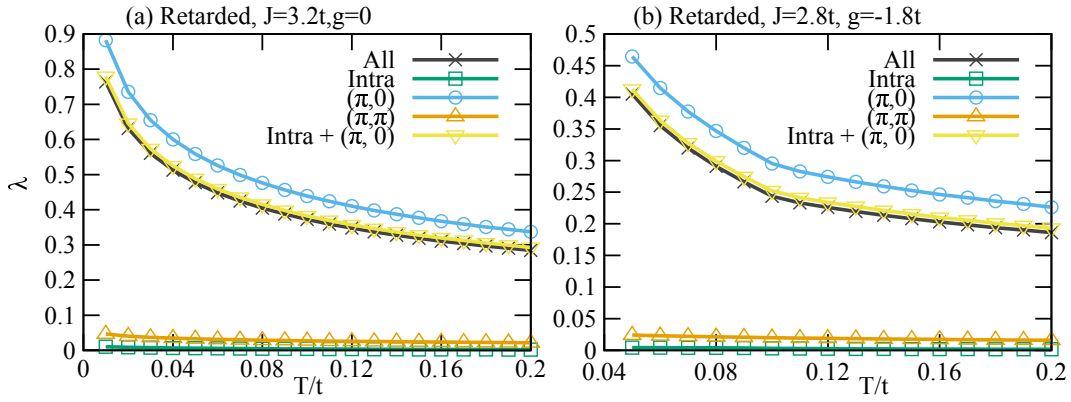

Figure 41: Temperature dependence of eigenvalues for the Lorentz-type spin fluctuations (a) in the tetragonal phase ($J/t = 3.2, g/t = 0$) and (b) in the nematic phase ($J/t = 2.8, g/t = -1.8$). See the caption in Fig.33 for the legend.

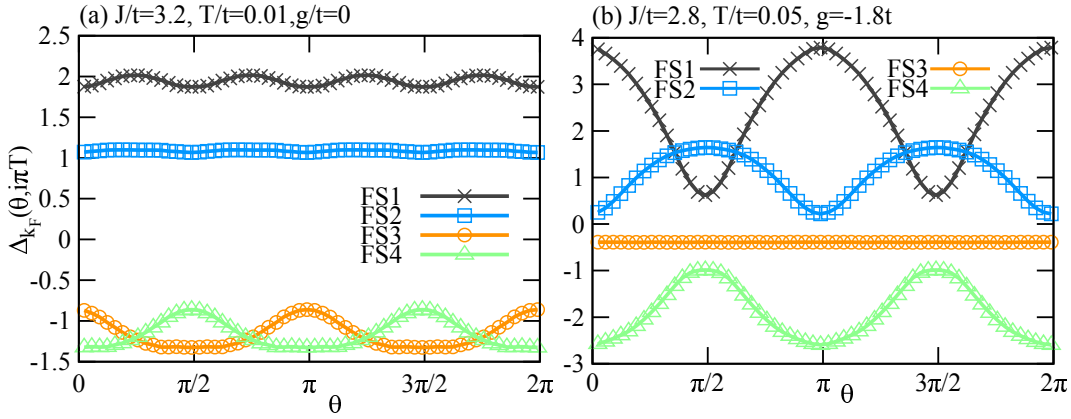

Figure 42: Momentum dependence of the pairing gap due to the Lorentz-type spin fluctuations at the lowest temperature (a) in the tetragonal phase ($g/t = 0$) and (b) in the nematic phase ($g/t = -1.8$). The angle θ is measured from the k_x axis; see Fig.31.

processes, which in turn suppress the tendency of the superconducitng instability. As a result, the eigenvalue corresponding to "All" tends to be suppressed and spin fluctuations cannot drive superconductivity even close to the SDW phase. Note that if the self-energy effect is neglected, we would obtain $\lambda = 1$ as we shall discuss in Section 5.2.2.

Although the eigenvalues do not reach unity, we show the momentum dependence of the pairing gap at the lowest temperature ($T/t = 0.01$) in Fig.42 (a). On the hole pockets (FS1 and FS2) the pairing gap is almost isotropic, while the gap becomes anisotropic on the electron pockets (FS3 and FS4) with its modulation about 20%. The pairing gap has the opposite sign between the gap on the hole and electron pockets, indicating $s_{\pm}$-wave symmetry. Our obtained gap structure is consistent with typical results for the possible superconductivity driven by spin fluctuations in FeSCs[15].

The momentum dependence of the corresponding renormalization function is shown

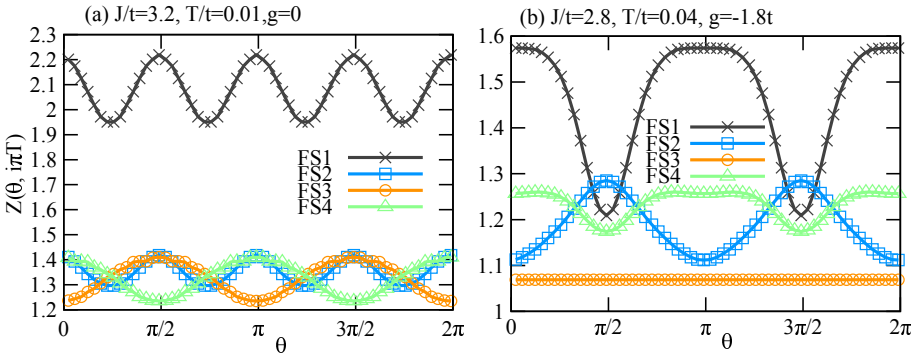

Figure 43: Momentum dependence of the renormalization function due to the Lorentz-type spin interaction (a) in the tetragonal phase and (b) in the nematic phase ($g/t = -1.8$).

in Fig.43 (a). The modulation is very weak at most 6% and can be regarded to be almost isotropic. A value of Z becomes the highest on the hole pocket around $\mathbf{q} = (0, 0)$ (FS1) and is about 2.2, whereas it is about 1.3 on the other pockets. These values of Z are smaller than the corresponding results for the orbital nematic fluctuations (see Fig.32). In this sense, the self-energy effect is weaker for spin fluctuations.

Although we cannot obtain the superconductivity from spin fluctuations, we make a phase diagram by drawing contour lines of the eigenvalues of the Eliashberg equations in Fig.44 (a). The eigenvalues become larger near the SDW phase and at lower temperature, but the superconductivity does not occur even very close to the SDW phase, because of the self-energy effect and the self-restraint effect of superconductivity from spin fluctuations.

Impact of the orbital nematic order

We next study possible superconductivity in the orbital nematic phase, where the system breaks fourfold symmetry and becomes anisotropic. We take $g/t = -1.8$ to realize the nematic phase below $T_{\rm ON} \simeq 0.10t$ (Fig.29), but note that we discard orbital nematic fluctuations and consider exclusively spin fluctuations [Eqs.(143) and (145)]; the instantaneous spin interaction [Eq.(101)] is also neglected. Our calculations are essentially the same as those in the tetragonal phase. The differences lie in the following two: i) the nematic order parameter n_- is determined for $g/t = -1.8$ and the band dispersion Eq.(59) is employed, instead of Eqs.(2) and (3), and ii) we take $J/t = 2.8$ to consider the superconductivity, instead of $J/t = 3.2$ because the nematic order changes the magnetic phase boundary. To highlight the effect of the nematic order, we present the corresponding results on the right hand in Figs.39-44.

Figure 39 (b) is the magnetic phase diagram constructed by solving Eq.(160). The phase diagram is essentially the same as Fig.39 (a): bending of the phase boundary and a magnetic phase characterized by the momentum slightly away from $\mathbf{q} = (\pi, 0)$ at low temperature. A crucial difference between Figs.39 (a) and (b) is a scale of the horizontal

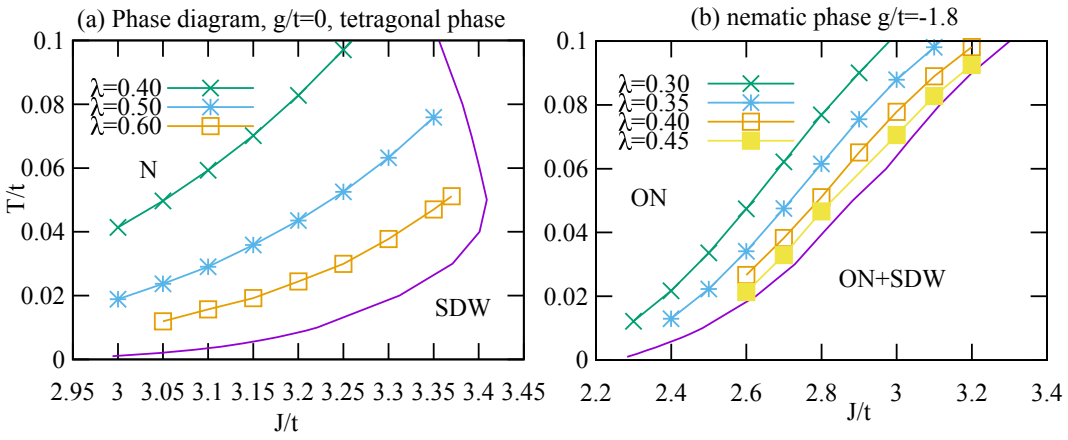

Figure 44: Phase diagram in the plane of the strength of the Lorentz-type spin interaction J and temperature T. Because the superconducting instability does not occur, the contour lines of the eigenvalues of Eliashberg equations are drawn. Purple line is a phase boundary between (a) the normal metallic (tetragonal) phase (N) and the SDW phase, and (b) the orbital nematic (ON) phase and the SDW phase: The nematic phase in (b) changes to the tetragonal phase above $T_{\rm ON} \simeq 0.10t$ for $g = -1.8t$.

axis. To see this reason, we plot the static spin susceptibility $\chi^{zz}(\mathbf{q}, 0)$ in Fig.40 (b). The susceptibility shows two peaks at $(\pi, 0)$ and $(0, \pi)$ for $J = 3.2t$ at $T = 0.15t$. With decreasing temperature, the orbital nematic order n_- develops below $T_{\rm ON} \simeq 0.10t$ (see Fig.12) and each Fermi pocket starts to deform as shown in Fig.10 (b). In particular, the electron pocket around $\mathbf{k} = (\pi, 0)$ (FS3) starts to shrink. As a result, the nesting between hole and electron pocket with momentum $\mathbf{q} = (\pi, 0)$ becomes much worse than that with $\mathbf{q} = (0, \pi)$. Hence the susceptibility exhibits a big anisotropy between $\mathbf{q} = (\pi, 0)$ and $(0, \pi)$ at low temperature and the peak around $\mathbf{q} = (0, \pi)$ is enhanced in the nematic phase as shown in Fig.40 (b). This is the reason why a smaller value of J can drive the SDW instability inside the nematic phase. The shift of the peak from $\mathbf{q} = (0, \pi)$ does not come from the nematic order, but from the fact that the Fermi-surface nesting is not perfectly for $\mathbf{q} = (0, \pi)$ as discussed in the case of the Lorentz-type spin interaction.

A comparison between the left and the right panel in Fig.41 shows that the eigenvalues tend to be suppressed by the nematic order, but the results are qualitatively the same. In particular, the eigenvalue obtained for "$(\pi, 0)$"-scattering processes is suppressed mainly by the intra-pocket scattering processes, although almost zero eigenvalue is obtained for intra-pocket scattering processes alone.

The pairing gap [Fig.42 (b)] is still characterized by $s_\pm$-wave symmetry in the nematic phase. The gap on FS1 and FS4 acquires a large modulation and has a nodelike structure around $\theta = \pi/2$ and $3\pi/2$. A large modulation also yields a nodelike structure on FS2 around $\theta = 0$ and π. The pairing gap becomes large (small) on a Fermi surface segment where the d_{xz} (d_{yz})-component is dominant in the nematic phase, although the large

modulation of the gap on FS4 cannot be understood in terms of the orbital components (see also Fig.10). The pairing gap on FS3 is nearly zero because FS3 substantially shrinks to be very small by the nematic order.

The renormalization function also acquires a large momentum dependence especially on FS1 as shown in Fig.43 (b). and it drops around $\theta = \pi/2$ and $3\pi/2$ where the minor orbital d_{yz}-orbital is dominant. The momentum dependence of Z on FS2 and FS4 is qualitatively the same as that in the tetragonal phase [Fig.43 (a)]. The value of Z on FS3 is nearly isotropic and close to 1, where d_{yz}-orbital is dominant and the self-energy effect is very small.

Contour lines of the eigenvalue are drawn in the phase diagram in Fig.44 (b). The eigenvalues become smaller than those in the tetragonal phase even very close to the SDW phase. Therefore the superconducting instability is more difficult in the nematic phase than the tetragonal phase, although the instability itself does not occur in both cases.

3.2.2 $J_1 - J_2$-type spin interaction

We next consider the $J_1 - J_2$-type spin fluctuations [Eq.(40)], which may mimic a situation where spins are characterized by localized spins (see Section 2.1.3). We fix $J_1/t = 1.0$ in Eq.(40) in this thesis. All calculations are fully parallel to those in Section 3.2.1 except for the choice of $J(\mathbf{q})$. Obtained results for the $J_1 - J_2$-type spin interaction turn out to be qualitatively the same as those for the Lorentz-type spin interaction. However, it may be worthwhile presenting briefly quantitative differences between the Lorentz- and $J_1 - J_2$-type spin interaction because some FeSCs may be characterized by the limit of localized spins better than the limit of itinerant spins.

A magnetic phase diagram is shown in Fig.45 (a). Similar to the case of the Lorentz-type spin interaction [Eq.(36)], the magnetic phase boundary first bends inward and bends back outward at lower temperature. This peculiar feature is understood by studying the temperature dependence of the static spin susceptibility. Figure 46 (a) shows the susceptibility $\chi^{zz}(\mathbf{q}, 0)$ [Eq.(82)] as a function of $\mathbf{q}$. $\chi^{zz}(\mathbf{q}, 0)$ exhibits a peak at $\mathbf{q} = (\pi, 0)$ and $(0, \pi)$ at high temperature. With decreasing temperature, the susceptibility is suppressed and a peak position slightly shifts away from $\mathbf{q} = (\pi, 0)$ and $(0, \pi)$. This peak originates from the Fermi-surface nesting between the hole and electron pockets and the nesting vector is deviated slightly from $\mathbf{q} = (\pi, 0)$ and $(0, \pi)$. With further decreasing temperature, the peak develops strongly and eventually diverges at low temperature, signalling the SDW instability.

Figure 47 (a) shows the temperature dependence of the eigenvalues of the Eliashberg equation. The full eigenvalue ("All") is reproduced by considering the intra-pocket and "$(\pi, 0)$"-scattering processes. Given that the eigenvalue for the "$(\pi, 0)$"-scattering processes is larger by a factor 1.5 than the full eigenvalue ("All"), the suppression due to the intra-pocket scattering processes is substantial although spin fluctuations contributing to the intra-pocket scattering processes have small momentum transfer around $\mathbf{q} = (0, 0)$

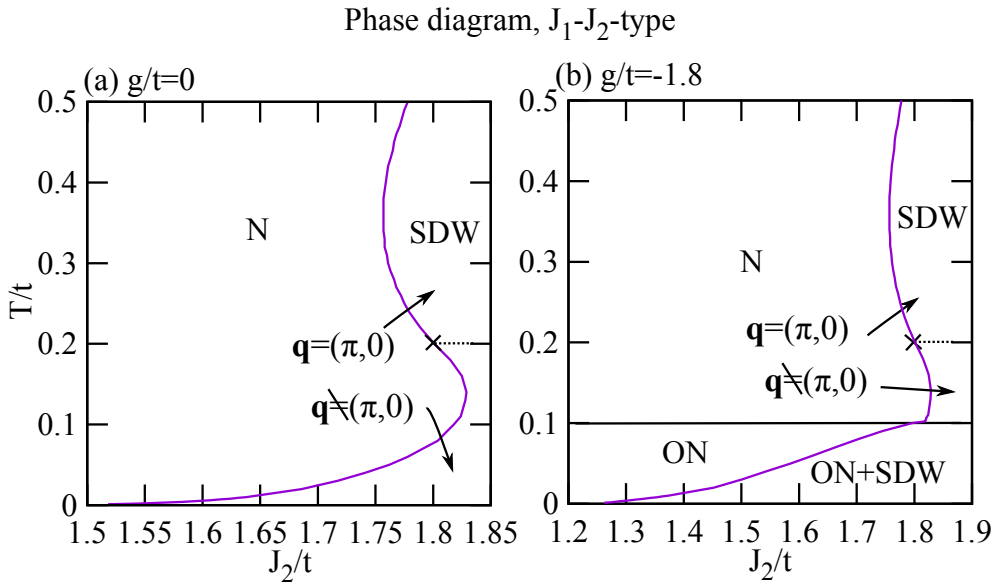

Figure 45: Magnetic phase diagram due to the $J_1 - J_2$-type spin fluctuations (a) in the absence of the nematic order ($g/t = 0$) and (b) in the presence of the nematic order at low temperature ($g/t = -1.8$). "N" stands for the normal metallic (tetragonal) phase and the SDW phase can be characterized by the momentum slightly far away from $\mathbf{q} = (\pi, 0)$ below the temperature marked by cross. Black solid line denotes the orbital nematic transition at $T_{\rm ON} \simeq 0.10t$.

and thus are very weak. In fact, the spin susceptibility is strongly suppressed around $\mathbf{q} = (0, 0)$ in Fig.46 (b). Therefore the self-restraint effect of superconductivity is much more pronounced than the Lorentz-type spin fluctuations (Fig.41). In contrast to the case for the Lorentz-type interaction (Fig.41), the intra-pocket scattering processes alone can yield a visible eigenvalue, although it is still less than 0.1.

While the superconductivity does not occur, we show the momentum dependence of the pairing gap in Fig.48 (a). Compared with the results for the Lorentz-type spin fluctuations [Fig.42 (a)], the pairing gap acquires a slightly larger anisotropy, although the symmetry is still $s_{\pm}$-wave: the gap modulation is as large as 10% on FS1 and 40% on the electron pockets (FS3 and FS4), while the gap is almost isotropic on FS2.

The momentum dependence of the renormalization function is shown in Fig.49 (a) and it is almost the same as that due to the Lorentz-type spin fluctuations [see Fig.43 (a)] except that the amplitude of the modulation is slightly enhanced.

Figure 50 (a) is a phase diagram for the $J_1 - J_2$-type spin fluctuations, where contour lines of the eigenvalues are drawn and superconduting instability does not occur even close to the SDW phase by the $J_1 - J_2$-type spin fluctuations. Compared with the phase diagram for the Lorentz-type spin fluctuations [Fig.44 (a)], the eigenvalues become smaller. This mainly comes from the stronger effect of the self-restraint of the superconducting instability due to intra-pocket scattering processes [Fig.47 (a)].

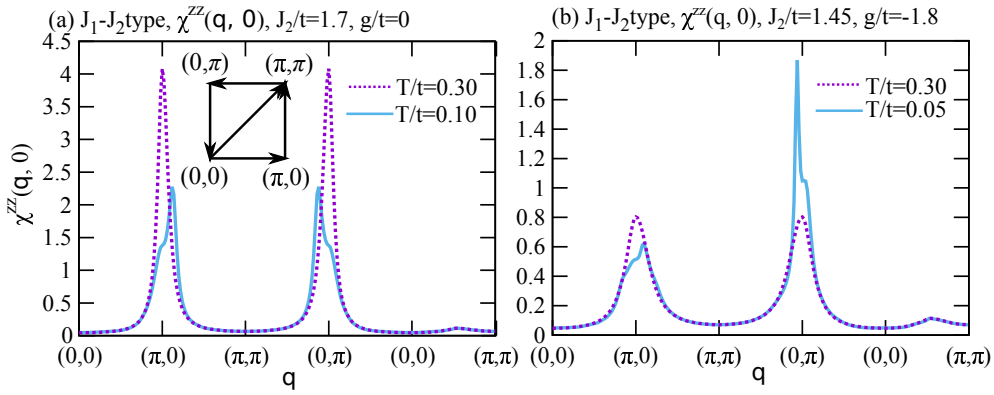

Figure 46: The static spin susceptibility $\chi^{zz}(\mathbf{q}, 0)$ as a function of $\mathbf{q}$ for the $J_1 - J_2$-type spin interaction for several choices of temperature (a) in the absence of the nematic order ($g/t = 0$) and (b) in the presence of the nematic order at low temperature ($g/t = -1.8$) along the line illustrated in the inset.

Impact of the orbital nematic order

To study the effect of the orbital nematic order, we introduce the orbital nematic interaction and take $g/t = -1.8$ [Eq.(19)]: orbital nematic fluctuations, however, are still switched off and only spin fluctuations are considered. For $g/t = -1.8$, orbital nematic order is stabilized below $T_{\rm ON} = 0.10t$ and the nematic order parameter n_- is computed self-consistently [see Fig.12]. Results obtained in the nematic phase is presented in the right panel in Figs.45-50.

The magnetic phase diagram in the plane of the strength of the spin interaction J_2/t and temperature T is shown in Fig.45 (b). The shape of the phase boundary is similar to the result in the tetragonal phase [Fig.45 (a)]. The scale of J_2/t, however, becomes smaller. These features are also recognized for the Lorentz-type spin interaction [Fig.39 (b)]. Figure 46 (b) is the momentum dependence of the static magnetic susceptibility $\chi^{zz}(\mathbf{q}, 0)$. A peak near $\mathbf{q} = (\pi, 0)$ and $(0, \pi)$ at $T = 0.30t$ becomes asymmetric below $T_{\rm ON} \simeq 0.10t$ because of the development of the nematic order n_-. The resulting $\chi^{zz}(\mathbf{q}, 0)$ shows a higher peak at $\mathbf{q} \simeq (0, \pi)$ as shown in Fig.46 (b). These features as well as the line shape of $\chi^{zz}(\mathbf{q}, 0)$ in the nematic phase are very similar to those for the Lorentz-type spin interaction [Fig.40 (b)].

The temperature dependence of the eigenvalues of the Eliashberg equations is shown in Fig.47 (b). The results are essentially the same as those in the tetragonal phase [Fig.47 (a)] and there occurs the substantial self-restraint effect of the superconducting instability due to intra-pocket scattering processes. That is, the superconducting instability is difficult also in the nematic phase by $J_1 - J_2$-type spin fluctuations.

While the superconducting instability does not occur, we plot the momentum dependence of the pairing gap at $T/t = 0.03$ in Fig.48 (b). The pairing gap acquires a large anisotropy especially on FS1 and FS4 whereas the gap becomes very small on FS3. These

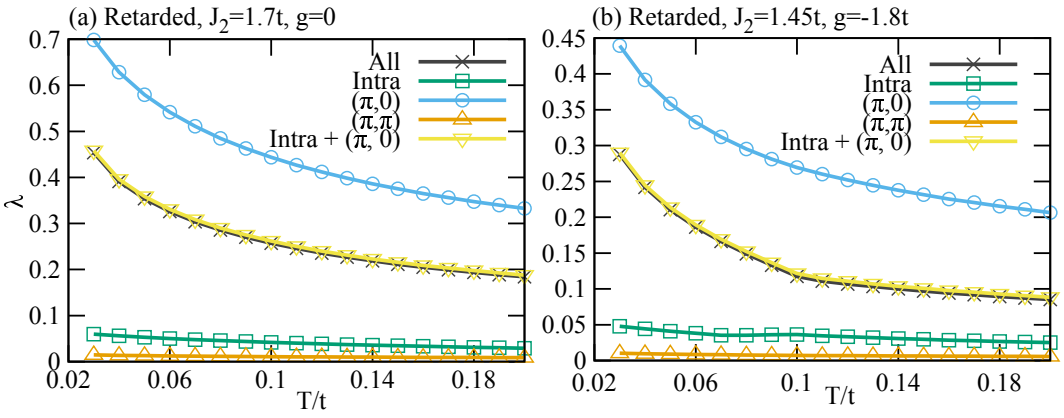

Figure 47: Temperature dependence of the eigenvalues of the Eliashberg equations for the $J_1 - J_2$-type spin fluctuations (a) in the tetragonal phase ($J_2/t = 1.7, g = 0$) and (b) in the nematic phase ($J_2/t = 1.45, g/t = -1.8$). See the caption in Fig.33 for the legend "All", "Intra", "$(\pi, 0)$", and "(π, π)".

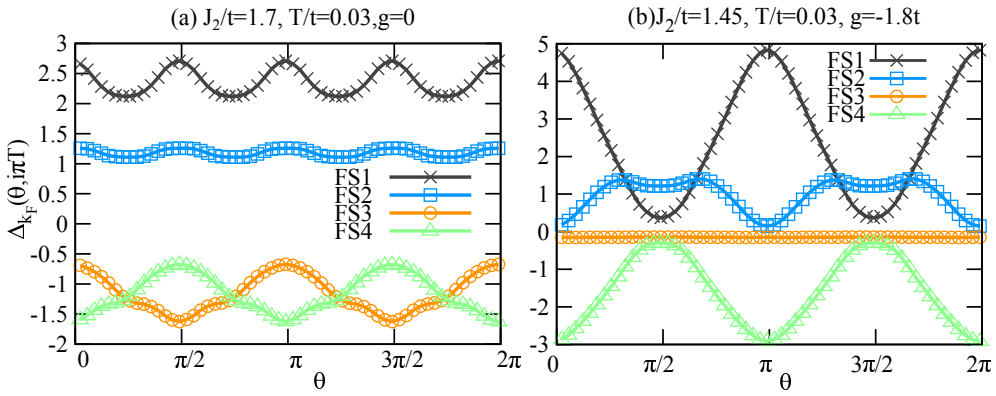

Figure 48: Momentum dependence of the pairing gap for the $J_1 - J_2$-type spin fluctuations at the low temperature (a) in the tetragonal phase ($J_2/t = 1.7, g/t = 0$) and (b) in the nematic phase ($J_2/t = 1.45, g/t = -1.8$).

results are very similar to those for the Lorentz-type spin fluctuations [Fig.42 (b)]. The momentum dependence of the renormalization function [Fig.49 (b)] is also very similar to the results due to the Lorentz-type spin fluctuations except for the absolute value of Z [Fig.43 (b)].

We summarize the eigenvalues of the Eliashberg equations for the $J_1 - J_2$-type spin fluctuations inside the nematic phase in Fig.50 (b). While the eigenvalues tend to be enhanced rapidly in the vicinity of the SDW phase, the eigenvalue is well below unity and the superconducting instability does not occur by the $J_1 - J_2$-type spin fluctuations.

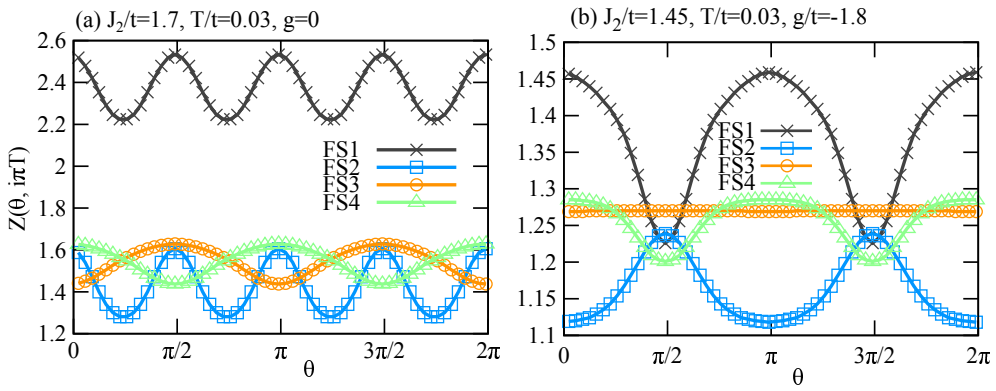

Figure 49: Momentum dependence of the renormalization function at the low temperature (a) in the tetragonal phase ($g/t = 0, J_2/t = 1.7$) and (b) in the nematic phase ($g/t = -1.8, J_2/t = 1.45$).

3.2.3 Summary of superconductivity from spin fluctuations

As is well known, spin fluctuations around $\mathbf{q} = (\pi, 0)$ develop due to the Fermi-surface nesting between the hole and electron pockets and tends to drive $s_{\pm}$-superconductivity. However, the superconducting instability does not occur because of the self-energy effect of superconductivity and also of the self-restraint effect due to apprarently weak intra-pocket scattering of spin fluctuations.

In spite of the absence of superconductivity, we can study the momentum dependence of possible pairing gap. In the tetragonal phase, the pairing gap is almost isotropic on the hole pockets (FS1 and FS2) and moderately anisotropic on the electron pockets (FS3 and FS4) [Figs.42 (a) and 48 (a)]. The anisotropy on the electron pockets is enhanced for the $J_1 - J_2$-type spin fluctuations more than the Lorentz-type spin fluctuations. In the nematic phase, the pairing gap acquires a large anisotropy on FS1 and FS4 and a moderate anisotropy on FS2; the gap on FS3 becomes very small in the nematic phase. The obtained modulation on FS1 and FS2 can be understood in terms of the orbital component. In the nematic phase, the energy of the d_{xz}-orbital becomes lower than that of the d_{yz}-orbital. As a result, the pairing gap is enhanced (suppressed) around regions on the FS where the d_{xz} (d_{yz})-orbital is dominant. This mechanism is the same as the large modulation of the pairing gap due to orbital nematic fluctuations inside the nematic phase (see Fig.35). Given that FS3 consists mainly of the d_{yz}-orbital and FS3 almost vanishes, the small gap on FS3 may be reasonable. The reason why the pairing gap on FS4 acquires the large anisotropy is not understood straightforwardly in terms of the orbital components.

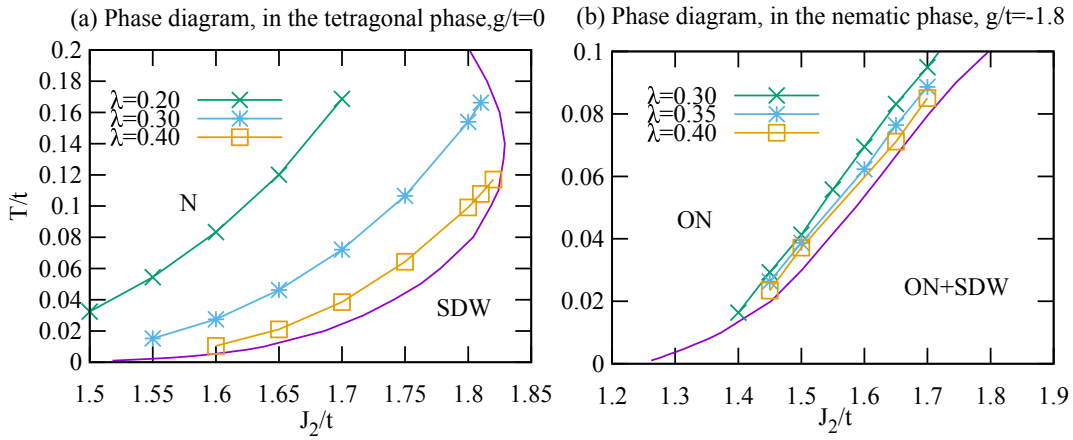

Figure 50: Phase diagram of for the $J_1 - J_2$-type spin interaction in the plane of the interaction strength J_2/t and temperature T/t (a) in the tetragonal phase ($g/t = 0$) and (b) in the nematic phase ($g/t = -1.8$). Since superconductivity does not occur, contour lines of the maximum eigenvalues of the Eliashberg equations are drawn.

3.3 Superconductivity from both orbital nematic and spin fluctuations

We have shown the superconductivity driven by orbital nematic fluctuations alone and spin fluctuations alone in Section 3.1 and Section 3.2, respectively. In this section, we study the superconductivity in the presence of both orbital nematic and spin fluctuations. Since spin fluctuations are modeled for the Lorentz-type [Eq.(36)] and the $J_1 - J_2$-type [Eq.(40)] interaction, we present our results seperately for each case.

3.3.1 Orbital nematic and Lorentz-type spin fluctuations

We solve the Eliashberg equations [Eqs.(155) and (156)] by including both orbital nematic fluctutations [Eq.(141)] and Lorentz-type spin fluctuations [Eqs.(36), (143) and (145)]. Figure 51 (a) is the temperature dependence of the eigenvalues of the Eliashberg equations in the tetragonal phase. A comparison with the purely orbital nematic case (Fig.33) shows that the temperature dependence of the eigenvalues does not change essentially by including spin fluctuations in the sense that the superconductivity is driven mainly by the intra-pocket scattering processes due to orbital nematic fluctuations. The effect of spin fluctuations is twofold. First, the eigenvalue "All" is slightly lower than the eigenvalue "Intra", which is the opposite to the case of the purely orbital nematic fluctuations. That is, spin fluctuations suppress the tendency of superconducting instability. Second, the eigenvalue "All" crosses unity at $T_c/t = 0.021$ where superconducting instability occurs. While we take the same strength of orbital nematic fluctuations ($g/t = -1.7$) as Fig.33, T_c is substantially suppressed by spin fluctuations.

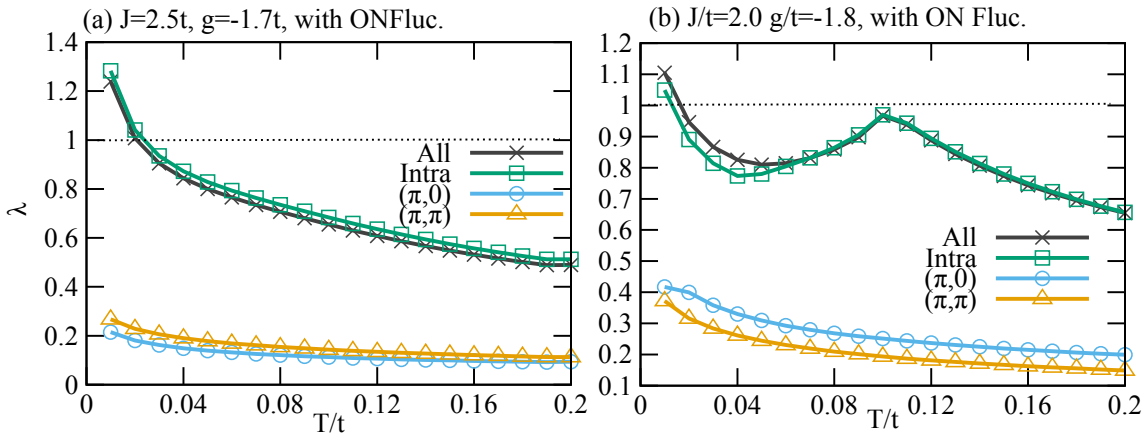

Figure 51: Temperature dependence of the eigenvalues of the Eliashberg equations due to both orbital nematic and Lorentz-type spin fluctuations (a) in the tetragonal phase ($J/t = 2.5, g/t = -1.7$) and (b) in the nematic phase ($J/t = 2.0, g/t = -1.8$). The eigenvalues are also computed by selecting specific scattering processes, "Intra", "$(\pi, 0)$" and "(π, π)"; see Fig.33.

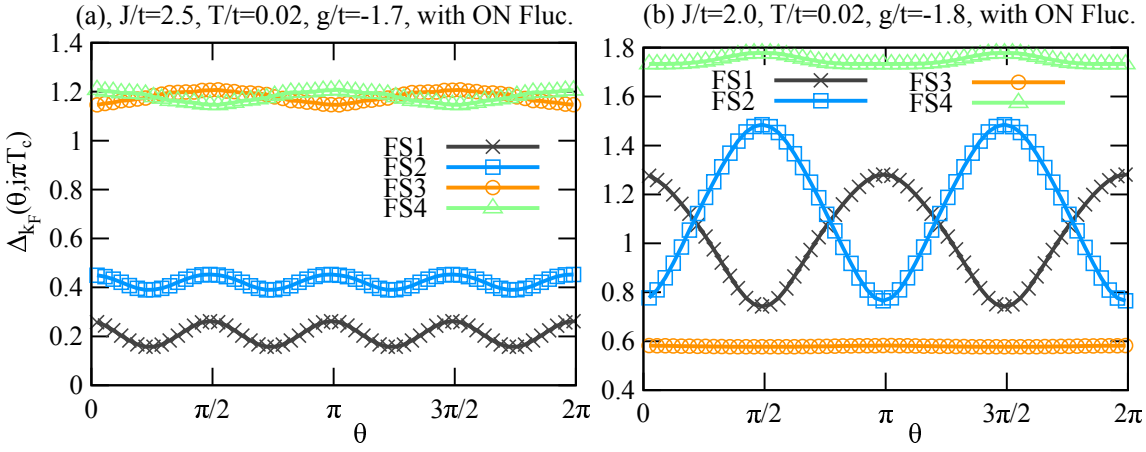

Figure 52: Momentum dependence of the pairing gap at $T = T_c$ in the presence of both orbital nematic and Lorentz-type spin fluctuations (a) in the tetragonal phase ($J/t = 2.5, g/t = -1.7$) and (b) in the nematic phase ($J/t = 2.0, g/t = -1.8$).

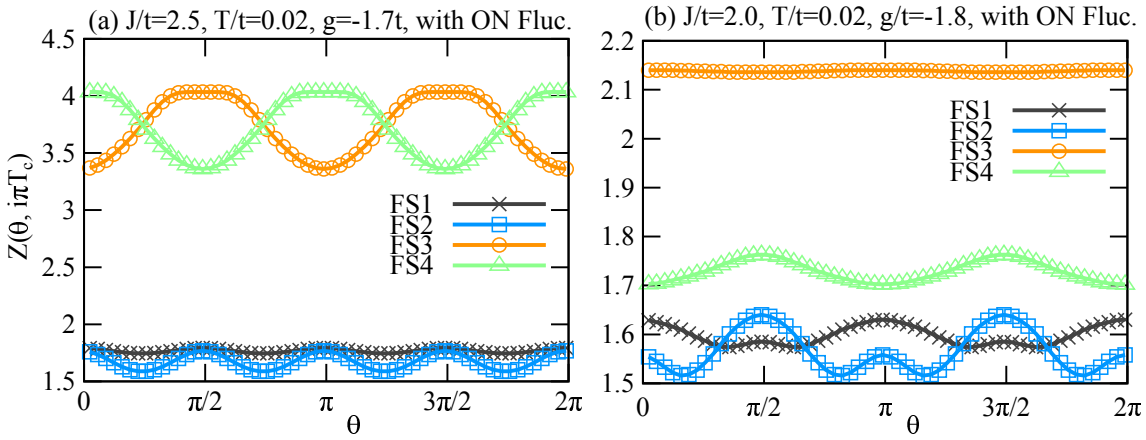

Figure 53: Momentum dependence of the renormalization function at $T = T_c$ in the presence of both orbital nematic and Lorentz-type spin fluctuations (a) in the tetragonal phase ($J/t = 2.5, g/t = -1.7$) and (b) in the nematic phase ($J/t = 2.0, g/t = -1.8$).

The momentum dependence of the pairing gap at T_c is shown in Fig.52 (a). The pairing gap is almost isotropic with s_{++}-wave symmetry and shares similar features as the purely orbital nematic fluctuations [Fig.31 (a)]. Figure 53 (a) shows the momentum dependence of the renormalization function, which is also similar to that due to orbital nematic fluctuations alone (see Fig.32), although values of Z become slightly larger. Hence obtained results [Figs.52 (a) and 53 (a)] implies that the effect of orbital nematic fluctuations is dominant over spin fluctuations, although the strength of the spin interaction is sizable ($J/t = 2.5$).

We summarize obtained T_c in Fig.54 (a) as a function of J. At $J/t = 0$, no spin fluctuations are present and T_c there is obtained from purely orbital nematic fluctuations. With increasing J, spin fluctuations develop and start to suppress the superconductivity. The gap symmetry is s_{++}-wave [Fig.52 (a)] at least up to $J/t = 2.5$. Very close to the SDW phase ($3.0 \leq J/t \leq 3.2$), the gap structure changes to $s_{\pm}$-wave symmetry and its momentum dependence is shown in Fig.55. Except for the sign of the gap on the electron pockets (FS3 and FS4), the gap structure on the electron pockets is similar to Fig.52 (a). For the hole pockets, the gap on FS1 becomes larger than that on FS2 in Fig.55. This is a typical feature of the gap from spin fluctuations [see Fig.42 (a)]. Figure 54 (a) clearly shows that spin fluctuations suppress the superconductivity from orbital nematic fluctuations and no enhancement of T_c is obtained even in the vicinity of the SDW phase.

Impact of the orbital nematic order

To study the impact of the nematic order on Figs.51 (a) - 54 (a), we next take $g/t = -1.8$ and present corresponding results in the right panel in Figs.51-54. For $g/t = -1.8$, the nematic order develops below $T_{\rm ON} \simeq 0.10t$, as seen in a cusp structure of the tempera-

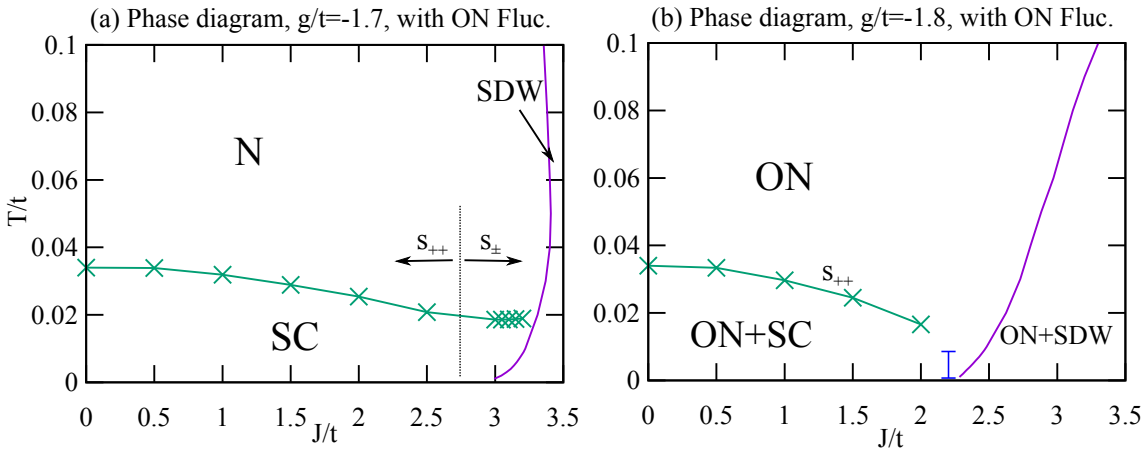

Figure 54: Phase diagram in the presence of both orbital nematic and Lorentz-type spin fluctuations. The strength of orbital nematic fluctuations is controlled by a value of g and the system is in the tetragonal phase for $g/t = -1.7$ (a) and in the nematic phase below $T_{\rm ON} \simeq 0.10t$ for $g/t = -1.8$ (b). On the other hand, the strength of spin fluctuations is controlled by the horizontal axis J/t and the SDW pahse is realized for a larger J. Possible T_c at $J/t = 2.2$ in (b) is less than $T = 0.01$ as denoted by a bar.

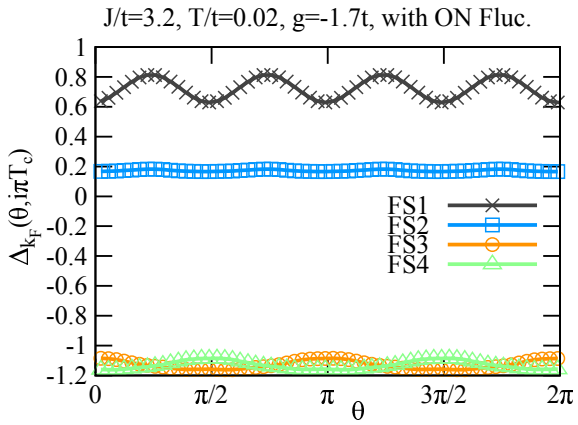

Figure 55: Momentum dependence of the pairing gap at $T = T_c$ in the presence of both orbital nematic and Lorentz-type spin fluctuations in the tetragonal phase ($J/t = 3.2, g/t = -1.7$).

ture dependence of the eigenvalues at $T/t \simeq 0.10$ in Fig.51 (b). This feature is already explained in the context of Fig.34. In contrast to the case in the tetragonal phase [Fig.51 (a)], the eigenvalue "All" is slightly larger than that of "Intra". This feature is typical to the superconductivity from purely orbital nematic phase (Fig.37). The eigenvalue "All" crosses unity at $T/t = 0.017$, where superconductivity occurs. Compared with Fig.34, the value of T_c is suppressed nearly by half due to spin fluctuations. The momentum dependences of the pairing gap [Fig.52 (b)] and of the renormalization function [Fig.53 (b)] are very similar to those for purely orbital nematic fluctuations (Figs.35 and 36). They are well characterized by the effect of orbital nematic fluctuations: the gap has a large (small) anisotropy on the hole (electron) pockets whereas the renormalization function does not acquire a large anisotropy on all Fermi pockets and its value is suppressed especially on the electron pockets (FS3 and FS4) compared with the tetragonal case [Fig.53 (a)]. Obtained T_c is summarized in Fig.54 (b). Spin fluctuations inside the nematic phase suppress the superconductivity more strongly than the tetragonal case [Fig.54 (a)] and T_c becomes less than $T = 0.01t$ in the vicinity of the SDW phase. The pairing gap is characterized by s_{++}-wave symmetry in Fig.52 (b).

3.3.2 Orbital nematic and $J_1 - J_2$-type spin fluctuations

We now summarize corresponding results for J_1-J_2-type spin fluctuations [Eqs.(141), (143), and (145)]. Figures 56 (a) and (b) show the temperature dependence of the eigenvalue of the Eliashberg equations and should be compared with Figs.51 (a) and (b), respectively. Essentially the same results are obtained for both Lorentz- and $J_1 - J_2$-type spin fluctuations. The momentum dependence of the pairing gap is presented in Figs.56 (c) and (d), which are essentially the same as Figs.52 (a) and (b), respectively. In Fig.56 (d), data on FS3 are not shown, because T_c ($= 0.013t$) becomes lower than the case of Fig.52 (b) and the resulting nematic order becomes larger, which eliminates FS3. The momentum dependence of the renormalization function are shown in Figs.56 (e) and (f). While the modulation of Z on FS1 and FS2 in the nematic phase [Fig.56 (f)] is enhanced more than the Lorentz-type spin fluctuations [Fig.53 (b)], we obtain no qualitative differences between the $J_1 - J_2$-type and Lorentz-type spin fluctuations in both tetragonal and nematic phase.

Obtained T_c is summarized as a function of the strength of the $J_1 - J_2$-type spin fluctuations in Figs.57 (a) and (b) in the tetragonal and the nematic phase, respectively. A comparison with Figs.54 (a) and (b) reveals the opposite curvature of the T_c line, indicating that the $J_1 - J_2$-type spin fluctuations suppress the superconductivity from orbital nematic fluctuations more strongly than the Lorentz-type spin fluctuations. Moreover, in the tetragonal phase very close to the SDW phase, the symmetry of the pairing gap changes to "hole-$s_{\pm}$-wave", where the pairing gap on the hole pockets (FS1 and FS2) has the opposite sign as shown in Fig.58. This solution may be interpreted as an intermediate state between s_{++}-wave and $s_{\pm}$-wave superconductivity.

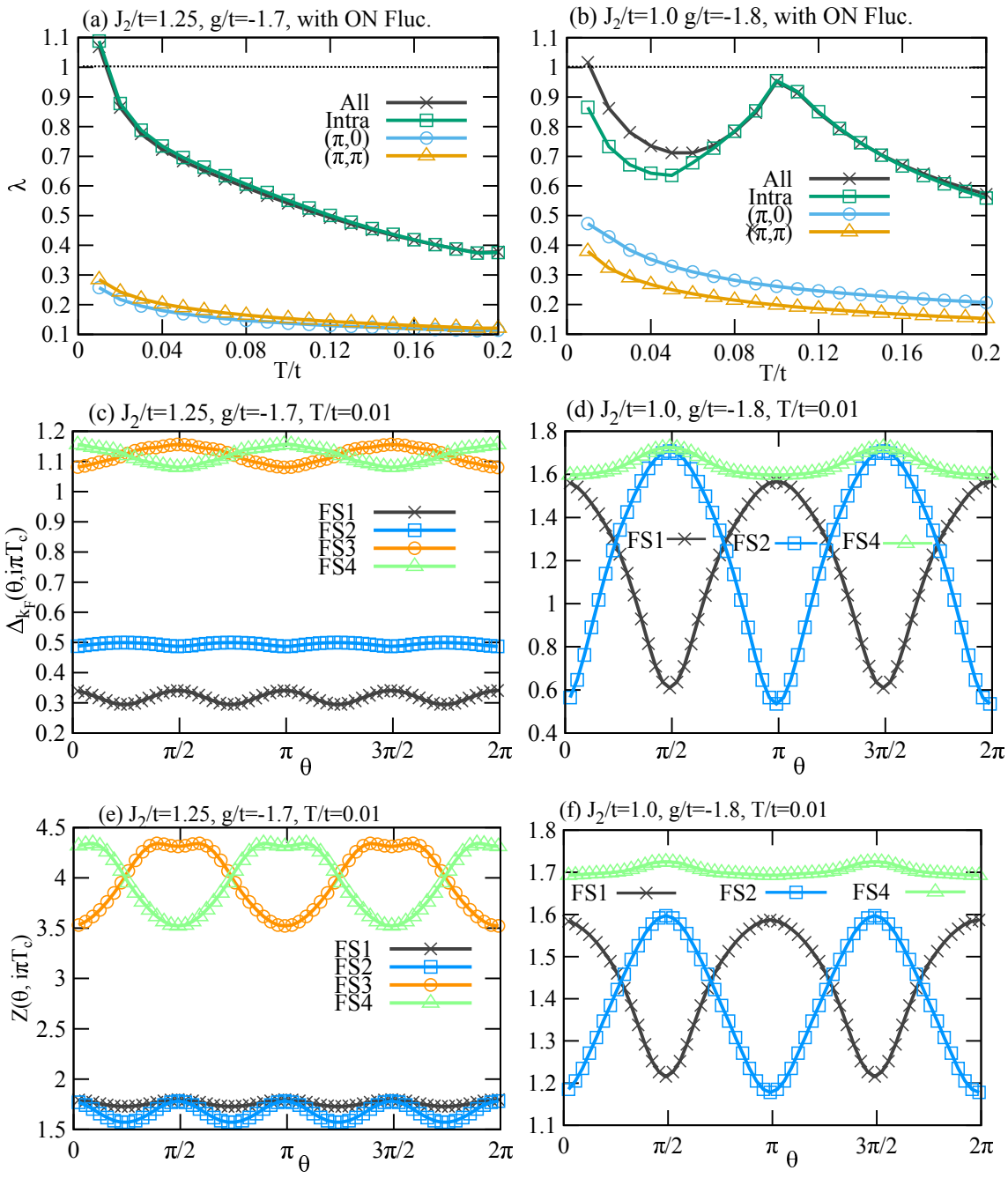

Figure 56: (a) Temperature dependence of the eigenvalues of the Eliashberg equations in the presence of both orbital nematic ($g/t = -1.7$) and $J_1 - J_2$-type spin fluctuations ($J_2/t = 1.25$). (c) and (e) The momentum dependence of the pairing gap and the renormalization function at $T = T_c$, respectively. The right-hand panels [(b), (d), and (f)] are the corresponding results for $g/t = -1.8$ and $J_2/t = 1.0$ where the nematic phase is stabilized below $T_{\rm ON} \simeq 0.10t$.

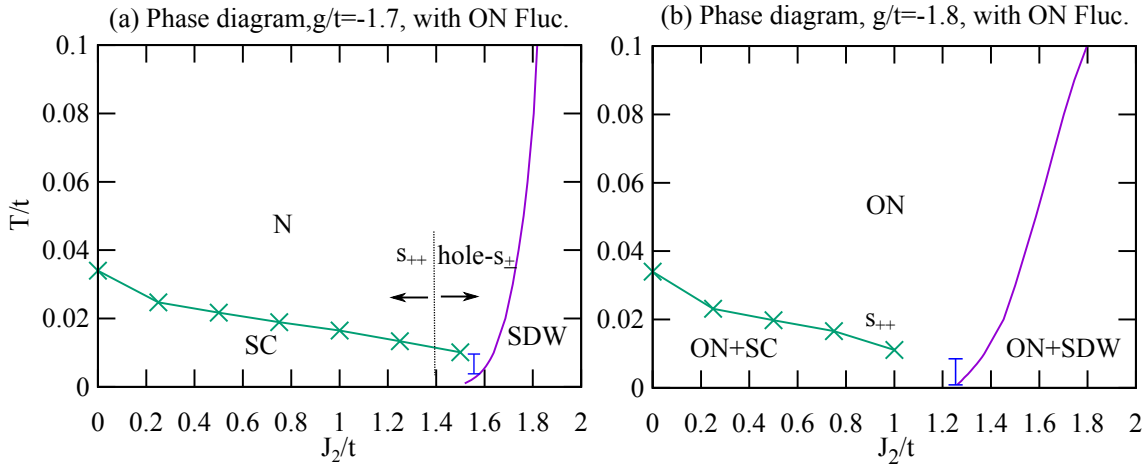

Figure 57: Phase diagram in the presence of both the orbital nematic and $J_1 - J_2$-type spin fluctuations (a) in the tetragonal phase ($g/t = -1.7$) and (b) in the nematic phase ($g/t = -1.8$). The orbital nematic fluctuations are controlled by the value of g/t and the nematic phase is stabilized below $T_{\rm ON} \simeq 0.1t$ for $g/t = -1.8$ whereas the tetragonal phase is stable down to $T = 0$ for $g/t = -1.7$. The spin fluctuations become stronger with increasing the value of J_2/t and the SDW phase is stabilized for a larger J_2. Although the bare spin interaction $J_{12}(\mathbf{q})$ does not have a peak around $\mathbf{q} = (\pi, 0)$ for $J_2/t \leq 0.5$, the peak position shifts to $\mathbf{q} = (\pi, 0)$ for $J_2/t \geq 0.5$. The onset temperature of superconductivity is less than $T/t = 0.01$ at $J_2/t = 1.25$ in (b) as denoted by a bar.

3.4 Superconductivity from instantaneous spin interaction

We have found that orbital nematic fluctuations are indispensable to the superconductivity through the analyses in Section 3.1, 3.2, and Section 3.3. Is there no chance that spin fluctuations drive the superconductivity? One option would be to discard the self-energy effect, which can actually lead to the superconductivity as shown in Appendix (Section 5.2.2). However, given that the self-energy effect turns out important in the sense that it can fully suppress the superconductivity from spin fluctuations, it is not reasonable to discard the self-energy. A more reasonable idea is to invoke the instantaneous spin interaction $\tilde{J}_{\rm Ins}(\mathbf{q})$ [Eq.(101)]. Note that the instantaneous interaction is not spin fluctuations. In this section, we clarify a role of the instantaneous spin interaction $\tilde{J}_{\rm Ins}(\mathbf{q})$ for both Lorentz-type [Eq.(36)] and $J_1 - J_2$-type [Eq.(40)] spin interaction.

We first focus on the tetragonal phase (i.e. $g/t = 0$) and compare results for the Lorentz-type and $J_1 - J_2$-type spin interaction. Figure 59 (a) is the eigenvalue of the Eliashberg equations as a function of T for the Lorentz-type spin interaction in three different pairing interactions: Only retardation term [Eq.(102)], only instantaneous term [Eq.(101)], and both terms ("Full"). The eigenvalue for the instantaneous term is much

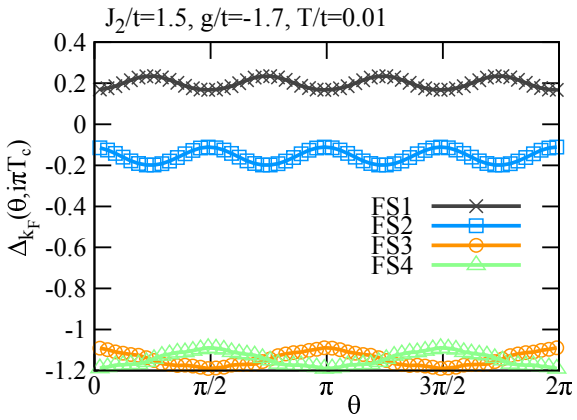

Figure 58: Momentum dependence of the pairing gap at $T = T_c$ in the presence of both orbital nematic and $J_1 - J_2$-type spin fluctuations in the tetragonal phase ($J_2/t = 1.5, g/t = -1.7$). The hole pockets (FS1 and FS2) have the opposite sign. In this sense, the gap symmetry may be referred to as "hole-$s_{\pm}$-wave".

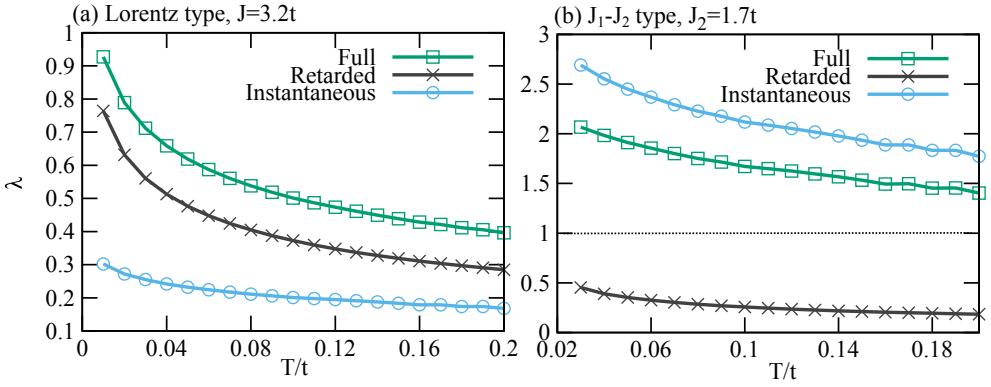

Figure 59: Temperature dependence of the eigenvalues of the Eliashberg equations for (a) the Lorentz-type and (b) the $J_1 - J_2$ type spin interaction in the tetragonal phase.

smaller than that for the retardation term, and "Full" eigenvalue is enhanced, indicating that both instantaneous and retarded term work cooperatively for superconductivity. However, the eigenvalue does not exceed unity and thus superconducting instability does not occur even if the instantaneous term is included. Corresponding results for the $J_1 - J_2$-type spin interaction are shown in Fig.59 (b). The eigenvalue of the instantaneous term already exceeds unity and can easily drive superconductivity. In contrast to the Lorentz-type spin interaction, the retardation term competes with the instantaneous part and the eigenvalue and the eigenvalue "Full" becomes smaller than the eigenvalue obtained for purely the instantaneous interaction. A comparison between Figs.59 (a) and (b) implies that the functional form of the instantaneous term is crucially important to the superconductivity.

To get more insight into the superconducting mechanism due to the instantaneous

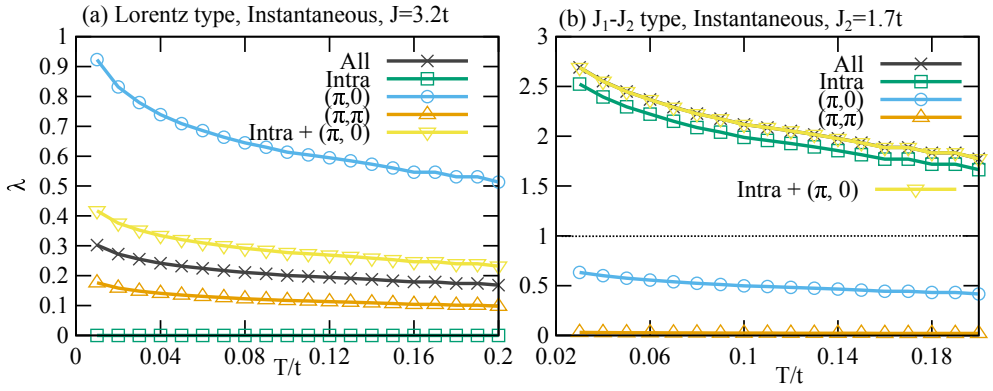

Figure 60: Temperature dependence of the eigenvalues for the instantaneous spin interaction. The eigenvalues are computed by choosing specific scattering processes for (a) the Lorentz-type and (b) the $J_1 - J_2$-type spin instantaneous term in the tetragonal phase. [see also Fig.33 (b)]

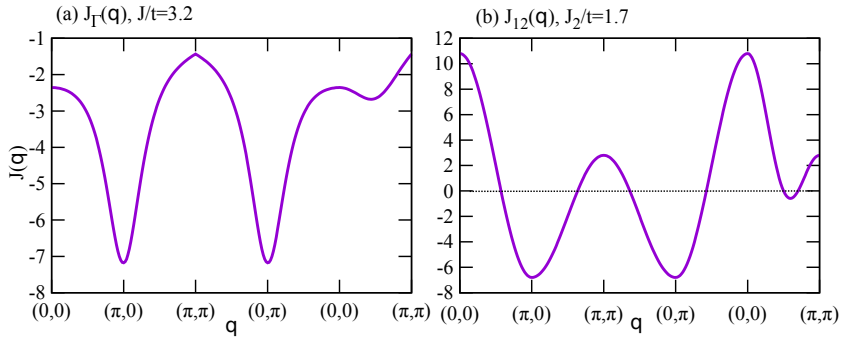

Figure 61: Momentum dependence of instantaneous spin interaction $J(\mathbf{q})$ of the Lorentz type (a) and the $J_1 - J_2$ type (b) in the tetragonal phase.

spin interaction, we focus on the instantaneous term and compute the eigenvalue as a function of T in Fig.60 by choosing specific scattering processes as we have performed in Figs.33, 37, 41, 47, 51, and 56 (a). For the Lorentz-type spin interaction [Fig.60 (a)], the eigenvalue for "$(\pi, 0)$"-scattering processes is sizable, but is strongly suppressed by the other scattering processes, especially by intra-pocket scattering processes. This strong suppression is due to the self-restraint effect discussed in Section 3.2. The corresponding results for the $J_1 - J_2$-type spin interaction are shown in Fig.60 (b), which is very different from Fig.60 (a). All scattering processes work cooperatively and the major scattering is the intra-pocket scattering, qualitatively very similar results to the case of orbital nematic fluctuations (Fig.33), although the spin interaction is considered here. The reason why the intra-pocket scattering processes are dominant for the $J_1 - J_2$-type spin interaction becomes clear by considering the functional form of $J(\mathbf{q})$. The $\mathbf{q}$ dependence of $J(\mathbf{q})$ is plotted in Fig.61. While $J(\mathbf{q})$ is negative definite for the Lorentz-type spin interaction [Fig.61 (a)], $J(\mathbf{q})$ in the $J_1 - J_2$-type spin interaction [Fig.61 (b)] changes its sign around

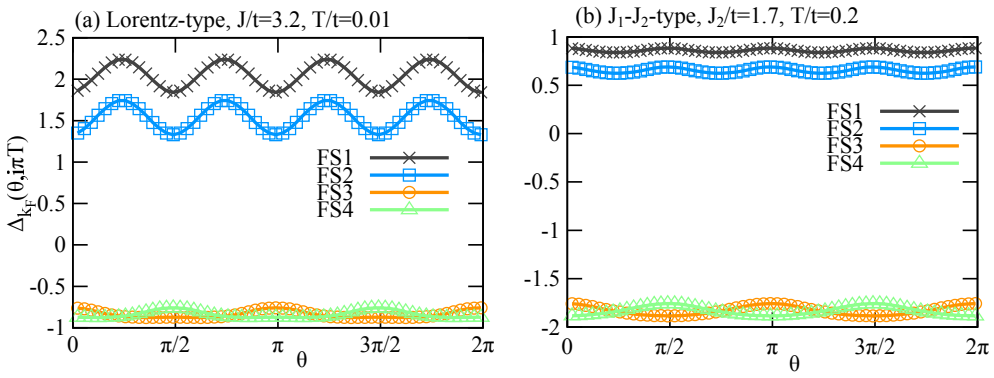

Figure 62: Momentum dependence of the pairing gap due to the instantaneous spin interaction of (a) the Lorentz type and (b) the $J_1 - J_2$ type in the tetragonal phase.

$\mathbf{q} = (3\pi/5, 0), (\pi, 3\pi/5), (3\pi/5, \pi), (0, 3\pi/5), (2\pi/5, 2\pi/5)$, and $(3\pi/5, 3\pi/5)$. The most important sign change is around $\mathbf{q} = (0, 0)$. $J(\mathbf{q})$ is now positive there and becomes very large. Given that a small momentum transfer $\mathbf{q}$ is responsible for intra-pocket scattering processes, the positive $J(\mathbf{q})$ there plays essentially the same role as orbital nematic fluctuations, leading to the isotropic gap on each Fermi surface as actually computed in Fig.62 (b). The relative phase between the electron and hole pockets is π, because $J(\mathbf{q})$ is negative around $\mathbf{q} = (\pi, 0)$ [Fig.61 (b)], leading to $s_{\pm}$-wave symmetry. Although the functional form of $J(\mathbf{q})$ is different between Figs.61 (a) and (b), the pairing gap in both cases [Figs.62 (a) and (b)] is characterized nearly isotropic $s_{\pm}$-wave symmetry, which shares the same feature as the case of spin fluctuations [Figs.42 (a) and 48 (a)].

The corresponding results in the nematic phase are summarized in Fig.63 by taking $g/t = -1.8$ where the nematic phase is stabilized below $T_{\rm ON} \simeq 0.10t$; note that associated orbital nematic fluctuations are switched off. Roles of the instantaneous term are qualitatively the same as the case in the tetragonal phase, which is clear by comparing between Figs.63 (a), (b) and Figs.59 (a), (b), Figs.63 (c), (d) and Figs.60 (a), (b), and Figs.63 (e), (f) and Figs.62 (a), (b).

Finally we provide remarks on the superconductivity driven by the instantaneous spin interaction, especially for the $J_1 - J_2$-type spin interaction [Fig.59 (b)] where the eigenvalue exceeds largely unity already at $T = 0.2t$. The absolute value of the eigenvalue for the instantaneous interaction, however, should not be taken literarly. The instantaneous term does not depend on Matsubara frequency by nature. Therefore, the sum of Matsubara frequency in the right-hand side in Eq.(156) does not converge. The resulting eigenvalue depends on the cutoff of the Matsubara sum. In Figs.59 (a) and (b), we have chosen the band width as a cutoff. Moreover, in our formalism the self-energy effect vanishes for the instantaneous term, leading to $Z_{\rm Ins} = 1$ [Eq.(155)]. Because of these two drawbacks in our formalism, we do not claim that the $J_1 - J_2$-type instantaneous spin interaction drives the superconductivity. Instead, we suggest that the instantaneous spin interaction can work positively to drive the superconductivity and the interplay with the retarded spin

interaction, namely spin fluctuations, depends on details of the functional form of $J(\mathbf{q})$.

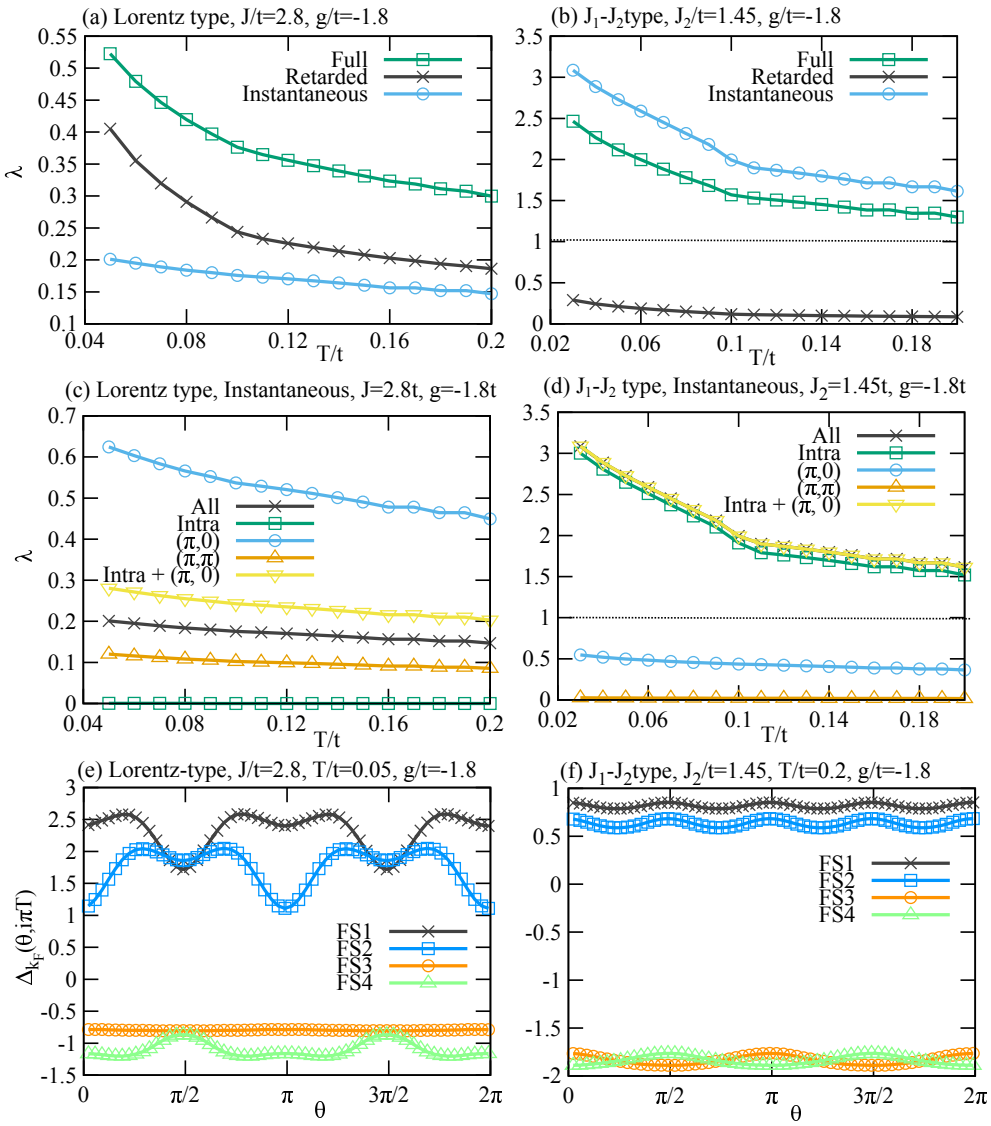

Figure 63: Temperature dependence of the eigenvalues of the Eliashberg equations in the nematic phase for (a) Lorentz-type and (b) $J_1 - J_2$-type spin interaction. Temperature dependence of the eigenvalues for the instantaneous spin interaction of (c) Lorentz-type and (d) the $J_1 - J_2$-type; the eigenvalues are computed by choosing specific scattering processes. Momentum dependence of the pairing gap for (e) Lorentz-type and (f) $J_1 - J_2$-type instantaneous spin interaction.

Chapter 4

Conclusions and Discussions

4.1 Conclusions

Previous studies showed that the orbital nematic fluctuations can drive s_{++}-wave[23, 30, 31, 32] superconductivity with transition temperature[32] comparable to experimental values in FeSCs. In this thesis, motivated by those studies we employ the Eliashberg theory and aim to establish the theory of the superconductivity driven by orbital nematic fluctuations by considering the following three, which are not handled on an equal footing in the literature: i) the momentum dependence of the pairing gap, ii) the self-energy effect of electrons, and iii) evaluation of the onset temperature of superconductivity. Refs. [23, 30, 31] respect only i) whereas Ref. [32] considers ii) and iii).

We have found that the onset temperature T_c is almost the same as that obtained in Ref.[32] [see Figs.8 (b) and 38], even though we allow the momentum dependence of the pairing gap. The absolute value of T_c can reproduce a realistic T_c observed in FeSCs if we assume our energy units $t \simeq 150$ meV. This implies that orbital nematic fluctuations are indeed a new high-T_c mechanism. Because the orbital nematic fluctuations yield an attractive interaction of pairing, the gap symmetry is always s_{++}-wave in the sense that the pairing gaps have the same sign on all Fermi pockets. When the instability occurs in the tetragonal phase, the gap exhibits a momentum dependence with fourfold symmetry, and is almost isotropic on each Fermi pocket (Fig.31), essentially the same results as Ref. [32]. Furthermore, the second leading instability has $d_{x^2-y^2}$-wave symmetry [Fig.66 (a)] and is nearly degenerate to the first one in the tetragonal phase (Fig.30). It is interesting to point out that a similar degeneracy is also obtained in a different mechanism such as spin fluctuations[11]. On the other hand, when the instability occurs inside the nematic phase, the gap remains isotropic on the electron pockets, but acquires large anisotropy with twofold symmetry on the hole pockets (Fig.35). The quasi-degeneracy between the leading and the second leading instability is largely lifted in the nematic phase (Fig.34). We have also confirmed that superconductivity from orbital nematic fluctuations belongs to a strong-coupling regeme[32] in the sense that the renormalization function Z [Eq.(155)] becomes as large as $\simeq 3.8$ in the tetragonal phase (Fig.32) and

$\simeq 2.5$ (Fig.36) in the nematic phase. That is, the self-energy effect is crucially important to the superconductivity from orbital nematic fluctuations.

It is natural to assume that spin fluctuations are also present in FeSCs. Therefore we have studied the superconductivity from spin fluctuations in the same theoretical scheme as the superconductivity from orbital nematic fluctuations. We have considered two types of spin interactions, the Lorentz type [Eq.(36)] and the $J_1 - J_2$ type [Eq.(40)]. The former may correspond to the limit of an itinerant magnetic system in the sense that the strength of spin interaction decays exponentially in real space. The $J_1 - J_2$-type interaction is motivated by a localized spin system with superexchange interactions J_1 and J_2. Hence the $J_1 - J_2$-type spin interaction may correspond to the system where spins have a localized character.

For the Lorentz-type interaction, spin fluctuations with momentum $\mathbf{q} = (\pi, 0)$ develop by Fermi-surface nesting between the hole and electron Fermi pockets and drive $s_{\pm}$-wave superconductivity similar to other theoretical studies[15]. While spin fluctuations are enhanced around $\mathbf{q} = (\pi, 0)$, weak spin fluctuations remain for a small $\mathbf{q}$ region, which then allow intra-pocket scattering processes. Apparently such processes seem negligible and less important. However, we have found that they suppress substantially the onset of the superconductivity driven by the major spin fluctuations around $\mathbf{q} = (\pi, 0)$. That is, the spin-fluctuation mechanism contains this self-restraint effect and tend to prevent superconducting instability. The self-energy effect also suppresses superconducting instability. These two negative feedbacks do not allow superconducting instability from spin fluctuations in our theory. Although superconductivity does not occur, we have computed a possible structure of pairing gap from spin fluctuations. The gap is characterized by $s_{\pm}$-wave symmetry and almost isotropic on the hole pockets in the sense that a maximal modulation of the gap is about $\simeq 12\%$. On electron pockets, the gap modulation reaches about $\simeq 21\%$. In the nematic state, the pairing gap acquires a large anisotropy although the tendency of superconducting instability is largely suppressed compared with the case in the tetragonal phase [Figs.42 (b) and 48 (b)]. We have also checked that the structure of the pairing gap is essentially the same even if the self-energy effect is neglected (Fig.74). In the $J_1 - J_2$-type spin interaction, results are essentially the same as the Lorentz-type interaction except that the gap modulation in the tetragonal phase is enhanced and reaches $\simeq 41\%$ on the electron pockets.

Supposing a realistic situation in FeSCs, we have considered the superconductivity driven by both orbital nematic and spin fluctuations. We have found that the orbital nematic and the spin fluctuations compete with each other (Figs.54 and 57), and the onset temperature T_c is suppressed monotonically by increasing the strength of spin fluctuations. The pairing gap is characterized by almost isotropic s_{++}-wave symmetry [Figs.52 (a) and 56 (c)] in a wide region of the phase space. In the vicinity of the SDW phase, however, the gap symmetry chan change to $s_{\pm}$-wave symmetry [Fig.55]. When superconducting instability occurs in the nematic phase, on the other hand, the symmetry of the pairing

gap remains s_{++}-wave even near the SDW phase [Fig.52 (b)]. However the pairing gap acquires large anisotropy on the hole Fermi pockets, whereas it remains almost isotropic on the electron Fermi pockets [Figs.52 (b) and 56 (d)], showing that the superconductivity is well characterized by that purely from orbital nematic fluctuations (Fig.35) even in the presence of both orbital nematic and spin fluctuations.

Finally we have also explored possible routes to obtain superconductivity from spin interactions, because spin fluctuations alone cannot drive superconductivity. One route would be to neglect the self-energy effect. In this case, we actually obtain superconducting instability as shown in Fig.75 and the gap structure itself is not affected much by the self-energy. However, given that superconducting instability does not occur in the presence of the self-energy, it is not reasonable to discuss superconductivity by discarding the self-energy effect. Another route is to invoke significant contributions from the instantaneous spin interaction (not spin fluctuations). Although in our theoretical scheme the instantaneous interaction cannot be treated in a reliable way because the self-energy effect vanishes and results depend on a choice of the cut-off energy, we have found that the instantaneous interaction can drive superconductivity [Figs.59 (b) and 62 (a)]. Hence the presence of the instantaneous spin interaction contributes positively to the superconducting instability.

4.2 Connection to iron-based superconductors

We now discuss a possible connection to the superconductivity in FeSCs. Because both orbital nematic and spin fluctuations are expected in FeSCs, we mainly consider results obtained in Section 3.3. We, however, note that the gap structure is very similar to that obtained from purely orbital nematic fluctuations except for the vicinity of the SDW phase where the sign of the gap can change, with keeping the momentum dependence of the gap almost unchanged.

In the tetragonal phase, we have obtained the nearly isotropic pairing gap, which is actually observed in many FeSCs by ARPES measurements. Typical results are obtained in $Ba_{0.6}K_{0.4}Fe_2As_2$[39, 40, 41] on all Fermi pockets as shown in Fig.64. A nearly isotropic gap is also observed in other FeSCs: on all Fermi pockets in Ba $(Fe_{0.75}Ru_{0.25})_2As_2$[42], on all hole Fermi pockets in $BaFe_2$ $(As_{0.7}P_{0.3})_2$[43] and $BaFe_2$ $(As_{0.65}P_{0.35})_2$[39, 44], on a hole fermi pocket in $NdFeAsO_{0.9}F_{0.1}$[45], on both hole and electron pocket in $CaKFe_4As_4$[46], on an electron pocket in $Cs_{0.8}Fe_2Se_2$[47] and a single-layer FeSe[48], and a potassium-coated triple-layer FeSe film[49], and in various FeSe systems such as $K_{0.68}Fe_{1.79}Se_2$[50], $(Tl_{0.45}K_{0.34})Fe_{1.84}Se_2$[50], $FeTe_{0.55}Se_{0.45}$[51], $K_{0.8}Fe_2Se_2$[47],

When superconductivity occurs inside the nematic state, we have found that the pairing gap acquires a large anisotropy on the hole Fermi pockets, while it remains nearly isotropic on the electron Fermi-pockets [Figs.52 (b) and 56 (b)]. For $FeSe_{0.93}S_{0.07}$ in the nematic phase an anisotropic pairing gap was revealed on the hole Fermi pockets by

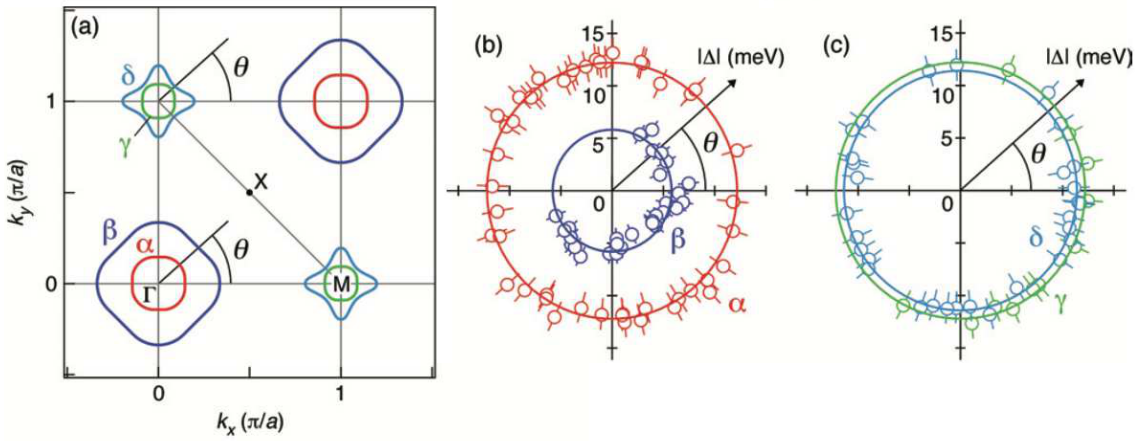

Figure 64: (a) Sketch of four Fermi pockets in the first quadrant of the Brillouin zone in $Ba_{0.6}K_{0.4}Fe_2As_2$[41]. (b) Polar plots of the pairing gap observed on the hole Fermi pockets α and β; the angle θ is measured from the k_x axis as illustrated in (a). (c) Polar plots of the pairing gap observed on the electron Fermi pockets γ and δ.

ARPES measurements as shown in Fig.65[52], which is well captured in the present work. On the other hand the pairing gap on the electron pockets in the nematic phase has not yet been detected by ARPES.

The structure of the pairing gap is considered important for identifying the mechanism of superconductivity. We have found that the gap structure due to orbital nematic fluctuations is rather similar to that due to spin fluctuations and a nearly isotropic gap is obtained on the hole pockets in the tetragonal phase. On the other hand, the pairing gap in the spin-fluctuations mechanism tends to be more anisotropic than the orbital nematic mechanism on the electron pockets. While the anisotropy can be about 40%, we need a careful treatment about this anisotropy, because we employ a unit cell containing only one iron. The unit cell in real FeSCs contains two irons. Hence our Brillouin zone are holded and two electron pockets exist around $\mathbf{k} = (\pm\pi, 0)$ and $(0, \pm\pi)$, respectively, in FeSCs [see Fig.5 (b)]. These two pockets hybridize and become inner (green) and outer (blue) electron pockets, respectively, around $\mathbf{k} = (\pi, 0)$ and $(0, \pi)$ as shown in Fig.64 (a). As a result, the gap modulation on each inner and outer electron-pocket may be reduced approximately by half, namely about 20%. Inside the nematic phase, on the other hand, we have found that the pairing gap due to only spin fluctuations acquires a large anisotropy on not only the hole Fermi pockets but also the electron Fermi pocket whereas orbital nematic fluctuations lead to the anisotropic gap only on the hole pockets. Therefore the anisotropy of the pairing gap on the electron pockets is different from orbital nematic mechanism. However, it is too early to state that this difference is crucial to distinguish the orbital nematic mechanism from the spin-fluctuation mechanism. Given that the gap structure inside the nematic phase is controlled by the occupation of d_{xz}- and d_{yz}-orbitals on the Fermi pockets, and the electron Fermi pockets in FeSCs contain

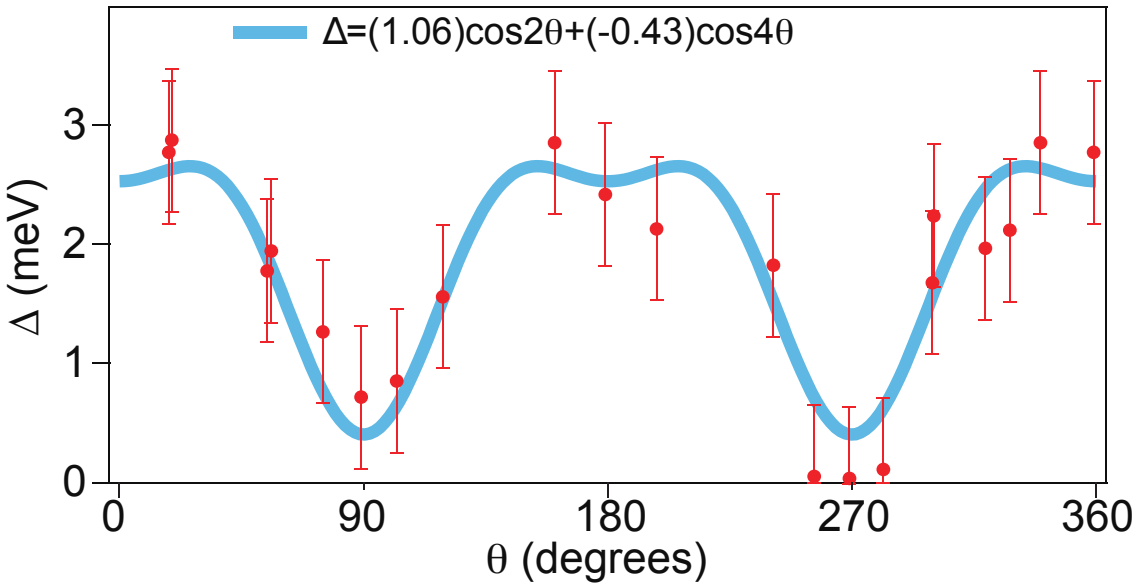

Figure 65: Pairing gap observed on a hole pocket in $FeSe_{0.93}S_{0.07}$[52] (Red filled circles). The horizontal axis θ is an angle measured by k_x axis. The blue curve is fitted line of the gap.

also a component of the d_{xy}-orbital, which is ignored in our theory. A possible anisotropy on the electron pockets is worth exploring in the future by including the d_{xy} orbital. In the tetragonal phase, the nodal gap is observed in KFe_2As_2[53, 54]. This data cannot be captured in our theory even through both orbital nematic and spin fluctuations are taken into account. This obviously suggests that our minimal two-band model should be developed, for example, by including other orbitals.

Concerning the onset temperature of superconductivity T_c, we have found that orbital nematic fluctuations can drive the superconductivity with T_c as high as T_c observed in FeSCs if we assume $t \simeq 150$meV (Fig.38), whereas it is difficult to achieve high-T_c superconductivity from spin fluctuations (Figs.44 and 50). In this sense, we consider that the orbital nematic fluctuations are more important than spin fluctuations as the mechanism of the superconductivity in FeSCs.

Chapter 5

Appendix

5.1 Supplementary results of superconductivity from orbital nematic fluctutations

5.1.1 Subleading superconducting instability in the tetragonal phase

In Figs.30 and 34 we have plotted the eigenvalue λ down to the fifth leading instability. Since we have discussed the pairing gap associated with the leading instability alone in Section 3.1, we here present the gap structure of the subleading instabilities. Figure 66 shows the pairing gap corresponding to the (a) second, (b) third, (c) fourth, and (d) fifth largest eigenvalues for $g = -1.7t$, where superconducting instability occurs in the tetragonal phase. The gap corresponding to the second largest eigenvalue is characterized by $d_{x^2-y^2}$-wave symmetry. While the gap has nodes at $\theta = \pi/4, 3\pi/4, 5\pi/4, 7\pi/4$ on the hole pockets (FS1 and FS2), there is no gap node on the electron pockets (FS3 and FS4), and the sign of the gap is positive (negative) on FS3 (FS4). This d-wave gap is also obtained for the superconductivity from spin fluctuations in some cases [15, 55]. The third largest eigenvalue [Fig.66 (b)] yields the gap with $s_{\pm}$-wave symmetry, which is very similar to the pairing gap frequency obtained from spin fluctuations (see Section 3.2). The fourth largest eigenvalue [Fig.66 (c)] corresponds to the gap of $d_{x^2-y^2}$-wave symmetry. A crucial difference between Figs.66 (a) and (c) lies in the sign of the gap on FS3 and FS4. The gap corresponding to the fifth largest eigenvalue is shown in Fig.66 (d). The gap symmetry is s_{++}-wave, the same symmetry as the leading instability (Fig.31). A major difference is that the gap becomes quite small on the electron pockets in Fig.66 (d).

5.1.2 Subleading superconducting instability in the nematic phase

Figure 67 is similar to Fig.66, but we take $g = -1.8t$, where superconductivity occurs in the nematic phase. The gap corresponding to the second largest eigenvalue [Fig.67 (a)] seems similar to Fig.66 (a), but $d_{x^2-y^2}$-symmetry cannot be defined in the nematic

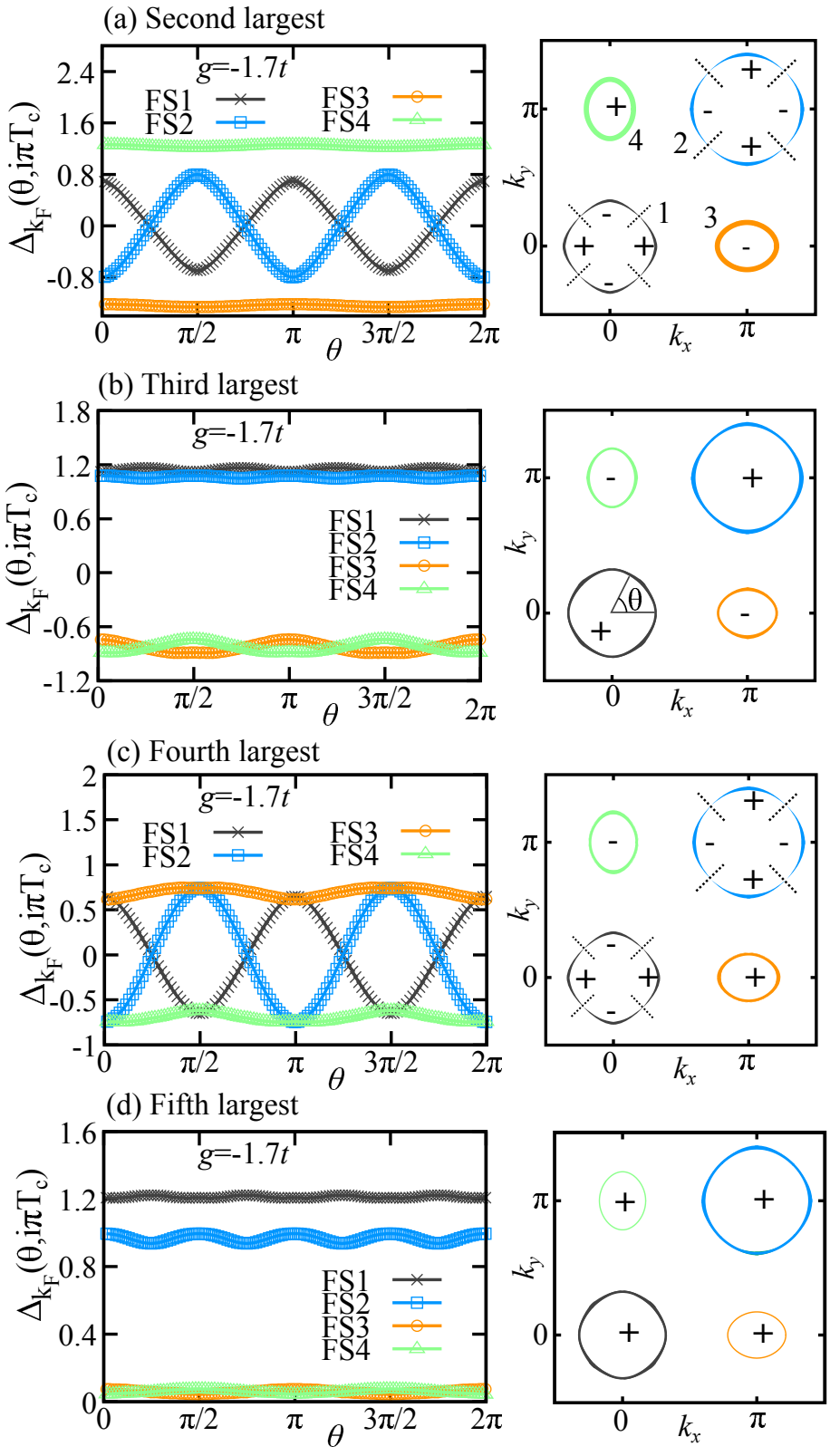

Figure 66: Momentum dependence of the pairing gap corresponding to the (a) second, (b) third, (c) fourth, and (d) fifth leading instability from orbital nematic fluctuations in the tetragonal phase ($g/t = -1.7$). The right figure in each panel is a sketch of pairing gap on each Fermi pocket where the gap magnitude is represented by the thickness of the Fermi pocket.

phase. The gap symmetry in Fig.67 (a) is characterized by nodal s-wave. Figure 67 (b) shows the gap corresponding to the third largest eigenvalue. This results shares the same $s_{\pm}$-wave symmetry with Fig.66 (b), although the gap modulation on the hole pockets is much larger and the gap becomes nearly zero at $\theta = 0, \pi$ on FS1 and at $\theta = \pi/2, 3\pi/2$ on FS2. The same $s_{\pm}$-wave symmetry is also realized in the fourth leading instability [Fig.67(c)], although the gap becomes nearly zero on the FS3. Figure 67 (d) shows the gap corresponding to the fifth largest eigenvalue. The gap structure is similar to Fig.66 (a), but the symmetry is nodal s-wave here and the gap on FS3 becomes nearly zero.

5.1.3 Superconducting instability deeply inside the nematic phase

We have shown superconducting instability in the orbital nematic phase by taking $g/t = -1.8$, where FS3 barely remains. For a larger magnitude of g, the orbital nematic order develops more and FS3 disappears. It is interesting to study superconducting instability in the absence of FS3. Here we summarize results in such a situation by taking $g/t = -1.9$ in Fig.68. The nematic order parameter n_- is computed self-consistently by solving Eq.(63). Its temperature dependence is shown in Fig.68 (a). As expected, FS3 disappears in $T \leq 0.13t$ because of a large nematic parameter [see the right panel in Fig.68 (c)]. Figure 68 (b) shows the temperature dependence of the eigenvalues of the Eliashberg equations down to the fifth leading instability. As we have already seen in Fig.34, all of the eigenvalues becomes nearly unity at the onset temperature of the nematic transition $T_{\rm ON} \simeq 0.20t$ and makes a cusp there, yielding no superconducting instability. The eigenvalues are suppressed below $T_{\rm ON}$ because orbital nematic fluctuations are suppressed by the nematic order. FS3 vanishes below $T = 0.13t$ and the eivenvalues exhibit a discontinuous change there. While the eigenvalues of the subleading instabilities remain suppressed at low temperatures, the largest eigenvalue starts to be enhanced below $T = 0.13t$ and finally crosses the unity at $T = 0.052t$ where the superconducting instability occurs. Figure 68 (c) shows the momentum dependence of the pairing gap. In spite of the absence of the FS3 the result is similar to the case of $g/t = -1.8$ (Fig.35), but the gap modulation on the hole pockets reaches as large as 60%, which is larger than the case of $g/t = -1.8$. Figure 68 (d) shows the renormalization function, which features a similar momentum dependence to that of the pairing gap [Fig.68 (b)]. Figure 68 (e) shows the eigenvalue of the Eliashberg equations for specific scattering processes and is very similar to the case of $g/t = -1.8$ (Fig.37). That is, the intra-pocket scattering processes are the major driving force of the superconducting instability even in the absence of FS3.

The momentum dependence of the pairing gap corresponding to the second, third, fourth and fifth largest eigenvalues is summarized in Figs.69 (a)-(d), respectively. The pairing gap for the second largest eigenvalues [Fig.69 (a)] has a momentum dependence similar to Fig.67 (a) except for the absence of FS3. While the gap almost vanishes at $\theta = 0, \pi$ on FS1 and $\theta = \pi/2, 3\pi/2$ on FS2, the pairing gap may be characterized by $s_{\pm}$-symmetry. The pairing gap for the third largest eivenvalues [Fig.69 (b)] has s_{++}-wave

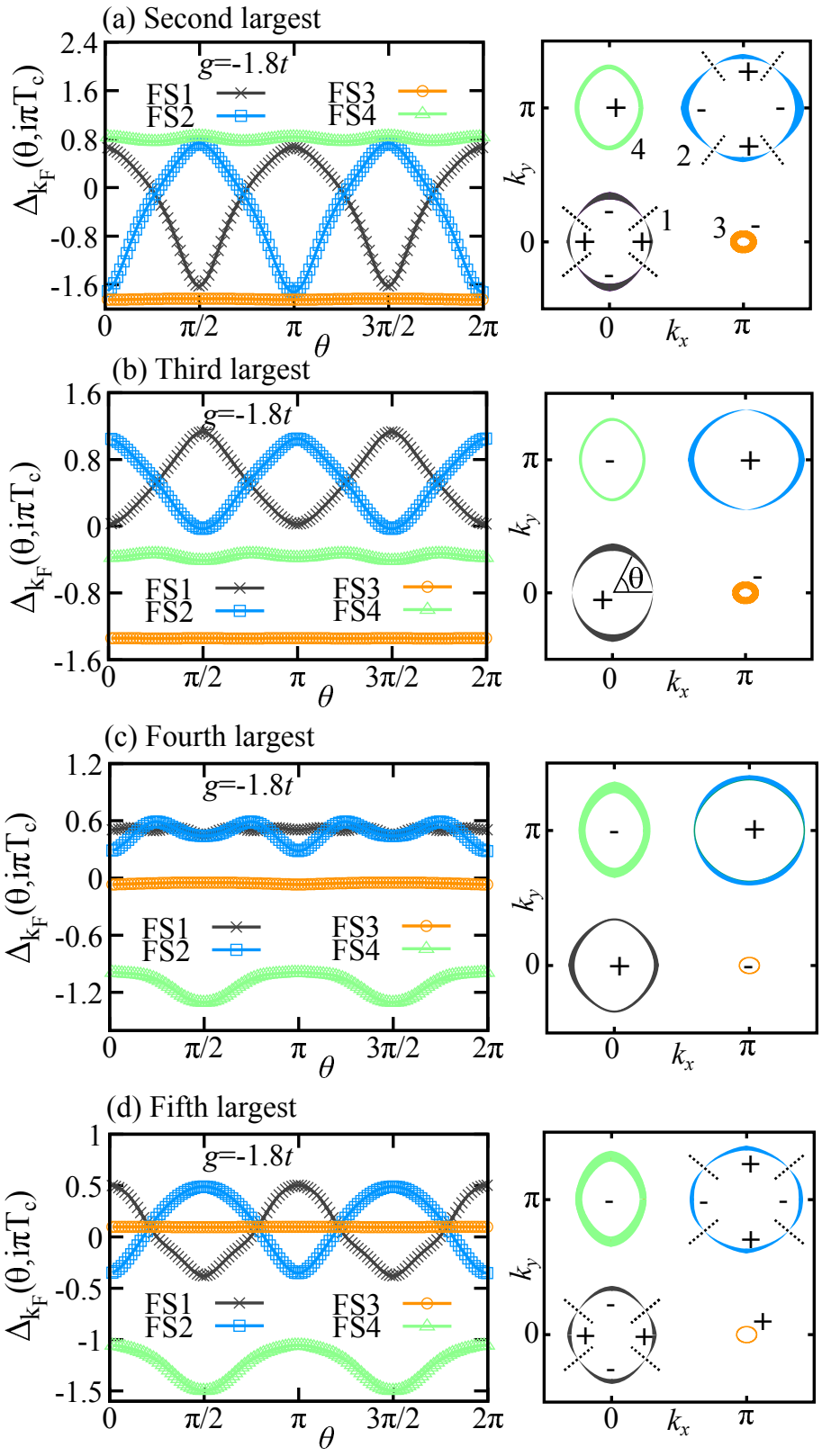

Figure 67: Momentum dependence of the pairing gap in the (a) second, (b) third, (c) fourth, and (d) fifth leading instability from orbital nematic fluctuations inside the nematic phase ($g/t = -1.8$). The right figure in each panel is a sketch of pairing gap on each Fermi pocket where the gap magnitude is represented by the thickness of the Fermi pocket.

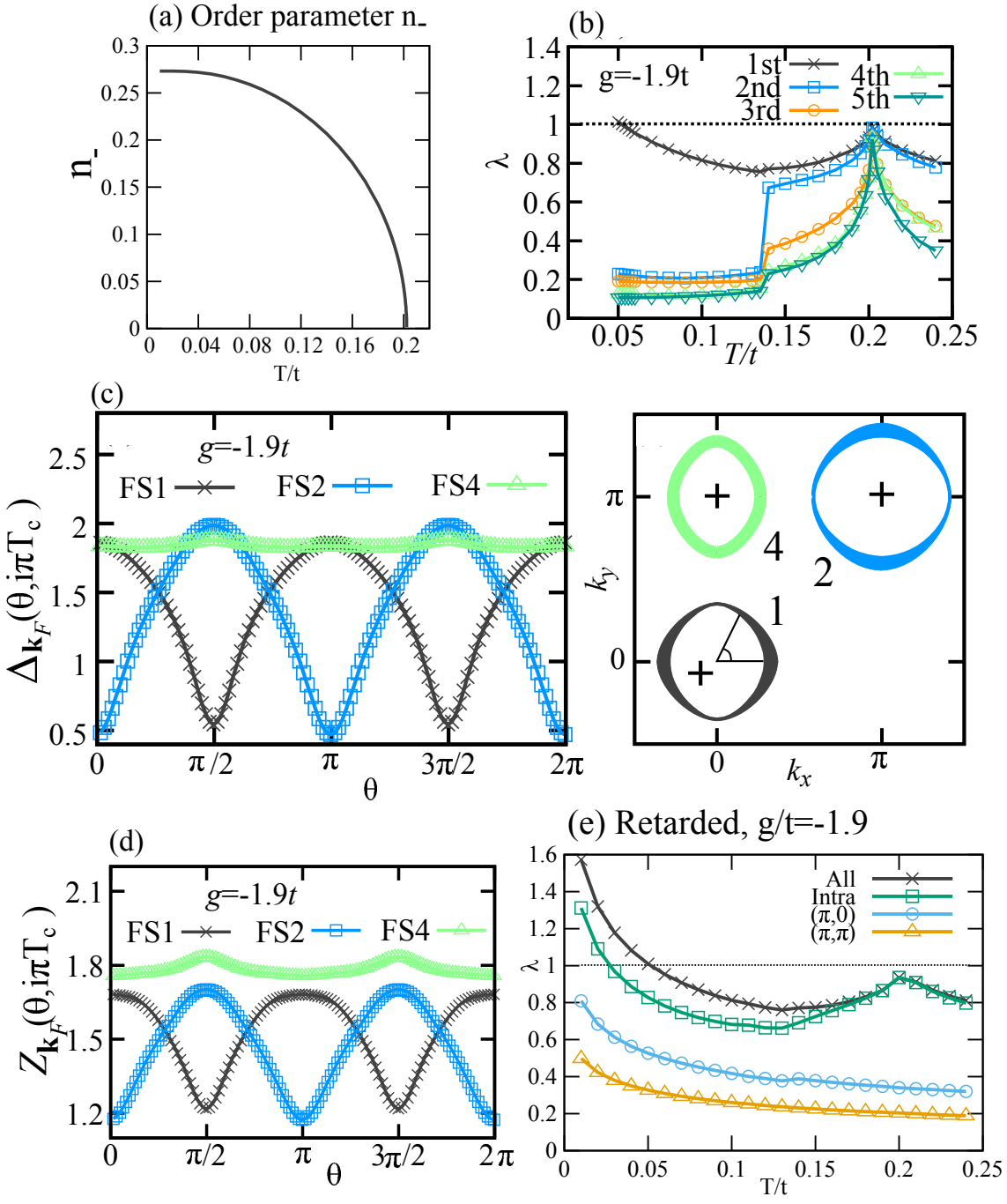

Figure 68: Superconductivity from orbital nematic fluctuations deeply inside the nematic phase ($g/t = -1.9$). (a) Temperature dependence of the nematic order parameter. (b) Temperature dependence of the five largest eigenvalues of the Eliashberg equations. (c) Momentum dependence of the pairing gap. (d) Momentum dependence of the renormalization function. (e) Temperature dependence of the largest eigenvalues of the Eliashberg equations for specific scattering processes.

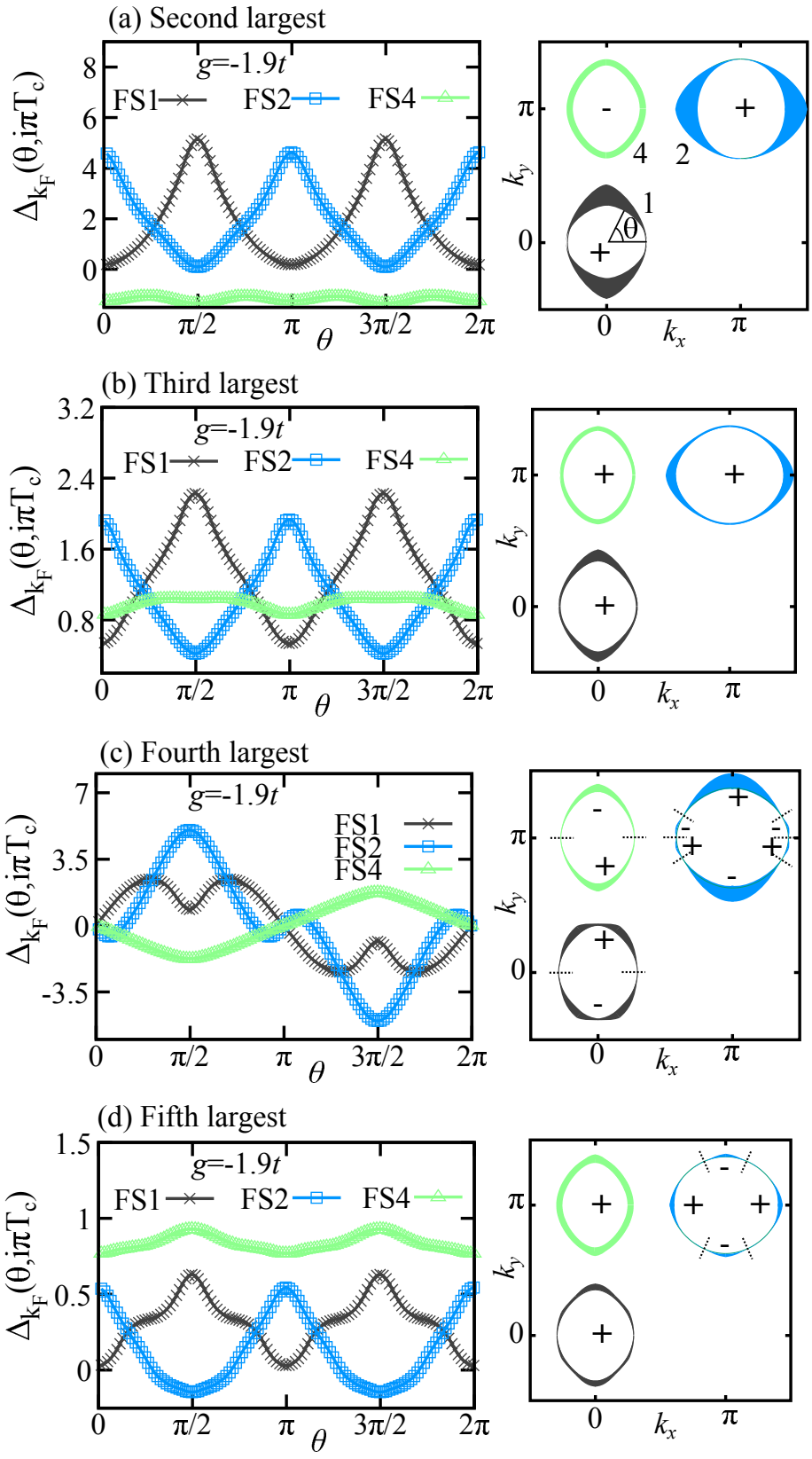

Figure 69: Momentum dependence of the pairing gap from the second to the fifth leading instability from orbital nematic fluctuations deeply inside the nematic phase ($g/t = -1.9$). The right figure in each panel is a sketch of pairing gap on each Fermi pocket where the gap magnitude is represented by the thickness of the Fermi pocket.

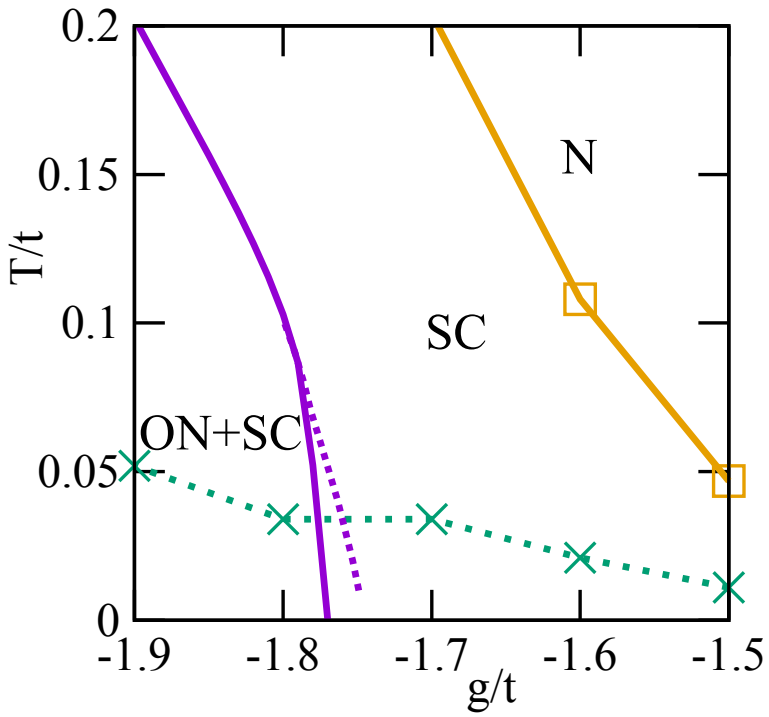

Figure 70: Onset temperature of superconductivity (orange solid line with open squares) without the self-energy effect in the plane of the strength of the orbital nematic interaction g and temperature T. The purple solid line and the purple dotted line are the same as those in Fig.38 and correspond to the phase boundary of the orbital nematic (ON) phase. For comparison, the result of T_c with the self-energy (dotted line with crosses), which is the same as T_c in Fig.38, is also plotted.

symmetry, similar to Fig.68 (b), but the position of the maximum gap shifts by $\pi/2$. Figure 69 (c) shows the pairing gap for the fourth largest eigenvalues. This gap has p-wave symmetry. It is interesting to know that in principle the orbital nematic fluctuations can drive p-wave superconductivity. In Fig. 69 (d) we show the pairing gap for the fifth largest eigenvalues. The symmetry of the gap is nodal s-wave, and the nodes appear on FS2. In addition, the gap almost vanishes at $\theta = 0, \pi$ on FS1.

5.1.4 Superconductivity from orbital nematic fluctuations without the self-energy effect

To demonstrate the importance of the self-energy effect, we study the superconductivity from orbital nematic fluctuations without the self-energy effect. Figure 70 is the phase diagram in the plane of the interaction strength g and temperature, where the phase boundary of the orbital nematic phase (ON) is the same as Fig.38 and we also add the onset temperature of superconductivity with the self-energy, namely obtained T_c in Fig.38 for comparison. The solid line is the corresponding T_c without the self-energy

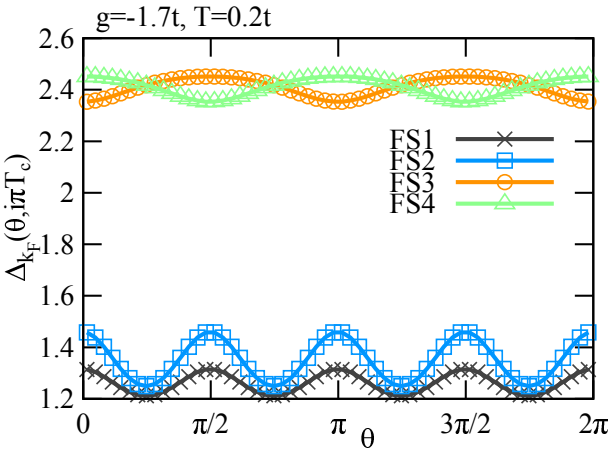

Figure 71: Momentum dependence of the pairing gap due to orbital nematic fluctuations without the self-energy effect ($g/t = -1.7$).

effect. Clearly Fig.70 shows that the self-energy effect is very important to not only the absolute value of T_c, but also the geometry of a T_c-curve near the ON phase. The pairing gap at the onset temperature of the superconductivity is shown in Fig.71. The symmetry of the pairing gap is s_{++}-wave and is almost isotropic, very similar to the results in Fig.31. Therefore the self-energy effect does not affect the structure of the pairing gap.

5.2 Supplementary results for superconductivity from spin fluctuations

5.2.1 Superconducting instability from spin fluctuations deeply inside the nematic phase

We present results of the superconductivity from spin fluctuations deeply inside the nematic phase ($g/t = -1.9$), where FS3 disappears at $T/t \simeq 0.13$ by the nematic order. Results turn out almost the same as those for $g/t = -1.8$ (Section 3.2), where FS3 still remains in the nematic phase. Nevertheless, results in the absence of FS3 may be interesting and thus we briefly present them below.

Lorentz-type spin fluctuations

Figure 72 shows (a) temperature dependence of the eigenvalues of the Eliashberg equation from the Lorentz-type spin fluctuations, (b) momentum dependence of the pairing gap, and (c) that of the renormalization function. A comparison with the case of $g/t = -1.8$, namely Figs.41 (b), 42 (b), and 43 (b) shows very similar results, implying that the effect of a change of the nematic order is minor. Differences are recognized in the following: The eigenvalues are suppressed more by the nematic order, and the absolute value of Z

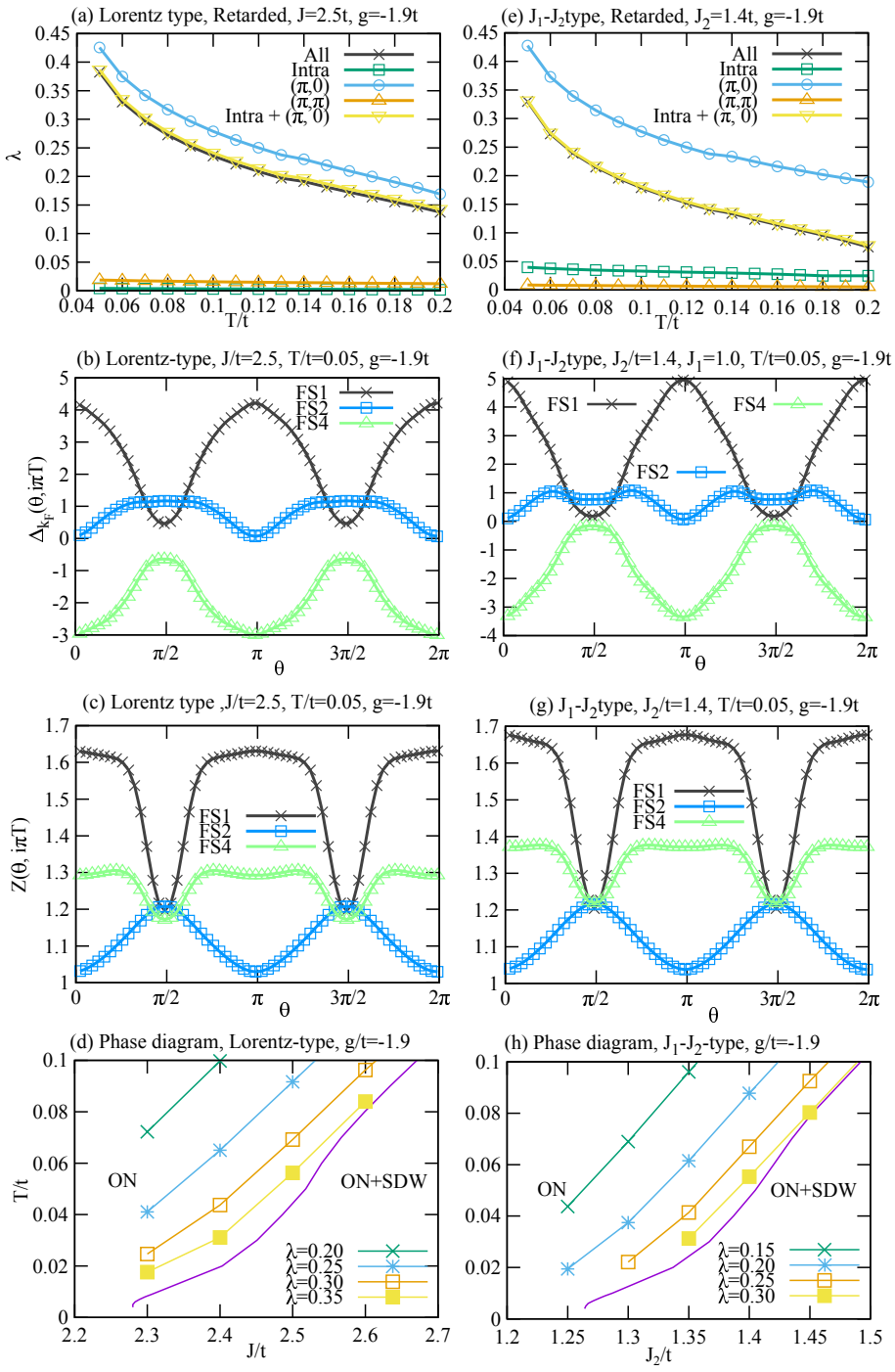

Figure 72: Possible superconductivity from spin fluctuations deeply inside the nematic phase ($g/t = -1.9$) for the Lorentz-type [(a)-(d)] and the $J_1 - J_2$-type [(e)-(h)] spin fluctuations. (a) and (e) Temperature dependence of the largest eigenvalues. (b) and (f) Momentum dependence of pairing gap. (c) and (g) Momentum dependence of the renormalization function. (d) and (h) Magnetic phase diagram in the plane of the strength of the spin interaction and temperature; the eigenvalues of the Eliashberg equations are plotted with contour lines.

is also suppressed more. Figure 72 (d) is a phase diagram as a function of the strength of the spin interaction J. This is also very similar to that in the case of $g/t = -1.8$ [Fig.44 (b)], except that the eigenvalues are suppressed more.

$J_1 - J_2$ -type spin fluctuations

Corresponding results for the $J_1 - J_2$-type spin fluctuations are summarized in the right panels in Fig.72, which shows very similar results to the Lorentz-type spin fluctuations. Minor differences are i) the eigenvalue from intra-pocket scattering processes is larger than that from "$(\pi, 0)$"-scattering processes [Fig.72 (e)] and ii) the eigenvalue tends to be suppressed more [Fig.72 (h)].

5.2.2 Superconductivity from spin fluctuations without the self-energy effect

To clarify a role of the self-energy effect on the superconductivity from spin fluctuations, we perform the same calculations as Section 3.2 except that we here neglect the self-energy effect ant assume $Z = 1$. Figure 73 (a) is the temperature dependence of the eigenvalues of the Eliashberg equations for the Lorentz-type spin fluctuations in the tetragonal phase. This result is qualitatively the same as Fig.41 (a), where the self-energy effect is considered. Quantitatively, the eigenvalues are substantially increased by neglecting the self-energy effect. Since the resulting eigenvalue exceeds unity and we obtain superconductivity from spin fluctuations alone. The momentum dependence of the pairing gap is shown in Fig.74 (a), which is very similar to Fig.42 (a), implying that the self-energy effect does not change the gap structure. Resulting superconducting phase diagram is presented in Fig.75 (a), showing that Lorentz-type spin fluctuations can drive the superconductivity very close to the SDW phase at low temperature.

Corresponding results in the nematic phase are given in Figs.73 (b), 74 (b), and 75 (b). As we have discussed in Section 3.2 in the presence of the self-energy, the nematic order has similar effects even in the absence of the self-energy: The eigenvalues of the Eliashberg equations tend to be suppressed [Figs.73 (b) and 75 (b)] and the pairing gap acquires a large momentum dependence [Fig.74 (b)]. In contrast to the case in the tetragonal phase, it is difficult that spin fluctuations drive superconductivity in the nematic phase even if the self-energy effect is discarded.

We also perform the same calculations for $J_1 - J_2$-type spin fluctuations without the self-energy effect. Figure 73 (c) is the temperature dependence of the eigenvalues of the Eliashberg equations. While "$(\pi, 0)$"-scattering processes yield the eigenvalue exceeding unity [Fig.73 (c)], it is substantially suppressed by intra-pocket scattering processes. Because of this self-restraint effect of the superconductivity, $J_1 - J_2$-type spin fluctuations are difficult to drive the superconductivity even if the self-energy effect is discarded. Compared to the case of Lorentz-type spin fluctuations [Fig.75 (a)], the region where the

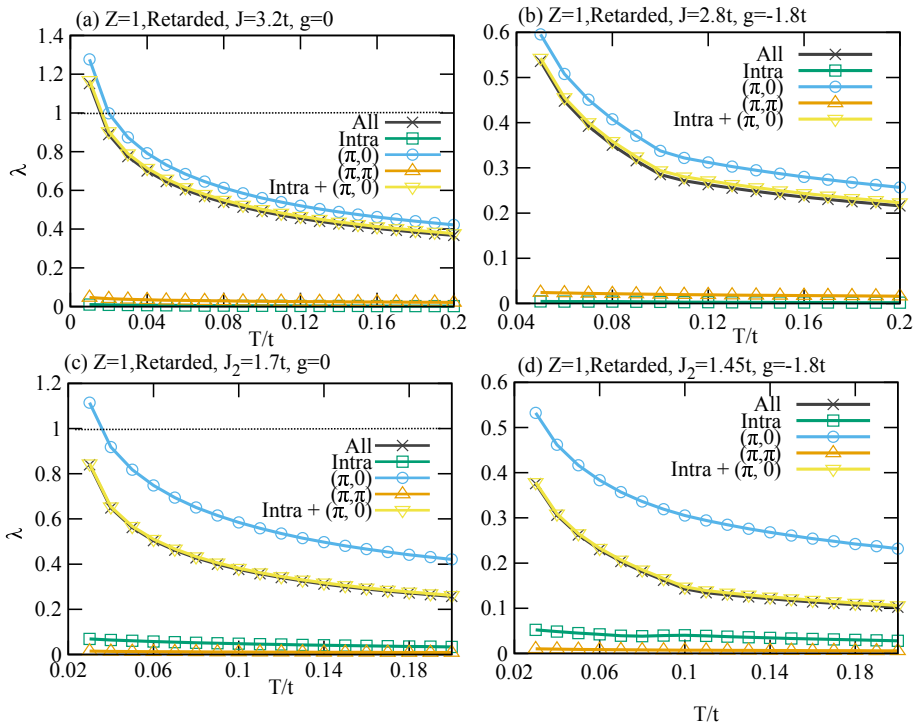

Figure 73: Temperature dependence of the eigenvalues of the Eliashberg equations without the self-energy effect for the Lorentz-type spin fluctuations (a) in the tetragonal phase and (b) in the nematic phase. (c) and (d) corresponding results for the $J_1 - J_2$-type spin fluctuations.

superconducting instability occurs is very limited in the vicinity of the SDW phase as shown in Fig.75 (c). The momentum dependence of the pairing gap is shown in Fig.74 (c), which shares the same feature as that with the self-energy effect [Fig.48 (a)] except that the modulation of the pairing gap on FS1, FS3, and FS4 is enhanced.

Corresponding results in the nematic phase are shown in Figs.73 (d), 74 (d), and 75 (d). As in the case of Lorentz-type spin fluctuations, the tendency of the superconducting instability is suppressed by the nematic order [Figs.73 (d) and 75 (d)] and the modulation of the pairing gap is enhanced although the gap on FS3 almost vanishes.

All results presented in this section imply that the self-energy effect does not provide qualitative changes, but quantitative ones. In particular, the absolute value of the eigenvalue of the Eliashberg equations is heavily suppressed by the self-energy effect. In this sense, the self-energy effect is very important when discussing whether spin fluctuations can actually drive the superconductivity with T_c comparable to the experimental observation.

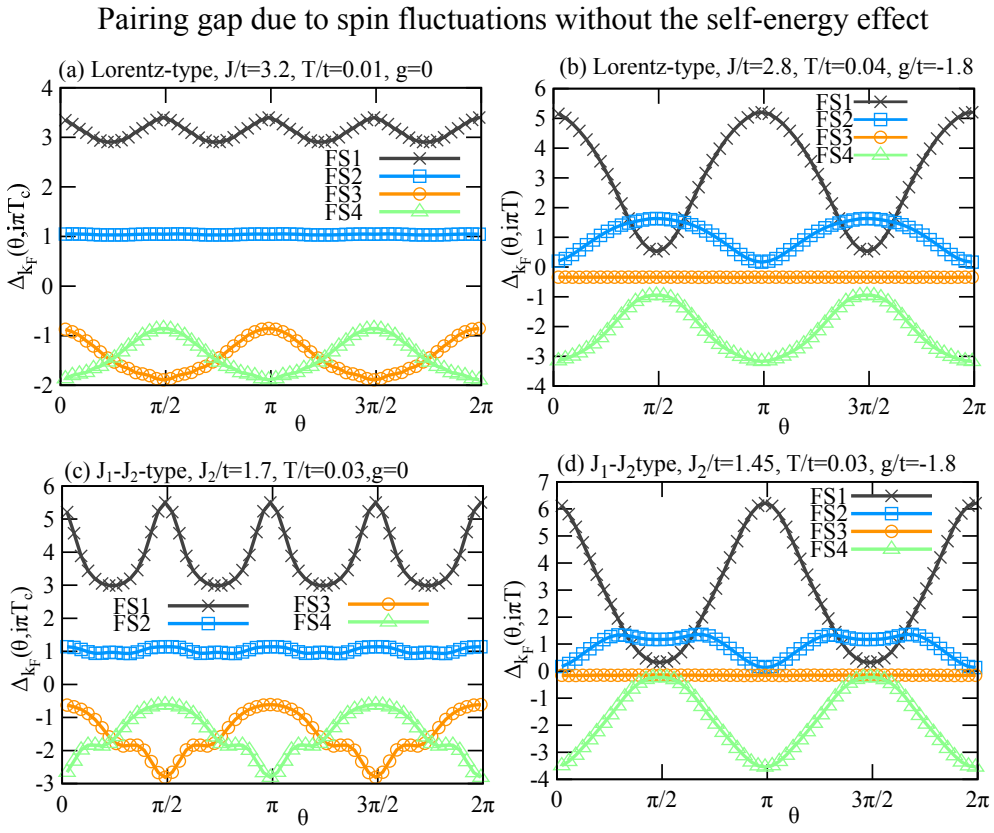

Figure 74: Momentum dependence of the pairing gap without the self-energy effect for the Lorentz-type spin fluctuations (a) in the tetragonal phase and (b) in the nematic phase. (c) and (d) corresponding results for the $J_1 - J_2$-type spin fluctuations.

5.3 Superconducting instability from both orbital nematic and spin fluctuations deeply inside the nematic phase

Orbital nematic and spin fluctuations

The electron pocket FS3 (Fig.10) disappears deeply inside the nematic phase, although it turns out that essentially new insight is not obtained for the superconducting mechanism. For completeness, however, we present results of superconducting instability from both orbital nematic and spin fluctuations in such a case.

The left column in Fig.76 is for the Lorentz-type spin fluctuations and the right column for the $J_1 - J_2$-type spin fluctuations. First of all, no qualitative differences are seen between results in the left and right column. Quantitatively, the $J_1 - J_2$-type spin fluctuations suppress the superconductivity from orbital nematic fluctuations more than the Lorentz-type spin fluctuations [Figs.76 (d) and (h)]. All results in Figs.76 (a) - (d) [Figs.76 (e) - (h)] can be compared with Figs.51 (b), 52 (b), 53 (b), and 54 (b) [Figs.56 (b), (d), and (f)] where FS3 substantially shrinks but remains (see Fig.10). Such a com-

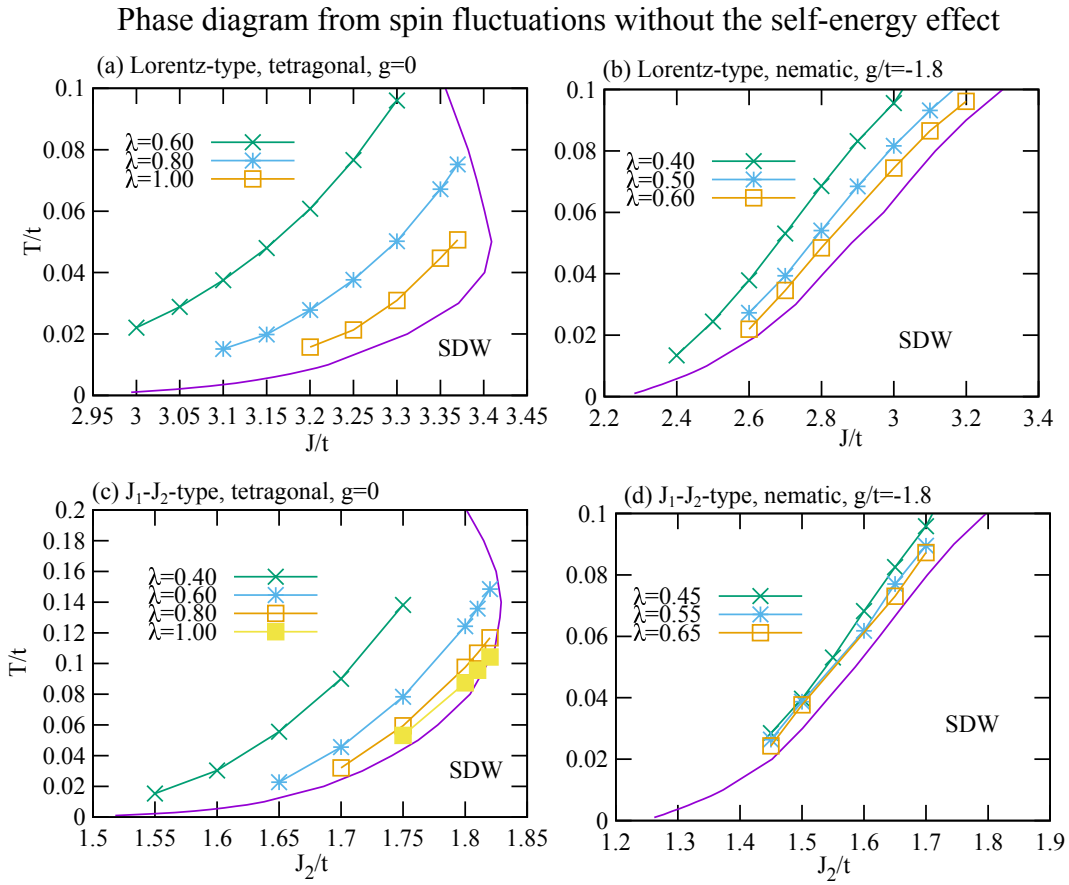

Figure 75: Phase diagram in the plane of the strength of the spin interaction and temperature in the absence of the self-energy effect for the Lorentz-type spin fluctuations (a) in the tetragonal phase and (b) in the nematic phase. Contour lines of the largest eigenvalue of the Eliashberg equations are plotted near the SDW phase. (c) and (d) corresponding results for the $J_1 - J_2$-type spin fluctuations.

parison shows that the major effect of a larger orbital nematic order is to enhance the momentum dependence of the pairing gap [Figs.76 (b) and (f)] and the renormalization function [Figs.76 (c) and (g)]. Although we have found that the pairing symmetry changes from s_{++}-wave to $s_{\pm}$-wave close to the SDW phase in the tetragonal phase in Figs.54 (a) and 57 (a), the pairing gap retains s_{++}-wave symmetry even in the vicinity of the SDW phase in the nemati phase; see Figs.76 (d) and (h), Fig.54 (b), and Fig.57 (b).

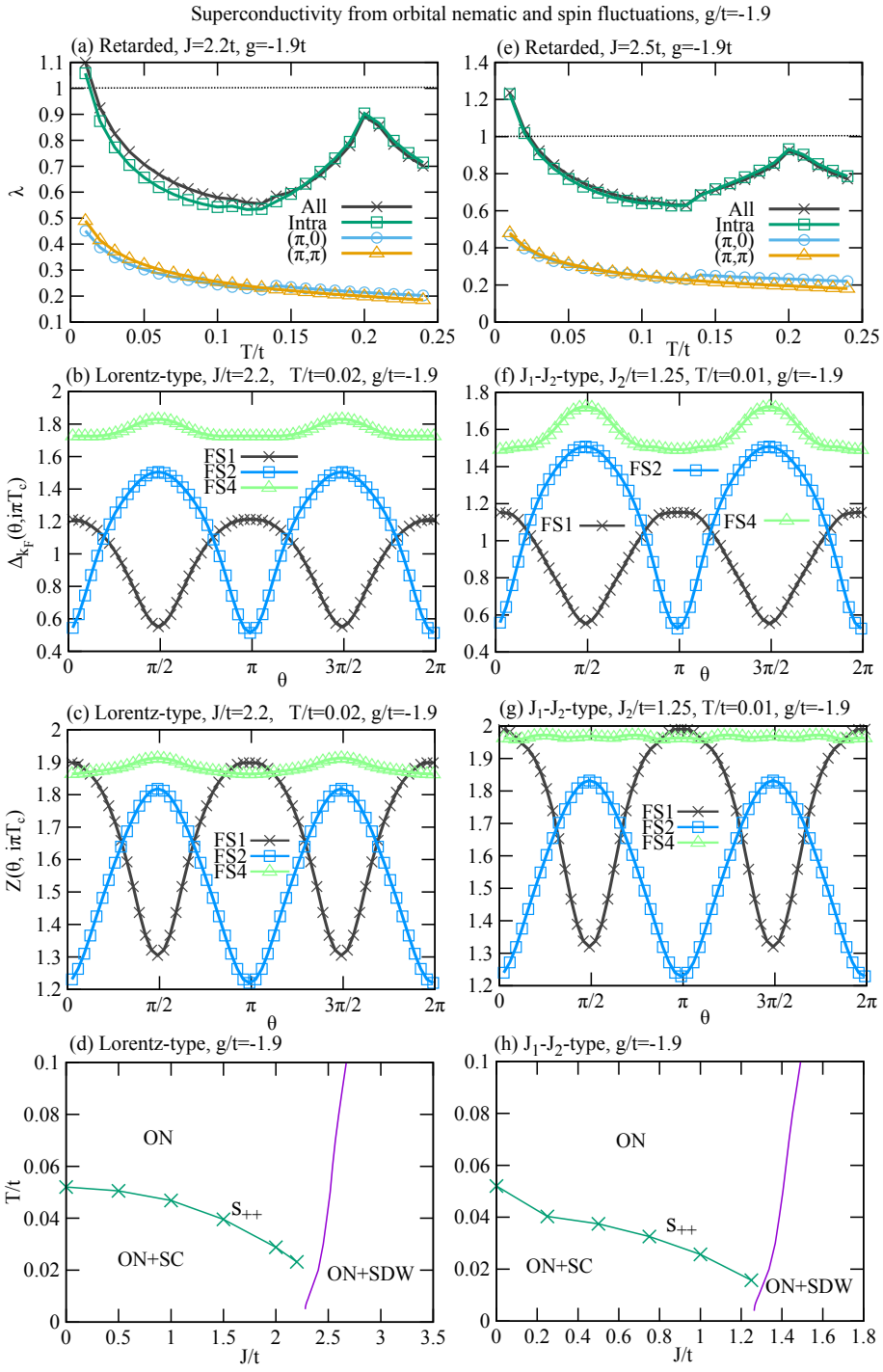

Figure 76: Superconductivity from both orbital nematic and spin fluctuations deeply inside the nematic phase ($g/t = -1.9$) [(a)-(d)] for the Lorentz-type spin fluctuations ($J/t = 2.2$) and [(e)-(h)] for the $J_1 - J_2$-type spin fluctuations ($J_2/t = 1.25$). (a) and (e) Temperature dependence of the eigenvalues. (b) and (f) Momentum dependence of the pairing gap. (c) and (g) Momentum dependence of the renormalization function. (d) and (h) Phase diagram in the plane of the strength of the spin interaction and temperature; note that the system has purely orbital nematic fluctuations at $J/t = 0$ and $J_2/t = 0$.

References

[1] J. Bardeen, L. N. Cooper, and J. R. Schrieffer, Phys. Rev. **108**, 1175 (1957).

[2] J. G. Bednorz and K. A. Müller, Z. Phys. B Condens. Matter **64**, 189 (1986).

[3] C. W. Chu, L. Gao, F. Chen, Z. J. Huang, R. L. Meng, and Y. Y. Xue, Nature **365**, 323 (1993).

[4] Md. A. Rahman, Md. Z. Rahaman, and Md. N. Samsuddoha, Am. J. Phys. Appl. **3**, 39 (2015).

[5] F. C. Zhang and T. M. Rice, Phys. Rev. B **37**, 3759 (1988).

[6] Y. Kamihara, H. Hiramatsu, M. Hirano, R. Kawamura, H. Yanagi, T. Kamiya, and H. Hosono, J. Am. Chem. Soc. **128**, 10012 (2006).

[7] G. Wu, Y. L. Xie, H. Chen, M. Zhong, R. H. Liu, B. C. Shi, Q. J. Li, X. F. Wang, T. Wu, J. J. Ying, and X. H. Chen, J. Phys: Condens. Matter **21**, 142203 (2009).

[8] S. He, J. He, W. Zhang, L. Zhao, D. Liu, X. Liu, D. Mou, Y.-B. Ou, Q.-Y. Wang, Z. Li, L. Wang, Y. Peng, Y. Liu, C. Chen, L. Yu, G. Liu, X. Dong, J. Zhang, C. Chen, Z. Xu, X. Chen, X. Ma, Q. Xue, and X. J. Zhou, Nat. Mat. **12**, 605 (2013).

[9] F.-C. Hsu, J.-Y. Luo, K.-W. Yeh, T.-K. Chen, T.-W. Huang, P. M. Wu, Y.-C. Lee, Y.-L. Huang, Y.-Y. Chu, D.-C. Yan, and M.-K. Wu, Proc. Natl. Acad. Sci. USA **105**, 14262 (2008).

[10] X. Chen, P. Dai, D. Feng, T. Xiang and F.-C. Zhang, Natl. Sci. Rev. **1**, 371 (2014).

[11] A. Chubukov, Annu. Rev. Condens. Matter Phys. **3**, 57 (2012).

[12] P. Dai, J. Hu, and E. Dagotto, Nat. phys. **8**, 709 (2012).

[13] A. Chubukov, arXiv 1507.03856 (2015).

[14] S. Kasahara, H. J. Shi, K. Hashimoto, S. Tonegawa, Y. Mizukami, T. Shibauchi, K. Sugimoto, T. Fukuda, T. Terashima, A. H. Nevidomskyy, and Y. Matsuda, Nature **486**, 382 (2012).

[15] K. Kuroki, S. Onari, R. Arita, H. Usui, Y. Tanaka, H. Kontani, and H. Aoki, Phys. Rev. Lett. **101**, 087004 (2008).

[16] S. Raghu, Xiao-Liang Qi, Chao-Xing Liu, D. J. Scalapino, and Shou-Cheng Zhang, Phys. Rev. B **77**, 220503 (2008).

[17] Zi-Jian Yao, Jian-Xin Li, and Z. D. Wang, New J. Phys. **11**, 025009 (2009).

[18] L. Boeri, O. V. Dolgov, and A. A. Golubov, Phys. Rev. Lett. **101**, 026403 (2008).

[19] T. Moriya, Proc. Jpn. Acad., Ser. B Phys. Biol. Sci. **82**, 1 (2006).

[20] I. I. Mazin, D. J. Singh, M. D. Johannes, and M. H. Du, Phys. Rev. Lett. **101**, 057003 (2008).

[21] G. R. Stewart, Rev. Mod. Phys. **83**, 1589 (2011).

[22] T. D. Stanescu, V. Galitski, and S. D. Sarma, Phys. Rev. B **78**, 195114 (2008).

[23] H. Kontani and S. Onari, Phys. Rev. Lett. **104**, 157001 (2010).

[24] C. Fang, H. Yao, W.-F. Tsai, J. P. Hu, and S. A. Kivelson, Phys. Rev. B **77**, 224509 (2008).

[25] C. Xu, Y. Qi, and S. Sachdev, Phys. Rev. B **79**, 134507 (2008).

[26] F. Krüger, S. Kumar, J. Zaanen, and J. van den Brink, Phys. Rev. B **103**, 054504 (2009).

[27] C.-C. Lee, W.-G. Yin, and W. Ku, Phys. Rev. Lett. **103**, 267001 (2009).

[28] W. Lv, J. Wu, and P. Phillips, Phys. Rev. B **80**, 224506 (2009).

[29] H. Yamase and R. Zeyher, New J. Phys. **17**, 073030 (2015).

[30] Y. Yanagi, Y. Yamakawa, and Y. Ōno, Phys. Rev. B **81**, 054518 (2010).

[31] Y. Yanagi, Y. Yamakawa, N. Adachi, and Y. Ōno, J. Phys. Soc. Jpn. **79**, 123707 (2010).

[32] H. Yamase and R. Zeyher, Phys. Rev. B **88**, 180502 (2013).

[33] G. M. Eliashberg, J. Exp. Theor. Phys. **11**, 696 (1960).

[34] D. J. Singh, Physica C **469**, 418 (2009).

[35] S. Raghu, A. Paramekanti, E-.A. Kim, R. A. Borzi, S. A. Grigera, A. P. Mackenzie, and S. A. Kivelson, Phys. Rev. B **79**, 214402 (2009).

[36] W. -C. Lee and C. Wu, Phys. Rev. B **80**, 104438 (2009).

[37] S. Sachdev, Physica A **313**, 252 (2002).

[38] T. Agatsuma and H. Yamase, Phys. Rev. B **96**, 214505 (2016).

[39] T. Shimojima, F. Sakaguchi, K. Ishizawa, Y. Ishida, T. Kiss, M. Okawa, T. Togashi, C.-T. Chen, S. Watanabe, M. Arita, K. Shimada, H. Namatame, M. Taniguchi, K. Ohguchi, S. Kasahara, T. Terashima, T. Shibauchi, Y. Matsuda, A. Chainani, and S. Shin Science **332**, 564 (2011).

[40] H. Ding, P. Richard, K. Nakayama, K. Sugawara, T. Arakane, Y. Sekiba, A. Takayama, S. Souma, T. Sato, T. Takahashi, Z. Wang, X. Dai, Z. Fang, G. F. Chen, J. L. Luo, and N. L. Wang, Europhys. Lett. **83**, 47001 (2008).

[41] K. Nakayama, T. Sato, P. Richard, Y.-M. Xu, Y. Sekiba, S. Souma, G. F. Chen, J. L. Luo, N. L. Wang, H. Ding, and T. Takahashi, Europhys. Lett. **85**, 67002 (2009).

[42] N. Xu, P. Richard, X.-P. Wang, X. Shi, A. van Roekeghem, T. Qian, E. Ieki, K. Nakayama, T. Sato, E. Rienks, S. Thirupathaiah, J. Xing, H.-H. Wen, M. Shi, T. Takahashi, and H. Ding, Phys. Rev. B **564**, 094513 (2013).

[43] Y. Zhang, Z. R. Ye, Q. Q. Ge, F. Chen, J. Jiang, M. Xu, B. P. Xie, and D. L. Feng, Nat. Phys. **8**, 371 (2012).

[44] T. Shimojima, F. Sakaguchi, K. Ishizaka, Y. Ishida, W. Malaeb, T. Yoshida, S. Ideta, A. Fujimori, T. Kiss, M. Okawa, T. Togashi, C.-T. Chen, S. Watanabe, Y. Nakashima, A. Ino, H. Anzai, M. Arita, K. Shimada, H. Namatame, M. Taniguchi, S. Kasahara, T. Terashima, T. Shibauchi, Y. Matsuda, M. Nakajima, S. Uchida, K. Kihou, C. H. Lee, A. Iyo, H. Eisaki, A. Chainani, and S. Shin Solid State Commun. **152**, 695 (2011).

[45] T. Kondo, A. F. Santander-Syro, O. Copie, C. Liu, M. E. Tillman, E. D. Mun, J. Schmalian, S. L. Bud'ko, M. A. Tanatar, P. C. Canfield, and A. Kaminski, Phys. Rev. Lett. **101**, 147003 (2008).

[46] D. Mou, T. Kong, W. R. Meier, F. Lochner, L.-L. Wang, Q. Lin, Y. Wu, S. L. Bud'ko, I. Eremin, D. D. Johnson, P. C. Canfield, and A. Kaminski, Phys. Rev. Lett. **117**, 277001 (2016).

[47] Y. Zhang, L. X. Yang, M. Xu, Z. R. Ye, F. Chen, C. He, H. C. Xu, J. Jiang, B. P. Xie, J. J. Ying, X. F. Wang, X. H. Chen, J. P. Hu, M. Matsunami, S. Kimura, and D. L. Feng, Nat. Mater. **10**, 273 (2011).

[48] D. Liu, W. Zhang, D. Mou, J. He, Y.-B. Ou, Q.-Y. Wang, Z. Li, L. Wang, L. Zhao, S. He, Y. Peng, X. Liu, C. Chen, G. Liu, X. Dong, J. Zhang, C. Chen, Z. Xu, X. Chen, X. Ma, Q. Xue, and X. J. Zhou, Nat. Commun. **3**, 931 (2012).

[49] Y. Miyata, K. Nakayama, K. Sugawara, T. Sato, and T. Takahashi, Nat. Mat. **14**, 775 (2015).

[50] L. Zhao, D. Mou, S. Liu, X. jia, J. He, Y. Peng, L. Yu, X. Liu, G. Liu, S. He, X. Dong, J. Zhang, J. P. He, D. M. Wang, G. F. Chen, J. G. Guo, X. L. Chen, X. Wang, Q. Peng, Z. Wang, S. Zhang, F. Yang, Z. Xu, C. Chen, and X. J. Zhou, Phys. Rev. B **83**, 140508 (2011).

[51] H. Miao, P. Richard, Y. Tanaka, K. Nakayama, T. Qian, K. Umezawa, T. Sato, Y. -M. Xu, Y. B. Shi, N. Xu, X. -P. Wang, P. Zhang, H. -B. Yang, Z. -J. Xu, J. S. Wen, G. -D. Gu, X. Dai, J. -P. Hu, T. Takahashi, and H. Ding, Phys. Rev. B **85**, 094506 (2012).

[52] X. C. Xu, X. H. Niu, D. F. Xu, J. Jiang, Q. Yao, Q. Y. Chen, Q. Song, M. Abdel-Hafiez, D. A. Chareev, A. N. Vasiliev, Q. S. Wang, H. L. Wo, and J. Zhao, Phys. Rev. Lett. **117**, 157003 (2016).

[53] K. Okazaki, Y. Ota, K. Kotani, W. Malaeb, Y. Ishida, T. Shimojima, T. Kiss, S. Watanabe, C.-T. Chen, K. Kihou, C. H. Lee, A. Iyo, H. Eisaki, T. Saito, H. Fukazawa, Y. Kohori, K. Hashimoto, T. Shibauchi, Y. Matsuda, H. Ikeda, H. Miyahara, R. Arita, A. Chainani, and S. Shin, Science **337**, 1314 (2012).

[54] Y. Ota, K. Okazaki, Y. Kotani, T. Shimojima, W. Malaeb, S. Watanabe, C.-T. Chen, K. Kihou, C. H. Lee, A. Iyo, H. Eisaki, T. Saito, H. Fukazawa, Y. Kohori, and S. Shin, Europhys. Lett. **89**, 081103 (2014).

[55] S. Graser, T. A. Maier, P. J. Hirschfeld, and D. J. Scalapino, New J. Phys. **11**, 025016 (2009).